Royal Holloway, University of London

Department of Mathematics

Momentum Distributions in the Dipole and Non-Dipole Regimes for Atoms in Strong Laser Fields

Author:

Samuel David Jenkins

Supervisor:

Professor Pat O'Mahony

Thesis submitted to the University of London for the degree of Doctor of Philosophy

2019

Declaration of Authorship

I, Samuel David Jenkins, hereby declare that this thesis and the work presented in it is entirely my own. Where I have consulted the work of others, this is always clearly stated.

Signed .... (Samuel David Jenkins)

Date:

Summary

The direct solution of the time dependent Schrödinger equation (TDSE) can yield an accurate theoretical description of the dynamics of atoms subject to intense electromagnetic radiation. However, it can become computationally difficult depending on the frequency, intensity, polarisation and duration of the electric field. In this thesis we explore the dynamics of laser-atom interactions subject to linear and circularly polarised radiation both in the dipole and non-dipole regimes.

We begin by outlining the mathematics and physics behind the Hamiltonian for the problem and we describe the main physical effects and current models which describe such effects. We then introduce some of the numerical methods used to solve the TDSE, such as grid based or spectral methods, before focussing on a spectral method which uses the Crank-Nicolson algorithm together with preconditioning and the bi-conjugate gradient method to propagate the solution in time. We use this method to study the propensity rule for argon in circularly polarised light, namely that an electron counter-rotating with respect to the laser is more easily ionised than one that is co-rotating. We do this over a range of frequencies and intensities covering the adiabatic tunnelling regime, non-adiabatic tunnelling regime, and the multiphoton ionisation regime. We then examine the final state momentum distribution for both hydrogen and argon subject to an elliptically polarised field and, in particular, the momentum distribution transverse to the polarisation plane

(TEMD) which is very sensitive to the electron ion interaction. We study the TEMD as a function of the ellipticity of the field and we demonstrate the existence of an inverted cusp for the TEMD for initial $l = 1$ and $m = 0$ states. Finally, we perform exploratory calculations of the momentum distributions for low frequency fields to examine non-dipole effects.

Acknowledgements

First and foremost I would like to extend a heartfelt thank you to Pat O'Mahony and Francisca Mota-Furtado for their support in the production of this thesis. Over the course of the four years, they have always been generous with their time, energy and expertise. Their input is always greatly appreciated. I would also like to thank Bernard Piraux and Alexander Galstyan. Bernard, for his hospitality and engagement whenever I visited Louvain-la-Neuve (and even when I was at home in Royal Holloway) and Alex for the numerous times he was able to offer his computational knowledge and friendship.

For all her patience and generosity over the course of the last year, Claire O'Reilly deserves a special mention and thank you for her input and support, especially in the final parts of this process.

Not last nor least, I would like to thank my parents for their support throughout my academic career. From the small things to the big, these four years would have been made more difficult without them.

I would like to thank Royal Holloway for allowing me to undertake this opportunity the first place and finally, the EPSRC for providing financial support through a 3 year PhD studentship.

List of Scientific Contributions

Publications

- **Modelling laser-atom interactions in the strong field regime.**
  Alexander Galstyan, Yuri V. Popov, Francisca Mota-Furtado, Patrick F. O'Mahony, Noël Janssens, Samuel D. Jenkins, Ochbadrakh Chuluunbaatar and Bernard Piraux, *The European Physical Journal D* 71.4 (2017), p.97 [36].

Invited Talks

- **Hybrid basis set approach to the solution of the TDSE for short intense pulses.**
  Samuel D. Jenkins.
  WG1 Expert Meeting on "Frontiers in attosecond theory: from atoms to molecules to solids".
  Hans-sur-Lesse, Belgium, $4^{th} - 8^{th}$ April 2016.

- **Momentum maps for atoms in intense elliptically polarized fields.**
  Samuel D. Jenkins, Francisca Mota-Furtado, P. F. O'Mahony, Bernard Piraux.

4th XLIC General Meeting.

Hotel Pyramida, Prague, Czech Republic, $14^{th} - 16^{th}$ March 2017.

Conference Preprints

- **Investigating the propensity rule in atoms in intense circularly polarised laser pulses.**
  Samuel D. Jenkins, P. F. O'Mahony, Francisca Mota-Furtado.
  2nd XLIC WG1 meeting "Ultrafast electron dynamics in molecules"
  University of Edinburgh, UK, $29^{th} - 30^{th}$ August 2016.

- **Momentum maps for atoms in intense elliptically polarized fields.**
  Samuel D. Jenkins, Francisca Mota-Furtado, P. F. O'Mahony, Bernard Piraux.
  International School of Quantum Electronics 59th Course: The frontiers of attosecond and ultrafast X-ray science.
  Erice, Sicily, Italy, $19^{th} - 28^{th}$ March 2017.

List of Figures

List of Tables

Contents

Chapter 1

Introduction

The first laser was produced using ruby crystal by Theodore H. Maiman at Hughes Research Laboratories in 1960 [58]. As early as 1931, Maria Göppert-Mayer predicted that double photon absorption was possible in her doctoral dissertation [38] which was proven true in 1961 by Kaiser and Garret [47] who detected two photon excitation in Eu^{2+}. In 1979 the first observation of above threshold ionisation was seen in xenon using a neodymium glass laser by Agostini *et al* [1] where the electron absorbs more photons than is required to ionise through multiphoton ionisation. Since then many developments have been made in the field. Intense laser fields are now available covering a frequency range from the infrared to the ultraviolet and X-ray in the form of short well-defined pulses. In particular the introduction of the 'reaction microscope' [28] has allowed experimentalists to map out the momentum distribution of the final products following interaction of the atom with the laser. On the theory side, models such as the strong field approximation, the three step model etc. (see Chapter 2) have been used to try to interpret the results.

In this thesis we will concentrate on the ab initio solution of the time dependent Schrödinger equation (TDSE) for argon subject to intense laser fields to investigate an interesting propensity rule in relation to the initial state of the atom. In addition to this, we also look at the momentum distribution of hydrogen and argon in dipole and non-dipole regimes. The electron momentum transverse to the direction of the electric field exhibits a sharp cusp

like shape about zero momentum under certain conditions in contradiction to theory. When non-dipole effects are introduced, we study the asymmetry in the momentum distribution along the direction the laser field is propagating.

In this thesis we will concentrate on the ab initio solution of the time dependent Schrödinger equation (TDSE) and how it can be used to obtain the momentum distribution in both the dipole and non-dipole regimes and to address an interesting propensity rule. The intensity of the laser fields we shall consider are comprised of such a large number of photons that we can approximate the field by treating it as a classical electromagnetic field described by Maxwell's equations. A number of methods shall be outlined to represent the wave function, either through the use of grid based methods or as a linear combination of basis set functions. For the majority of calculations considered, the B-spline basis was the preferred representation of the wave function of the electron. To propagate TDSE in time, we apply the Crank-Nicolson scheme with preconditioning and the bi-conjugate gradient method or BiCGSTAB algorithm. The BiCGSTAB algorithm allows for the efficient solution of systems of coupled differential equations. We study hydrogen and argon in an intense laser field where for the latter we use the single active electron approximation.

1.1 Structure of the Thesis

- In Chapter 2 we describe the basic background material required to study atoms interacting with electromagnetic fields. We define the Hamiltonian and explain the theory behind gauge transformations. The various regimes for laser-atom interactions are outlined, namely the multiphoton, tunnelling and over the barrer ionisation regime. All of the above

regimes are considered within this body of work. We introduce the dipole approximation and the regions of laser parameters where it can applied.

- Chapter 3 outlines the various methods we explored for propagating the TDSE. Different ways to represent the wave function are considered. Grid based methods are explained alongside the B-Spline and Sturmian basis set function representation of the wave function. The numerical techniques required to integrate the TDSE using the Crank-Nicolson scheme with preconditioning and the bi-conjugate gradient method are described in detail. Simple 1-D grid based calculations are displayed, as well as computationally inexpensive 3-D calculations involving Sturmian functions. The advantages and disadvantages of representing the wave function in terms of the Sturmian and B-spline functions are also discussed.

- In Chapter 4 we investigate the *propensity rule* and its range of validity whereby electrons counter-rotating with respect to a circularly polarised electric field are preferentially ionised compared to co-rotating ones in the non-adiabatic tunnelling regime. The theory behind the propensity rule is explained in detail and some experimental evidence is given to corroborate the theory. We present results for ground state argon subject to a circularly polarised field for both $m = -1$ (counter-rotating) and $m = 1$ (co-rotating) to compare with the theory. We begin by looking at the non-adiabatic regime but happen upon interesting results by moving beyond this point into the multiphoton ionisation regime.

- Chapter 5 is a study into the dynamics of electrons ionised in the direction transverse to the electric field. In the dipole approximation, the transverse momentum distribution (TEMD) of the ionised electrons isola-

tes the interaction between the photoelectron and the parent-ion leading to cusp-like structures in the TEMD. Commonalities are found in the momentum distributions for hydrogen and argon. However a new inverted cusp structure is found for a particular initial state of the system.

- In Chapter 6, an attempt is made to move into the non-dipole regime for ground state hydrogen subject to a low frequency, intense linearly polarised laser field. Experimental work in the field suggests that for linearly polarised fields, electrons should be pulled back towards the ion-core after experiencing radiation pressure in the direction of propagation during the pulse. The inclusion of non-dipole components to the Hamiltonian alongside the parameters of the laser make these problems very computationally expensive. Several approximations are made in exploratory calculations of non-dipole effects.

- In Appendix A, we describe some separate work we did on the momentum space representation of the Schrödinger equation which formed part of a new publication [36]. There we show how the Coulomb kernel in momentum space can be expressed as a sum over products of Gegenbauer polynomials.

- In Appendix B, the derivation of the coefficients of the continuum Coulomb functions in the Sturmian basis is laid out in full. These are coefficients are required in Chapter 5.

1.2 A note on the programming work in this thesis

At the start of the PhD I focussed on learning how to solve the basic 1 dimensional hydrogen TDSE subject to linearly polarised laser field using grid based methods using Fortran. Note that all numerical calculations presented in this thesis were calculated with Fortran. For the 1-dimensional cases considered, the Crank-Nicolson method was used to propagate the wave function in time, step by step.

After becoming comfortable with the 1 dimensional case, I was moved on to the full 3 dimensional hydrogen TDSE subject to linearly and circularly polarised laser fields. These cases were treated using the Sturmian basis due to the similarity between the Sturmian functions and the hydrogenic radial wave functions. Propagation of the wave function in time was performed using the Arnoldi time propagator. To study the TDSE for argon, an attempt was made to combine the Sturmian function basis with the B-Spline basis. A working code was produced that represented the non-hydrogenic behaviour near the core using the B-Spline functions and the behaviour far from the core, which can be considered hydrogenic, using the Sturmian functions. The combination of a pre-written algorithm for the Arnoldi time propagator and the mixed basis resulted in propagation that ran far too slowly for the problems that are now presented in the body of this thesis.

In order to address this, the mixed basis approach to representing argon was put to one side in favour of representing both hydrogen and argon in the B-Spline basis. The Arnoldi time propagator was removed and I programmed the Crank-Nicolson method with preconditioner to propagate the TDSE in time and I programmed the BiCG-STAB algorithm to solve for $\mathbf{x}$ in the system

$A\mathbf{x} = \mathbf{b}$ where A and $\mathbf{b}$ are known. If applicable, parallel programming was applied to the new algorithms with OpenMP to speed up the computations further. The consequences of these changes was a significant decrease in the time taken for propagation and the amount of memory required to perform a full calculation was also significantly reduced. This permitted problems which would require much larger parameters to be compiled and run within a reasonable amount of time. Even problems involving non-dipole dynamics where all (l, m) pairs in the Hamiltonian are accessible were made possible.

Unless stated otherwise, the observables of the wave function computed within this thesis were also programmed by myself. These include momentum distributions, ionisation, excitation and ground state probabilities and the density of l and (l, m) states in the continuum part of the atomic wave function.

Atomic Interactions with an Intense Electromagnetic Field

2.1 Introduction

We assume that the electromagnetic field can be treated classically due to the overwhelming number of photons considered when dealing with very intense laser fields. In order to describe the field continuously, this chapter introduces Maxwell's equations of electromagnetism and defines the general equation for the electric field and vector potential with any polarisation used in this thesis.

While the field is treated classically, the atomic system is treated quantum mechanically. We describe the main quantum mechanical dynamics that arise from the interaction of a classical electromagnetic field and define the Hamiltonian of the system in two main parts: the atomic interaction and the interaction with the electromagnetic field. The various approximations that are to be used within this text are explained and we establish the parameter space to which they can be employed. We will study pulsed fields with intensities ranging from 10^{13} to $10^{15} W/cm^2$ and wavelengths ranging from 800 nm to 2.5 μm. We introduce the dipole approximation for the atom-field interaction and some of the important concepts and models which have been used in the field to date. In particular, the main approximations we take advantage of are the dipole approximation and the *single active electron* (SAE) approximation

for laser-atom interactions involving argon (a multi-electron system) and the Muller potential [62].

2.2 External Field

The classical electromagnetic field in vacuo can be described in terms of the electric field, $\mathbf{E}(\mathbf{r}, t)$, and the magnetic field, $\mathbf{B}(\mathbf{r}, t)$, which satisfy Maxwell's field equation without sources:

$$\nabla \cdot \mathbf{E} = 0 \tag{2.1}$$

$$\nabla \cdot \mathbf{B} = 0 \tag{2.2}$$

$$\nabla \times \mathbf{E} = -\frac{\partial \mathbf{B}}{\partial t} \tag{2.3}$$

$$\nabla \times \mathbf{B} = \frac{1}{c^2} \frac{\partial \mathbf{E}}{\partial t} \tag{2.4}$$

where c is the speed of light. We may also choose to describe the electromagnetic field using the scalar field, $\phi(\mathbf{r}, t)$, and vector potential, $\mathbf{A}(\mathbf{r}, t)$, from the following relations:

$$\mathbf{E} = -\nabla \phi - \frac{\partial \mathbf{A}}{\partial t} \tag{2.5}$$

$$\mathbf{B} = \nabla \times \mathbf{A}. \tag{2.6}$$

Using equations (2.1) to (2.6) we find that the vector potential satisfies the homogeneous wave equation

$$\nabla^2 \mathbf{A} - \frac{1}{c^2} \frac{\partial^2 \mathbf{A}}{\partial t^2} = 0. \tag{2.7}$$

Equations (2.5) and (2.6) produce the same electromagnetic field $\mathbf{E}$ and $\mathbf{B}$ under the gauge transformation

$$\mathbf{A} \to \mathbf{A}' = \mathbf{A} + \nabla\chi \qquad (2.8)$$

$$\phi \to \phi' = \phi - \frac{\partial\chi}{\partial t} \qquad (2.9)$$

where $\chi(\mathbf{r}, t)$ is an arbitrary scalar function. Careful choices of χ can simplify problems involving electromagnetic fields. When no sources are present, the most common gauge is the *Coulomb* gauge where the $\chi(\mathbf{r}, t)$ has been chosen to satisfy the condition

$$\nabla \cdot \mathbf{A} = 0. \qquad (2.10)$$

With this, we have $\phi = 0$, which transforms definitions of the electric and magnetic fields to

$$\mathbf{E} = -\frac{\partial\mathbf{A}}{\partial t} \qquad (2.11)$$

$$\mathbf{B} = \nabla \times \mathbf{A}. \qquad (2.12)$$

A monochromatic transverse plane wave solution to equation (2.7) is

$$\mathbf{A}(\mathbf{r}, t) = \hat{\boldsymbol{\epsilon}}A_0 \sin(\mathbf{k} \cdot \mathbf{r} - \omega t - \phi) \qquad (2.13)$$

where $\mathbf{k}$ is the propagation vector, ω is the frequency and ϕ the phase of the laser field. We use equations (2.11) and (2.12) to define the corresponding electric field and magnetic field as

$$\mathbf{E}(\mathbf{r}, t) = \hat{\boldsymbol{\epsilon}} E_0 \cos(\mathbf{k} \cdot \mathbf{r} - \omega t - \phi) \tag{2.14}$$

$$\mathbf{B}(\mathbf{r}, t) = (\hat{\mathbf{k}} \times \hat{\boldsymbol{\epsilon}}) \frac{E_0}{c} \cos(\mathbf{k} \cdot \mathbf{r} - \omega t - \phi) \tag{2.15}$$

where the electric field amplitude and vector potential amplitude are related by $E_0 = \omega A_0$ and the unit vector $\hat{\boldsymbol{\epsilon}}$ is known as the polarisation vector. The laser field defined by equations (2.14) and (2.15) is described as *linearly polarised*, that is to say, the electric field points in a fixed direction $\hat{\boldsymbol{\epsilon}}$ independent of time.

The combination of two orthogonal, phase shifted, linearly polarised transverse plane waves produces elliptically polarised light. The ellipticity of a particular laser field is defined by the quantity ξ. The corresponding vector potential and electric fields with ellipticity ξ are

$$\mathbf{A}(\mathbf{r}, t) = \frac{A_0}{\sqrt{1 + \xi^2}} [\hat{\boldsymbol{\epsilon}}_x \sin(\mathbf{k} \cdot \mathbf{r} - \omega t - \phi_x) - \xi \hat{\boldsymbol{\epsilon}}_y \cos(\mathbf{k} \cdot \mathbf{r} - \omega t - \phi_y)] \tag{2.16}$$

and

$$\mathbf{E}(\mathbf{r}, t) = \frac{E_0}{\sqrt{1 + \xi^2}} [\hat{\boldsymbol{\epsilon}}_x \cos(\mathbf{k} \cdot \mathbf{r} - \omega t - \phi_x) + \xi \hat{\boldsymbol{\epsilon}}_y \sin(\mathbf{k} \cdot \mathbf{r} - \omega t - \phi_y)]. \tag{2.17}$$

A special case of elliptically polarised light, called *circularly polarised* light, occurs when the conditions $\xi = \pm 1$ and $\phi_x = \phi_y$ are met. We may also distinguish the rotation of the field by labelling circularly polarised light when $\xi = 1$ as *right-circularly polarised* light and $\xi = -1$ as *left-circularly polarised* light.

2.3 The Hamiltonian

The Hamiltonian is the sum of operators pertaining to the kinetic and potential energies of a system. Given a particle with charge q, no spin and mass m in an atomic potential $V(\mathbf{r})$, the Hamiltonian operator for an atom in an electromagnetic field is as follows:

$$\hat{H} = \frac{1}{2m}(\hat{\mathbf{p}} - q\mathbf{A})^2 + q\phi + V(\mathbf{r}) \tag{2.18}$$

where momentum operator is defined as $\hat{\mathbf{p}} = -i\hbar\nabla$. In the case of one-electron systems, we may rewrite equation (2.18) with $m = 1$, $\hbar = 1$ and $q = -1$ in atomic units. Let us also expand the Hamiltonian like so:

$$\hat{H} = -\frac{1}{2}\nabla^2 - \frac{i}{2}(\mathbf{A} \cdot \nabla + \nabla \cdot \mathbf{A}) + \frac{1}{2}\mathbf{A}^2 - \phi + V(\mathbf{r}). \tag{2.19}$$

The solution to the time-dependent Schrödinger equation (TDSE)

$$i\frac{\partial}{\partial t}\Psi(\mathbf{r}, t) = \hat{H}\Psi(\mathbf{r}, t) \tag{2.20}$$

is invariant under the gauge transformation

$$\mathbf{A}(\mathbf{r}, t) = \mathbf{A}'(\mathbf{r}, t) + \nabla\chi(\mathbf{r}, t) \tag{2.21}$$

$$\phi(\mathbf{r}, t) = \phi'(\mathbf{r}, t) - \frac{\partial}{\partial t}\chi(\mathbf{r}, t) \tag{2.22}$$

$$\Psi(\mathbf{r}, t) = \Psi'(\mathbf{r}, t)e^{-i\chi(\mathbf{r}, t)} \tag{2.23}$$

where, in the case of equation (2.20), $\chi(\mathbf{r}, t)$ represents an arbitrary real, differentiable function of $\mathbf{r}$ and t. Combining equation (2.19) with the Coulomb gauge $\nabla \cdot \mathbf{A} = 0$, $\phi = 0$, and the fact that

$$\nabla \cdot (\mathbf{A}\Psi) = \mathbf{A} \cdot (\nabla\Psi) + (\nabla \cdot \mathbf{A}) \cdot \Psi \tag{2.24}$$

equation (2.20) is reduced to

$$i\frac{\partial}{\partial t}\Psi(\mathbf{r}, t) = \hat{H}\Psi(\mathbf{r}, t) \tag{2.25}$$

$$= \left[-\frac{1}{2}\nabla^2 - i\mathbf{A} \cdot \nabla + \frac{1}{2}\mathbf{A}^2 + V(\mathbf{r}) \right]\Psi(\mathbf{r}, t). \tag{2.26}$$

The components in the Hamiltonian as described in equation (2.25) can be understood as the summation of the atomic interaction and the interaction with field such that

$$\hat{H}_0 = -\frac{1}{2}\nabla^2 + V(\mathbf{r}) \tag{2.27}$$

$$\hat{H}_I = \hat{H} - \hat{H}_0 = -i\mathbf{A} \cdot \nabla + \frac{1}{2}\mathbf{A}^2. \tag{2.28}$$

2.3.1 Dipole Approximation

If we assume that the wavelength λ of the laser field is much larger than the atomic system, along with the intensity of the field not being too high, then we can neglect the spatial variation of the electromagnetic field the atomic system is subject to. Dropping the spatial dimension of the the laser field is known as the *dipole approximation*, that is to say the vector potential is only a time-dependent factor of the TDSE.

In order to see why this works, we can take the plane wave form of the vector potential in equation (2.13) with $\phi = 0$ and expand it in terms of its Taylor series with respect to position:

$$
\begin{aligned}
\mathbf{A}(\mathbf{r},t) &= \frac{1}{2i}\{\hat{\boldsymbol{\epsilon}}A_0 \exp[i(\mathbf{k}\cdot\mathbf{r}-\omega t)] - c.c.\} \\
&= \frac{1}{2i}\left\{\hat{\boldsymbol{\epsilon}}A_0 \exp(-i\omega t)\left(1 + i\mathbf{k}\cdot\mathbf{r} + \frac{1}{2!}(i\mathbf{k}\cdot\mathbf{r})^2 + \dots\right) - c.c.\right\}.
\end{aligned}
\tag{2.29}
$$

From here, the matrix element between the initial, $\langle\Psi_0|$, and final state, $|\Psi_f\rangle$, is

$$
\begin{aligned}
\langle\Psi_0|\hat{H}_I|\Psi_f\rangle &\propto \langle\Psi_0|\mathbf{A}\cdot\nabla|\Psi_f\rangle + \langle Psi_0|\mathbf{A}^2(\mathbf{r},t)|\Psi_f\rangle \\
&\propto \exp(-i\omega t)\hat{\boldsymbol{\epsilon}}\cdot\left(\langle\Psi_0|\nabla|\Psi_f\rangle + \langle\Psi_0|(i\mathbf{k}\cdot\mathbf{r})\nabla|\Psi_f\rangle\right. \\
&\quad \left.+ \frac{1}{2!}\langle\Psi_0|(i\mathbf{k}\cdot\mathbf{r})^2\nabla|\Psi_f\rangle\cdots - c.c.\right) + \langle Psi_0|\mathbf{A}^2(\mathbf{r},t)|\Psi_f\rangle.
\end{aligned}
\tag{2.30}
$$

For the majority of the laser parameters considered in this thesis, the matrix elements containing $\mathbf{k}\cdot\mathbf{r}$ are small compared to $\langle\Psi_0|\nabla|\Psi_f\rangle$ and the power series in $\mathbf{k}\cdot\mathbf{r}$ converges quickly and allowing us to neglect the spatial component of the electric field. Similarly for the $\mathbf{A}^2$ term in equation (2.30), dropping the spatial component $\mathbf{k}\cdot\mathbf{r}$ leaves a purely time dependent part of the interaction of the form

$$
\langle Psi_0|\mathbf{A}^2(\mathbf{r},t)|\Psi_f\rangle \approx \langle Psi_0|\mathbf{A}^2(t)|\Psi_f\rangle.
\tag{2.31}
$$

This quantity is equal to 0 unless state the final state f is equal to the initial state 0 and therefore does not contribute to the dynamics of the interaction within the dipole approximation.

Since $\mathbf{A}(\mathbf{r},t) = \mathbf{A}(t)$ in the dipole approximation, the Coulomb gauge is automatically satisfied along with the electric field and magnetic field being

defined as follows:

$$\mathbf{E}(t) = -\frac{d\mathbf{A}(t)}{dt} \tag{2.32}$$

and most importantly

$$\mathbf{B} = \nabla \times \mathbf{A}(t) = \mathbf{0}. \tag{2.33}$$

Equation (2.33) only remains a valid assumption, however, when the velocity of electrons in the continuum remain insignificant relative to the speed of light. Equations (2.14) and (2.15) tell us that

$$\frac{|B|}{|E|} = \frac{1}{c}. \tag{2.34}$$

The $\mathbf{v} \times \mathbf{B}$ component of the full Lorentz force, pulls the magnetic force back into the fray as the ratio v/c increases. Figure 2.1 points out the regions where non-dipole effects must be considered. An electron's maximum velocity in the continuum is a function of the field's wavelength and intensity. As such, the long wavelength regions of figure 2.1 highlight the necessity to include non-dipole terms. The upper dipole limit occurs when the wavelength of the field is comparable to the size of the atomic system, at which point spatial homogeneity can no longer be considered a reasonable assumption.

2.3.2 Gauge Transformations

For one-electron systems where $\hat{H}_0 = -\frac{1}{2}\nabla^2 + V(\mathbf{r})$, we may write

$$i\frac{\partial}{\partial t}\Psi(\mathbf{r}, t) = \left[\hat{H}_0 - i\mathbf{A} \cdot \nabla + \frac{1}{2}\mathbf{A}^2\right]\Psi(\mathbf{r}, t). \tag{2.35}$$

Within the dipole approximation, we can eliminate the term $\mathbf{A}^2$ using the
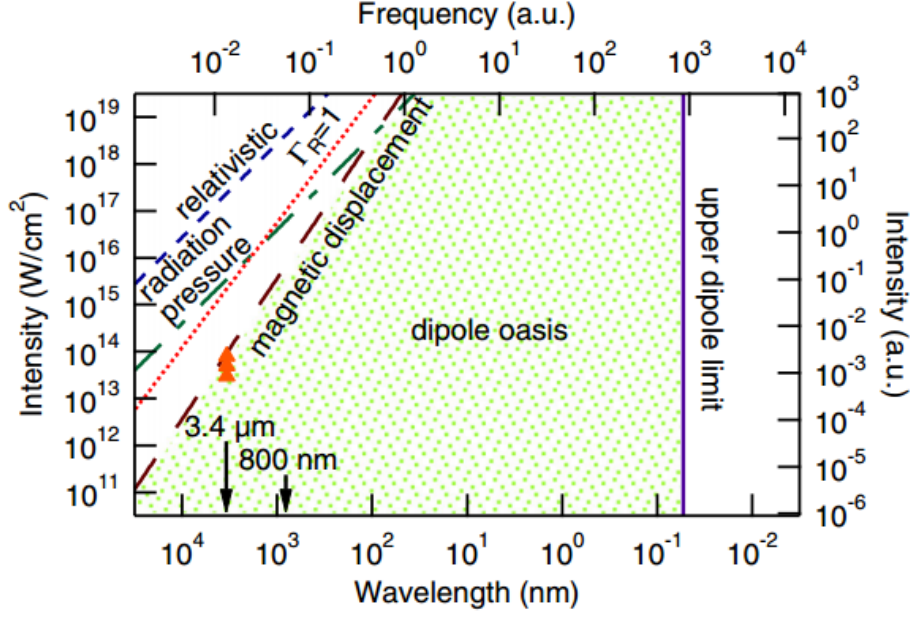
Figure 2.1: The wavelength-intensity parameter space for when the dipole approximation is valid [57].

gauge transformation

$$\Psi(\mathbf{r}, t) = e^{-\frac{i}{2} \int^{t} \mathbf{A}^2(t') dt'} \Psi^V(\mathbf{r}, t), \qquad (2.36)$$

yielding the *velocity* gauge form of the TDSE

$$i\frac{\partial}{\partial t}\Psi^V(\mathbf{r}, t) = \left[\hat{H}_0 - i\mathbf{A}(t) \cdot \nabla\right]\Psi^V(\mathbf{r}, t). \qquad (2.37)$$

Another gauge transformation that may be implemented is the *length* gauge by using the Göpert-Mayer transformation $\chi(\mathbf{r}, t) = \mathbf{A}(t)\cdot\mathbf{r}$. Within the dipole approximation $\mathbf{E}(t) = -\frac{d\mathbf{A}(t)}{dt}$ and along with equations (2.21) to (2.23) we have

$$\mathbf{A}'(t) = 0 \tag{2.38}$$

$$\phi' = -\mathbf{E}(t) \cdot \mathbf{r} \tag{2.39}$$

$$\Psi^L(\mathbf{r}, t) = e^{i\mathbf{A}(t) \cdot \mathbf{r}} \Psi^V(\mathbf{r}, t). \tag{2.40}$$

The TDSE in the length gauge then becomes

$$i\frac{\partial}{\partial t}\Psi^L(\mathbf{r}, t) = \left[\hat{H}_0 + \mathbf{E}(t) \cdot \mathbf{r}\right]\Psi^L(\mathbf{r}, t). \tag{2.41}$$

A gauge transformation is a unitary transformation on the TDSE and in theory should amount to measurable quantities being equal between the gauges. In practice, when approximations are made in the case of strong field approximations in particular (to be discussed shortly) or under certain conditions of the electric field, this is not the case. It is well known that the length gauge requires an increased number of angular momenta and basis functions to describe the electron dynamics faithfully when compared with propagation under the velocity gauge [23].

The canonical momentum in the length gauge is equal to the kinetic momentum of the electron, whereas the velocity gauge has canonical momentum equal to the kinetic momentum of the electron with the quantity $A(t)$ subtracted. This is equivalent to subtracting the classical momentum of the electron in an electromagnetic field, rendering the canonical momentum to vary slowly compared to the length gauge. Cormier and Lambropoulos [23] demonstrate this for hydrogen subject to a $619.88nm$ pulse with intensity $3.16 \times 10^{13} W/cm^2$ for 12 cycles in both gauges. The observed populations of the angular momentum numbers between the two gauges showed a clear advantage in using the velocity gauge. The length gauge populates the high angular momentum so-

mewhat equally, whereas the velocity gauge sees a very small number of angular momenta populated beyond what is considered non-negligible (see figure 2.2).
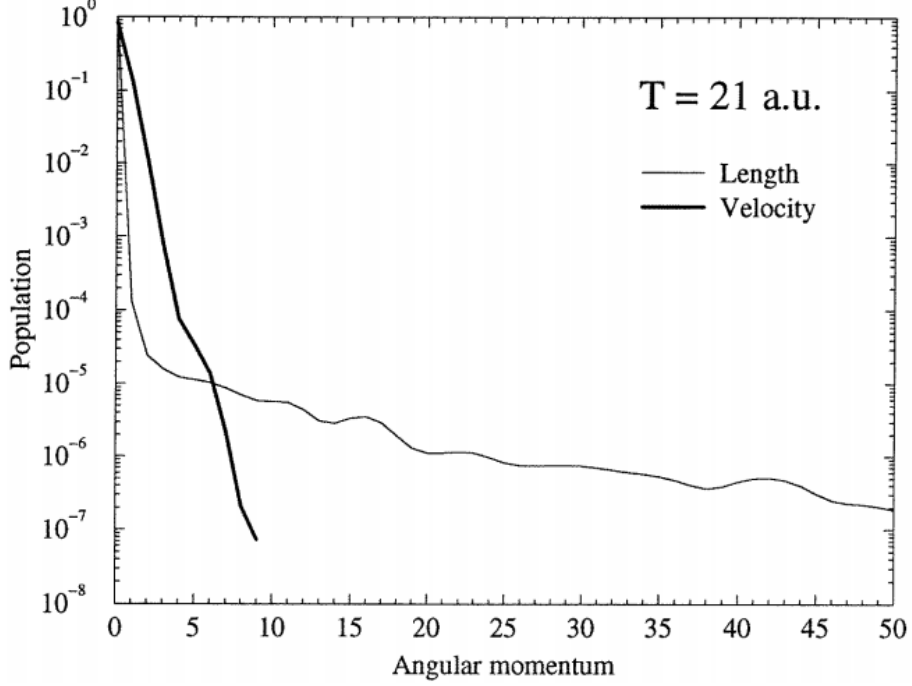
Figure 2.2: Distribution of the population of the wave function as a function of angular momentum l at a time $t = 21$ a.u. when the field, $E(t)$, is instantaneously 0 during the pulse [23].

2.4 Classical Motion in a Monochromatic Field

The Lorentz equation which governs the classical dynamics of an electron in an electromagnetic field is as follows [84]

$$\frac{d}{dt}\mathbf{p}_{cl} = -[\mathbf{E}(\mathbf{r}, t) + \mathbf{v} \times \mathbf{B}(\mathbf{r}, t)]. \tag{2.42}$$

Taking $\phi = 0$ in equation (2.5), employing the Coulomb gauge and neglecting relativistic effects, the momentum $\mathbf{p}_{cl} = \mathbf{v}$ in atomic units and $\mathbf{E}$ and $\mathbf{B}$ are

related to $\mathbf{A}$ by equations (2.5) and (2.6), respectively. Since we are working in the non-relativistic regime, it is true that $v/c \ll 1$, permitting us to omit the second term of equation (2.42). Making the assumption that the initial velocity of the electron is small enough that the displacement from its initial position $\mathbf{r}_0$ along the propagation direction remains much smaller than the carrier wavelength means that, in the long-wavelength limit, we have [46]

$$\frac{d}{dt}\mathbf{v} = -\mathbf{E}(\mathbf{r}_0, t). \tag{2.43}$$

Integrating equation (2.43) tells us the velocity of an electron with initial velocity $\mathbf{v}_0$ at time t_0

$$\begin{aligned}\mathbf{v}(t) &= -\int_{t_0}^{t} \mathbf{E}(\mathbf{r}_0, t')dt' + \mathbf{v}_0 \\ &= \mathbf{A}(\mathbf{r}_0, t) - \mathbf{A}(\mathbf{r}_0, t_0) + \mathbf{v}_0.\end{aligned} \tag{2.44}$$

The canonical momentum in the velocity gauge is

$$\mathbf{p} = \mathbf{v}(t) - \mathbf{A}(\mathbf{r}_0, t) \tag{2.45}$$

and so

$$\mathbf{p}(t) = \mathbf{p}(t_0) \tag{2.46}$$

which shows that the canonical momentum is conserved in the long-wavelength approximation in the velocity gauge. The classical motion of the electron is a superposition of the *quiver* motion and the *drift* motion defined as follows

$$\mathbf{v}_q(t) = \mathbf{A}(\mathbf{r}, t) \tag{2.47}$$

and

$$\mathbf{v}_d(t) = \mathbf{v}_0 - \mathbf{A}(\mathbf{r}_0, t_0) = \mathbf{p}_0. \tag{2.48}$$

The position of the electron at time t with initial velocity $\mathbf{v}_0$ and location $\mathbf{r}_0$ at time t_0 is found by integrating equation (2.44)

$$\mathbf{r} = \int_{t_0}^{t} \mathbf{A}(t')dt' + \mathbf{v}_0(t - t_0) + \mathbf{r}_0$$
$$= \alpha(t, t_0) + \mathbf{v}_0(t_0 - t) + \mathbf{r}_0 \tag{2.49}$$

where $\alpha(t, t_0)$, the quiver motion of the electron, is defined as

$$\alpha(t, t_0) = \int_{t_0}^{t} \mathbf{A}(\mathbf{r}_0, t')dt'. \tag{2.50}$$

For a linearly polarised laser field, the electron oscillates along the polarisation vector with amplitude $\alpha_0 = E_0/\omega^2 = A_0/\omega$.

2.4.1 Ponderomotive Energy

The *ponderomotive energy*, U_p, is an important parameter in laser-atom physics. It is defined as the cycle averaged quiver energy of the free electron in the field. Assuming the electron is at rest in a monochromatic field acting along the x-axis, where the field is defined as

$$\mathbf{E}(t) = E_0 \cos(\omega t)\hat{\boldsymbol{\epsilon}}_x \tag{2.51}$$

the kinetic energy is given by

$$E_k = \frac{E_0^2}{2\omega^2} \sin^2(\omega t) \tag{2.52}$$

and therefore the cycle averaged kinetic energy is

$$\langle E_k \rangle_T \equiv U_p = \frac{E_0^2}{4\omega^2} = \frac{I}{4\omega^2}. \tag{2.53}$$

The notation $\langle \rangle_T$ denotes the time averaging over one laser cycle $T = 2\pi/\omega$.

A *direct electron* is an electron that accrues enough kinetic energy to never return to the core. The maximum kinetic energy an electron can have when its motion is defined by equation (2.52) is $E_k^{dir,max} = 2U_p$, the maximum kinetic energy of an electron in a monochromatic field [59].

2.5   Volkov Solutions to the TDSE: An unbound electron in a laser field A(t)

Frequently, the solution of the free particle in a vector potential $\mathbf{A}(t)$ is required when modelling behaviour very far from the ion core, at which point the particle is considered asymptotically free. The quantum mechanical solution of a free electron in a laser field with vector potential $\mathbf{A}(t)$ in the dipole approximation are given by the *Volkov* states.

Let us consider a free electron in a laser field with vector potential $\mathbf{A}(t)$ within the dipole approximation. The motion of the electron is described by

$$i\frac{\partial}{\partial t}\psi_{\mathbf{k}}^{(Vv)}(\mathbf{r},t) = \hat{H}_F \psi_{\mathbf{k}}^{(Vv)}(\mathbf{r},t) \tag{2.54}$$

where, for $q = -1$,

$$\hat{H}_F(t) = \frac{1}{2}[\mathbf{p} + \mathbf{A}(t)]^2. \tag{2.55}$$

Applying the velocity gauge to equation (2.54) produces

$$i\frac{\partial}{\partial t}\psi_{\mathbf{k},V}^{(Vv)}(\mathbf{r},t) = \left[\frac{\mathbf{p}^2}{2} + \mathbf{A}(t)\cdot\mathbf{p}\right]\psi_{\mathbf{k},V}^{(Vv)}(\mathbf{r},t). \qquad (2.56)$$

Since $\hat{H}_F^V$ commutes with $\mathbf{p}$ and since $e^{i\mathbf{k}\cdot\mathbf{r}}$ is an eigenfunction of $\mathbf{p}$ correspon-
ding to the eigenvalue $\mathbf{k}$ in a.u., equation (2.56) admits the solution [46]:

$$\psi_{\mathbf{k},V}^{(Vv)}(\mathbf{r},t) = \frac{1}{(2\pi)^{\frac{3}{2}}}e^{i\mathbf{k}\cdot\mathbf{r}}f_{\mathbf{k}}(t). \qquad (2.57)$$

The Volkov states are plane waves with an oscillating phase dependent on
the vector potential $\mathbf{A}(t)$. Substituting equation (2.57) into equation (2.56)
produces the first order differential equation

$$i\frac{\partial}{\partial t}f_{\mathbf{k}}(t) = \left[\frac{k^2}{2} + \mathbf{k}\cdot\mathbf{A}(t)\right]f_{\mathbf{k}}(t) \qquad (2.58)$$

yielding solutions of the form:

$$f_{\mathbf{k}}(t) = Ce^{-iE_kt-i\mathbf{k}\cdot\boldsymbol{\alpha}(t)} \qquad (2.59)$$

where $E_k = \frac{k^2}{2}$ and

$$\boldsymbol{\alpha}(t) = -\int_{-\infty}^{t}\mathbf{A}(t')dt'. \qquad (2.60)$$

is the classical quiver amplitude of an electron in a laser field.

Choosing $C = 1$, we obtain from equation (2.57)

$$\psi_{\mathbf{k},V}^{(Vv)}(\mathbf{r},t) = \frac{1}{(2\pi)^{\frac{3}{2}}}e^{i\mathbf{k}\cdot[\mathbf{r}-\boldsymbol{\alpha}(t)]-iE_kt} \qquad (2.61)$$

with normalisation condition

$$\langle\psi_{\mathbf{k},V}^{(Vv)}|\psi_{\mathbf{k},V}^{(Vv)}\rangle = \delta(\mathbf{k}-\mathbf{k}'). \qquad (2.62)$$

The choice $C = \sqrt{k}$ in a.u. results in the 'energy normalisation' of the Volkov states

$$\langle \psi^{(Vv)}_{\mathbf{k}',V} | \psi^{(Vv)}_{\mathbf{k},V} \rangle = \delta(E_k - E'_k)\delta(\mathbf{k} - \mathbf{k}'). \tag{2.63}$$

2.6   Multiphoton Ionisation

Multiphoton processes were first observed in 1963 by Damon and Tomlinson [25] and again in 1965 by Voronov and Delone [83], who recorded two-photon electron detachment from the negative ion I⁻. The multiphoton regime is dominant when the photon energy is lower than the ionisation potential of the atom within the laser field, requiring a number of photon absorptions to ionise. For single electron atoms we have the multiphoton ionisation (MPI) reaction

$$n\omega + A^q \rightarrow A^{q+1} + e^- \tag{2.64}$$

where n is the number of photons absorbed and q is the charge of the atomic system.

2.6.1   Above Threshold Ionisation

In 1979, P. Agostini *et al* discovered that for sufficiently high intensities (I $>$ 10^{11} W/cm², the ionised electron can absorb more than the minimum number of photons required to enter the continuum [1]. This phenomena was called *above threshold ionisation* (ATI). The spectra in [1] were seen to exhibit several peaks at

$$E_s = (n + s)\omega - I_p \tag{2.65}$$

separated by the photon energy ω, where n is the minimum number of photons needed to exceed the ionisation potential I_p and s is the excess number of photons absorbed.

An experimental example of ATI spectra measured in 1988 by G. Petite *et al* [67] is shown in figure 2.3. At weak intensities we find the intensity dependence of the peaks follows the *lowest order perturbation theory* (LOPT) prediction that the ionisation rate for an $(n+s)$ photon-process is proportional to I^{n+s}. For higher intensities, we find the LOPT prediction breaking down as peaks at higher energies arise where a disproportionate number of excess photons have been absorbed.

We may also remark on the fact that the low energy peaks have been noticeably suppressed. This is due to the *Stark shifting* of the atomic states in the presence of the laser field. The (AC) Stark shift of a system is the effect of the electric field on the energy levels of the atomic states. Relative to the electric field, electrons that are strongly bound to the ion core are barely affected by the Stark shift of the system. On the other hand, induced Stark shifts of the Rydberg and continuum states are given by the electron ponderomotive energy $U_p = E_0^2/4\omega^2$, described in section 2.4.1 as the cycle-averaged kinetic energy of an electron in a laser field.

For a wavelength of $\lambda = 1064$nm, U_p becomes equal to the photon energy at approximately $I = 10^{13}$W/cm^2. Since the continuum states are shifted upwards by U_p relative to the lower bound states, we find that there is a corresponding increase in the intensity-dependent ionisation potential of the atom such that $I_p(I) \approx I_p + U_p$. If $n\omega < I_p + U_p$ then ionisation by n photon absorption is energetically forbidden, however, for smoothly varying pulses, the electron is subject to a range of intensities and a dampening rather than a nullification of low energy peaks is observed.

The intensity profile for a pulse can vary both in time and space in a realistic experiment. The variation in space leads to a *ponderomotive force* and one can account for its effect on the ATI spectrum in figure 2.3 (see section 1.3 and subsection 2.2.2 in [46]).
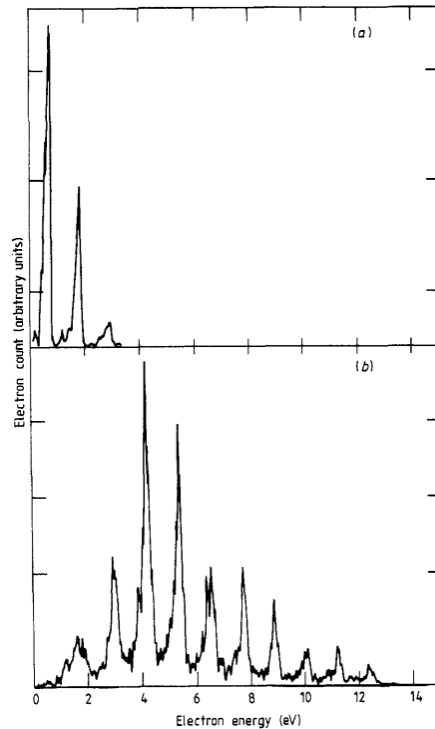
Figure 2.3: Electron energy spectra showing ATI of xenon subject to a laser with wavelength $\lambda = 1064$nm. Top: $I = 2 \times 10^{12}$W/cm^2. Bottom: $I = 10^{13}$W/cm^2 [67].

2.7 Tunnelling and Barrier Suppression Ionisation

If the frequency is low enough and the intensity of the field is large enough to mean that the electric field is comparable to the Coulomb potential, then we can interpret ionisation using a quasi-static model. The bound electron experiences the sum of the Coulomb potential and the instantaneous electric

field in the length gauge (i.e. $E(t) \cdot \mathbf{r}$) to form an effective potential, an illustration of which can be seen in figures 2.4 and 2.5.
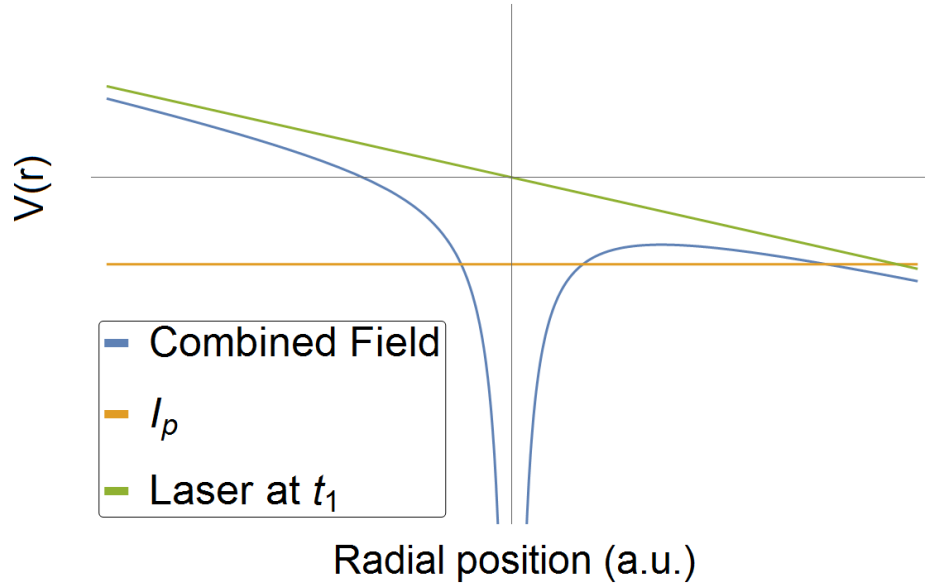
Figure 2.4: Classically forbidden tunnelling ionisation.
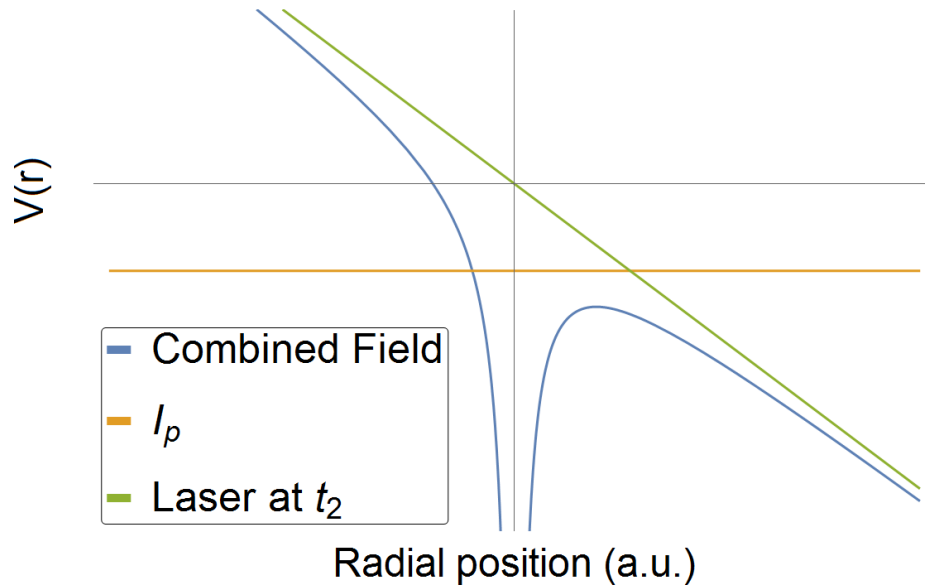
Figure 2.5: Barrier suppression ionisation.

The diagram in figure 2.4 is a one dimensional depiction of tunnelling ionisation, whereby the electric field at time t_1 suppresses the effective barrier to

the point at which tunnelling may occur. Tunnelling is most prevalent during the peaks of the electric field when it lowers the potential barrier resulting in periodic bursts of ejected electrons.

Figure 2.5 displays *barrier suppression ionisation* (BSI) or *over the barrier ionisation* (OBI) which occurs when the electric field at time t_2 has become strong enough to lower the effective barrier enough for the electron to ionise without the need for tunnelling.

2.7.1 Keldysh Parameter

Since it is possible for ionisation to occur under different circumstances (multiphoton, tunnelling or BSI), it would be useful to know prior to a calculation which form of ionisation we would expect to observe. Keldysh [52] defined the dimensionless quantity γ, the *Keldysh parameter*, to distinguish between these separate regimes. Keldysh considered the ratio of the characteristic time for tunnelling, T_t, to the characteristic time of the laser field (the period T):

$$\gamma = \frac{T_t}{T} = \frac{\omega}{w_t} = \frac{\omega\sqrt{2I_p}}{E_0} = \sqrt{\frac{I_p}{2U_p}}. \qquad (2.66)$$

When $\gamma \gg 1$ then multiphoton processes dominate ionisation and when $\gamma \ll 1$ then we find tunnelling through a static barrier is the dominant process for ionisation. The peak electric field required to enter the BSI regime is

$$E_{BSI} = \frac{E_n^2}{4Z} = \frac{Z^3}{16n^4} \qquad (2.67)$$

where $E_n = Z^2/2n^2$ is the binding energy of the atom. With this parameter, we can further distinguish the processes that lead to ionisation. If $E_0 < E_{BSI}$ and $\gamma \ll 1$, then adiabatic tunnelling becomes the prevalent mechanism for ionisation whereby the electron escapes along the instantaneous direction of

the electric field, ignoring any oscillations and rotations of the electric field during the tunnelling time. On the other hand, if $E_0 \geq E_{BSI}$ and $\gamma \ll 1$, then we should find ourselves in the barrier suppression ionisation regime since the electric field is strong enough to completely overcome the Coulomb at peak amplitude.

If however we find $\gamma \approx 1$ and $E_0 < E_{BSI}$, then we enter the non-adiabatic tunnelling regime. This regime drops the assumption that the field has frequency low enough to discount the effects of its oscillatory and rotational behaviour during the 'time' the electron spends tunnelling through the no longer static barrier.

2.8 Three Step Model

The following model provides an intuitive picture of the ionisation process and has been very successful in interpreting a broad range of processes in strong field ionisation.

The *three step model* assumes that tunnelling plays a role in the ionisation process (i.e. $\gamma \leq 1$) and that at the moment of ionisation, the electron has tunnelled through the barrier and has initial velocity $\mathbf{v} = 0$. Once in the continuum, the effect of the Coulomb potential is neglected.

As the name suggests, the ionisation process is broken into three steps:

1. The Coulomb potential combines with the slowly oscillating laser field to create a barrier in the direction of the field. The electron tunnels through this barrier at which point the atomic potential can be neglected. The tunneling is treated quantum mechanically or semi-classically.

2. Once the electron is in the continuum, its motion is then dictated by the

laser field. When the field switches direction, the electron is accelerated back towards its parent-ion.

3. At the point of recollision, three scenarios may occur: the electron scatters elastically; scatters inelastically, which may lead to multiple ionisations and inner shell excitations of the atom; or it can radiatively recombine into an empty bound state of the ion, releasing a photon with energy $\omega = E_k + I_p$, where E_k is the energy gained by the laser field. This final scenario is known as *high harmonic generation.*

Classical calculations predict that the maximum kinetic energy the electron can accrue directly in the laser field is $2U_p$. If the electron is to scatter elastically when recolliding with the parent-ion, then the maximum kinetic energy an electron can gather occurs when it backscatters at an angle of $180°$ with a maximum electron energy of $10U_p$. Note that this is the maximum classical energy possible following recollision, there will be a range of electron energies between $2U_p$ and $10U_p$ determined by the time at which ionisation occurs and the time recollision occurs.

If the electron is to recombine with the parent-ion, the highest energy photon will be emitted when the electron has gathered the largest possible kinetic energy in the laser field at the moment the electron recombines. Classical mechanics tells us the highest possible photon energy under these circumstances is $\omega = I_p + 3.17U_p$.

In a regime whereby non-dipole effects can be discounted, atoms interacting with many cycle laser fields incur the generation of high order harmonics when the electron recombines with the core. At the point of recombination, the atom responds in a nonlinear way, emitting coherent radiation at frequencies equal to odd integer multiples of the laser frequency due to inversion symmetry of

the atom [76].

2.9   Strong Field Approximation

The final topic we shall discuss briefly before moving onto methods of solving the TDSE is the *Strong Field Approximation* SFA, a simple and approximate theoretic approach to the problem of laser-atom interactions. The general principle of the SFA is that the initial bound state of the atom is unaffected by the laser field up to some time t' at which point ionisation occurs, while the final state in the continuum neglects the Coulomb potential entirely or is treated as a perturbation [52], [65]. This model assumes that the field is strong enough to ionise directly from the initial state, ignoring any and all intermediary excited states of the atom.

The ionisation amplitude describing the above simplified hypothesis for an electron ejected with momentum $\mathbf{p}$ is given by

$$M_{\mathbf{p},x}(t_i, t_f) = -i \int_{t_i}^{t_f} dt' \, \langle \psi_{\mathbf{p},x}^{(Vv)}(t_f) | H_{I,x}(t') | \psi_0(t_i) \rangle \qquad (2.68)$$

where ψ_0 is the initial state and $\psi_{\mathbf{p},x}^{(Vv)}$ is the Volkov state of an electron with momentum $\mathbf{p}$ in the continuum described in section 2.5. $H_{I,x}(t)$ is the laser-atom interaction term usually expressed in the length gauge. Time t' is the time at which ionisation takes place and so the point at which the binding potential is neglected in favour of the electric field [11]. Unlike the TDSE, the SFA is gauge-dependent. The subscript x in equation (2.68) denotes the choice of gauge, either $x = L$ or $x = V$ for the length or velocity gauge, respectively. The results produced by equation (2.68) differ significantly when selecting a different gauge. A more general theory derived by Perelomov, Popov, and Terentev (PPT), which shall be discussed further in Chapter 4, eliminates the

gauge dependence of the SFA.

Equation (2.68) may be recast using integration by parts into

$$M_{\mathbf{p},x} = -i \int_{t_i}^{t_f} dt' \, \langle \psi_{\mathbf{p},x}^{(Vv)}(t_f) | V(\mathbf{r}) | \psi_0(t_i) \rangle \qquad (2.69)$$

which depends on the gauge only via the final Volkov state by

$$\langle \mathbf{r} | \psi_{\mathbf{p},V}^{(Vv)} \rangle = \frac{e^{-iS_{\mathbf{p}(t)}}}{(2\pi)^{\frac{3}{2}}} e^{i\mathbf{p}\cdot\mathbf{r}} \qquad (2.70)$$

in the velocity gauge and

$$\langle \mathbf{r} | \psi_{\mathbf{p},L}^{(Vv)} \rangle = \frac{e^{-iS_{\mathbf{p}(t)}}}{(2\pi)^{\frac{3}{2}}} e^{i[\mathbf{p}+\mathbf{A}(t)]\cdot\mathbf{r}} \qquad (2.71)$$

in the length gauge where the action $S_{\mathbf{p}}(t)$ is defined as

$$S_{\mathbf{p}(t)} = \frac{1}{2} \int^t d\tau [\mathbf{p} - \mathbf{A}(t)]^2. \qquad (2.72)$$

Substituting the length gauge form into equation (2.68) and using saddle point methods for the integral, we can connect the results with the three step model involving tunnelling and semi-classical interpretations of the ionisation process.

Solution of the Time Dependent Schrödinger Equation for Short Pulses

3.1   Introduction

There exist semi-classical and perturbative methods such as SFA that are able to accurately describe the interaction between electromagnetic fields and atoms for certain frequencies and intensities. For example, perturbation theory relies on a laser pulse that is not too intense and a frequency that is not too high or low so as to induce non-dipole or even relativistic effects. Restrictions to semi-classical methods also include the shape and length of the pulse. If we do not wish to impose any fixed shape and length on the pulse (within reason) and relax the restrictions on the intensity and frequency that the field may take, we must look outside of perturbative methods to solve the TDSE. One major non-perturbative method is the direct numerical integration of the time-dependent Schrödinger equation. It is important to note that depending on the characteristics of the electromagnetic field, direct integration may require large numbers of grid points or functions in basis sets to accurately represent the wave function during and after the pulse, which can mean computationally expensive calculations. Direct numerical integration is often limited to single

electron atom interactions.

In order to broaden the reach of this method to many electron atoms, one may employ the *single active electron* (SAE) approximation which assumes that the laser only interacts with the outer most electron and the electron's interaction with the atom is represented by an effective potential $V(\mathbf{r})$. This approximation is most applicable to the alkali metals since the valence electron sits outside a closed shell, but it is also effective to apply it to atoms where the probability of multiple excitations is small. Therefore, atomic systems where the SAE approximation is effective require that the single active electron has a very high probability to be completely ionised by sequential processes before the next is even excited [75].

The SAE reduces the problem of many electron interactions to a one-electron equation which provides both a significant reduction in complexity, as well as bound state plus continuum state superposition solutions. The obvious disadvantage to the SAE is that it completely ignores electron-electron interactions which may lead to non-sequential multiple ionisation.

This section explores a number of methods to find the full solution, $\Psi(\mathbf{r}, t)$, for all points in space and time, to the TDSE

$$i\frac{\partial}{\partial t}\Psi(\mathbf{r}, t) = \hat{H}\Psi(\mathbf{r}, t) \tag{3.1}$$

where atomic units have been used.

Two problems need to be faced: firstly, the representation of $\Psi(\mathbf{r}, t)$ in space at any time t and secondly, its propagation in time from some initial state $\Psi(\mathbf{r}, t_0)$. There are broadly two methods which are used to represent the wave function in space: grid based methods, where space is divided into a discrete uniform grid or basis set methods, where the wave function is expanded

in a fixed basis with coefficients which depend on time. We will mainly use the latter, however, we introduce the former by first describing a widely used time propagation scheme before describing the Biconjugate Gradient Stabilised method (BiCGSTAB) method, the method of propagation to be used within this body of work.

3.1.1 Finite Difference Methods

Explicit and Implicit Methods

Suppose we have the solution to a differential equation, u_j, at point j. We can calculate the solution at the next point u_{j+1} from quantities that we have already. For a clearer example, suppose we have a simple differential equation:

$$y' = -cy. \tag{3.2}$$

We may approximate the solution to equation (3.2) from known solution y_j with the *Forward-Euler* scheme [70]

$$y_{j+1} = (1 - ch)y_j \tag{3.3}$$

where $h > 0$ denotes the step size. While very simple to implement, explicit schemes are inherently unstable. By choosing $h > c/2$, we can see that $|y_j| \to \infty$ as $j \to \infty$. Therefore large values for c would necessitate tiny step sizes. Figure 3.1 below showcases this instability for the parameters $c = 2$ and $h = 1.001 > 2/c$.

Implicit schemes trade longer computation for stability. Solving equation (3.2) with the *Back-Euler* scheme, whereby the right-hand side of the equation is evaluated at a new location by

Figure 3.1: This figure highlights the importance of choosing h small enough to avoid problems with stability.

$$y_{j+1} = \frac{y_j}{1 + ch},\tag{3.4}$$

we can see that as $h \to \infty$, $y_{j+1} \to 0$. This stability for all step sizes is not general for all implicit schemes, in fact it is only true for linear systems. However, in general, stability of solutions to implicit schemes is better than solutions to explicit schemes and therefore are better suited to deal with stiff sets of equations.

3.2   Schrödinger Equation in 1 Dimension

The Crank-Nicolson scheme [24] was developed in 1946 by John Crank and Phyllis Nicolson to provide a novel way to solve partial differential equations, in particular Crank and Nicolson were interested in the solution to the equations describing the diffusion of heat.

At its core, the scheme proposed by Crank and Nicolson combines the stability of an implicit scheme with second order accuracy in space and time by averaging the explicit and implicit *Forward Time Centered Space* differencing

schemes [70].

As an example, consider the TDSE in one dimension

$$i\frac{\partial}{\partial t}\Psi(x,t) = \mathbf{H}\Psi(x,t), \tag{3.5}$$

where $\mathbf{H}$ doesn't depend explicitly on time.

Equation (3.5) admits the solution

$$\Psi(x,t) = \exp(-i\mathbf{H}t)\Psi(x,0), \tag{3.6}$$

where $\Psi(x,0)$ is the initial wave function at time $t = 0$. Discretising the wave function over an equally spaced mesh in space and time such that $\Psi(x_i, t_j) = \psi_i^j$, we may form an explicit scheme to compute ψ_i^{j+1} from ψ_i^j:

$$\psi_i^{j+1} = (1 - i\mathbf{H}\delta t)\psi_i^j. \tag{3.7}$$

By multiplying equation (3.6) by $\exp(i\mathbf{H}(t))$, we can calculate ψ_i^{j+1} implicitly from ψ_i^j using

$$\psi_i^{j+1} = (1 + i\mathbf{H}\delta t)^{-1}\psi_i^j. \tag{3.8}$$

At each time step, both equations (3.7) and (3.8) do not preserve the norm of the wave function and so, the wave function must be renormalised at each time step. Combining equations (3.7) and (3.8), we arrive at the Cayley-Klein form [37] for the time evolution operator which preserves the norm and is second order accurate in time:

$$\exp(-i\mathbf{H}t) \approx \frac{1 - \frac{1}{2}i\mathbf{H}\delta t}{1 + \frac{1}{2}i\mathbf{H}\delta t}. \tag{3.9}$$

Hence,

Figure 3.2: Plot of $|\Psi(x)|^2$ of ground state hydrogen in one dimension subject to a linearly polarised 10 cycle pulse with $\omega = 0.7$ (a.u.) (see equation (3.21)) and intensity $I = 3.509 \times 10^{14}$ W/cm^2 computed using the Crank-Nicolson method in equation (3.10).

$$(1 + \frac{1}{2}i\mathbf{H}\delta t)\psi_i^{j+1} = (1 - \frac{1}{2}i\mathbf{H}\delta t)\psi_i^{j}. \qquad (3.10)$$

Note, that this equation also holds for $\mathbf{H} = \mathbf{H}(t)$ where we assume $\mathbf{H}(t)$ is constant in the time interval δt. Usually $\mathbf{H}(t)$ is evaluated at the mid-point of the interval.

The right hand side of equation (3.10) requires a matrix vector multiplication while the left hand side requires the solution of a tridiagonal system of linear equations in order to fully recover ψ_i^{j+1}. Figure 3.2 is the result of a 3000 point mesh in a box of size $x \in [-125, 125]$ using equation (3.10) calculated in the length gauge.

3.3 Basis Methods

In this approach the wave function can be represented in terms of an expansion of a complete square-integrable set of basis states $\psi_k(\mathbf{r})$

$$\Psi(\mathbf{r}, t) = \sum_{k=1}^{N} a_k(t)\psi_k(\mathbf{r}). \tag{3.11}$$

As usual, the computational complexity to solve equation (3.1) is a high priority and so, the expansion of the wave function must be truncated. The key to basis state methods is to find the least number of basis states needed to accurately represent the wave function during and after the pulse. We represent the $\psi_k(\mathbf{r})$ in spherical coordinates and the angular part of the basis is represented by the spherical harmonics $Y_{l,m}(\theta, \phi)$. We will focus on two radial bases: Coulomb-Sturmian functions and B-Splines.

3.3.1 Sturmian Functions

The choice of basis heavily influences the number of basis functions one requires to accurately represent the wave function. The Coulomb-Sturmian basis, referred to here as simply the Sturmian basis, are the solutions of the Sturm-Liouville equation

$$\left(-\frac{1}{2}\frac{d^2}{dr^2} + \frac{l(l+1)}{2r^2} - \frac{\kappa n}{r} + \frac{\kappa^2}{2} \right) S_{n,l}^{\kappa}(r) = 0. \tag{3.12}$$

Equation (3.12) bears close resemblance to the reduced radial Schrödinger equation for the Hydrogen atom

$$\left(-\frac{1}{2}\frac{d^2}{dr^2} + \frac{l(l+1)}{2r^2} - \frac{1}{r} \right) u_{n,l}(r) = E_n u_{n,l}(r) \tag{3.13}$$

where $u_{n,l}(r) = rR_{n,l}(r)$. In fact, by choosing $\kappa = \frac{1}{n}$, we find that $S^{\kappa}_{n,l}(r) = R_{n,l}(r)$. This displays the close relationship between the Sturmian functions and the hydrogenic radial wave functions. However, Sturmians form a complete (discrete) set as opposed to the hydrogenic functions which require the continuum states for completeness. The Sturmian functions are given by [35]

$$S^{\kappa}_{n,l}(r) = N^{\kappa}_{n,l} r^{l+1} e^{-\kappa r} L^{2l+1}_{n-l-1}(2\kappa r) \tag{3.14}$$

where n and l are the principal quantum number and orbital angular momentum, respectively and where

$$N^{\kappa}_{n,l} = \sqrt{\frac{\kappa}{n}} (2\kappa)^{l+1} \sqrt{\frac{(n-l-1)!}{(n+l)!}} \tag{3.15}$$

is chosen such that

$$\int_0^{\infty} S^{\kappa}_{n,l}(r) S^{\kappa}_{n,l}(r) dr = 1. \tag{3.16}$$

The parameter κ acts as a dilation parameter. By increasing the value of κ the quantity $e^{-\kappa r}$ becomes more prevalent and suppresses behaviour further from the origin, decreasing the value of κ has the opposite effect.

Comparing figures 3.3 and 3.4, there is a stretch of factor 2 when halving the dilation parameter κ. Therefore as well as the total number of Sturmians (denoted by N) in the basis set that will determine the size of the 'box' a calculation uses, one may also tweak κ to manipulate the box size, too. The range of the functions is approximately

$$r = \frac{2N}{\kappa} \tag{3.17}$$

the approximate outer turning point.
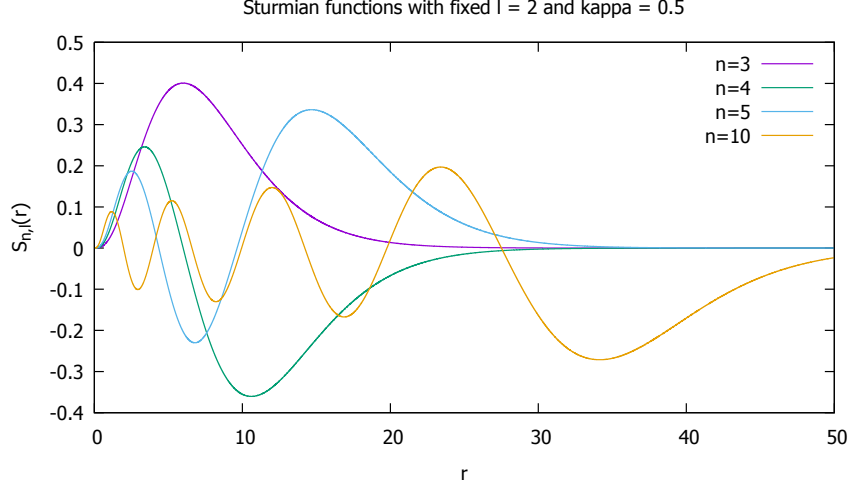
Figure 3.3: Sturmian functions with fixed $l = 2$ and $\kappa = 0.5$
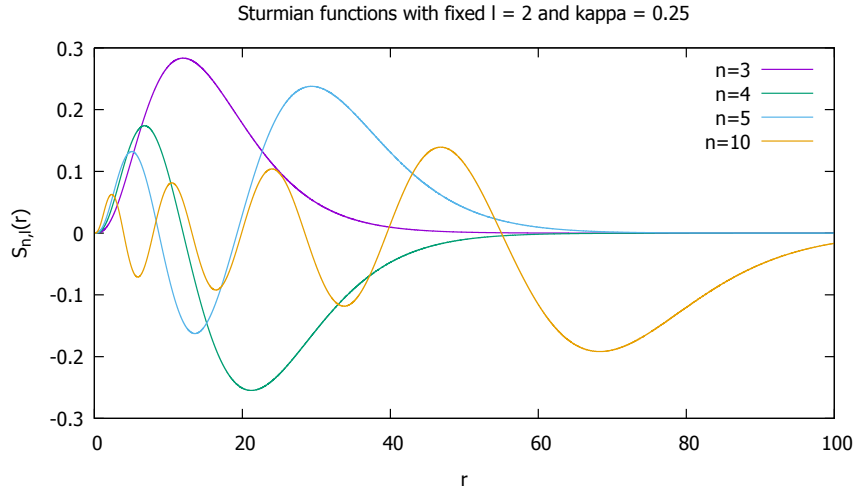
Figure 3.4: Sturmian functions with fixed $l = 2$ and $\kappa = 0.25$

For hydrogen in a laser field, the Sturmian representation of the wave function is in general then

$$\Psi(\mathbf{r}, t) = \sum_{n,l,m} a_{n,l,m}(t) \frac{S_{n,l}^{\kappa}(r)}{r} Y_{l,m}(\theta, \phi). \tag{3.18}$$

We will also usually require the 'atomic' basis (i.e. the field free states) to calculate excitation probabilities by projecting the atomic states onto the wave packet at the end of the pulse. The field free Hamiltonian, H_0, and eigenvalue

Spread of eigenvalues for increasing number of Sturmians with kappa fixed at 0.3
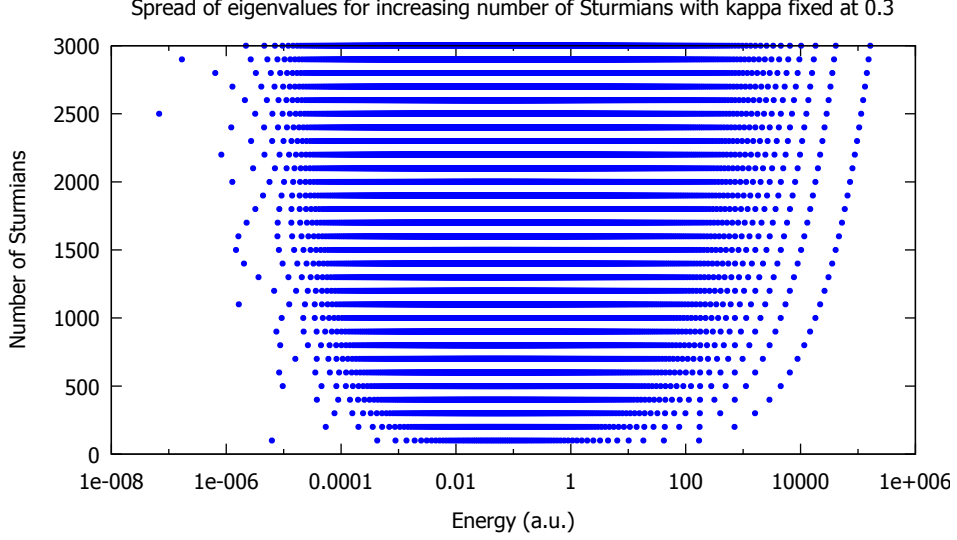
Figure 3.5: Density of positive eigenvalues as the number of Sturmians is increased incremented by 100.

equation is

$$\mathbf{H}_0 \Psi_n(\mathbf{r}) = E_n \mathbf{S} \Psi_n(\mathbf{r}), \tag{3.19}$$

whose solution gives the atomic states or basis.

Since the Sturmian functions are not orthogonal, the overlap matrix $\mathbf{S}$ is present on the right hand side of equation (3.19). When it comes to calculating observables after the pulse, the density of states in the continuum that the basis set occupies is something that must be taken into account. A density of states that is too low around a certain energy region will result in an inaccurate representation of the continuum.

To highlight the need to choose N large enough to include the energies a calculation will require, figure 3.5 displays the density of eigenvalues against increasing N. If the maximum expected electron energy will be no greater than 1 a.u., then 100 Sturmians would suffice, if the maximum expected electron energy is larger than 1 a.u., then N must be increased accordingly.
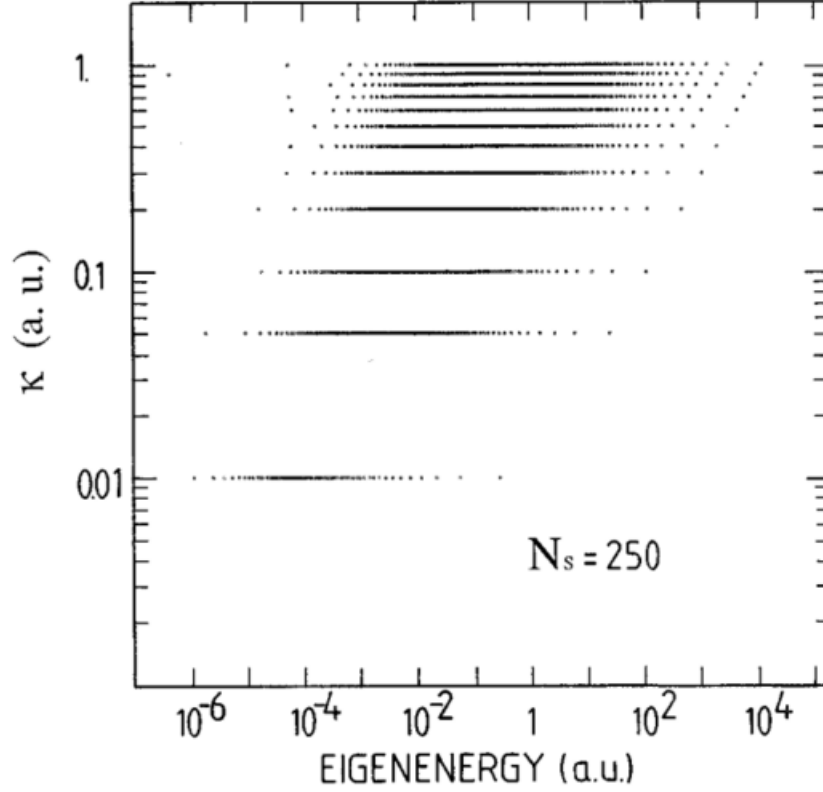
Figure 3.6: Density of eigenvalues with fixed N and varying κ. [41]

Changing the scope of the energy density does not just depend on the size of the basis. In the same way that κ also influences the size of the box, it also has an effect on the positive eigenvalues of the system as shown in figure 3.6.

3.3.2 Calculations Involving Sturmian Functions

When it comes to considering the problem of hydrogen subject to a linearly polarised laser pulse with frequency ω and phase ϕ in three dimensions within the velocity gauge, we must solve the Schrödinger equation

$$i\frac{\partial}{\partial t}\Psi(\mathbf{r}, t) = \left(-\frac{1}{2}\nabla^2 - \frac{1}{r} - i\mathbf{A}(t) \cdot \nabla \right)\Psi(\mathbf{r}, t). \qquad (3.20)$$

We use a 'sine squared pulse'

$$\mathbf{A}(t) = A(t)\mathbf{e}_z = A_0 \sin(\omega t + \phi) \sin^2\left(\frac{\omega t}{2N}\right)\mathbf{e}_z \qquad (3.21)$$

within the dipole approximation, where $0 < t < \tau$ and $\tau = 2N\pi/\omega$ is the pulse duration defined in terms of the number of cycles N and the frequency of the pulse ω. Unless stated otherwise, the phase, ϕ, is set to 0.

Within the velocity gauge, the Sturmian functions produce an extremely sparse Hamiltonian. The interaction blocks are 2-banded and the field free blocks are 3-banded which, in total, yields a 7-banded Hamiltonian.

Using equation (3.18) to replace Ψ in equation (3.20), the matrix elements of the Hamiltonian and the overlap matrix are analytical [41]. Note that due to the selections rules associated with linearly polarised light, the wave function Ψ is defined only in terms of a sum over n and l since m is constant. The diagonal block elements of the overlap matrix are:

$$(\mathbf{S})_{n,n}^l = 1 \qquad (3.22)$$

$$(\mathbf{S})_{n-1,n}^l = -\frac{1}{2}\sqrt{\frac{(n+2l)(n-1)}{(n+l)(n+l-1)}} \qquad (3.23)$$

$$(\mathbf{S})_{n+1,n}^l = -\frac{1}{2}\sqrt{\frac{n(n+2l+1)}{(n+l)(n+l+1)}}. \qquad (3.24)$$

The elements of diagonal blocks of the Hamiltonian are:

$$(\mathbf{H})_{n,n}^{l} = \frac{\kappa^2}{2} - \frac{\kappa}{n+l} \tag{3.25}$$

$$(\mathbf{H})_{n-1,n}^{l} = \frac{\kappa^2}{4}\sqrt{\frac{(n+2l)(n-1)}{(n+l)(n+l-1)}} \tag{3.26}$$

$$(\mathbf{H})_{n-1,n}^{l} = \frac{\kappa^2}{4}\sqrt{\frac{n(n+2l+1)}{(n+l)(n+l+1)}}. \tag{3.27}$$

The off-diagonal blocks require the resolution of the integral

$$\langle S_{n',l'}^{\kappa}Y_{l',m'}| - i\mathbf{A}(t)\cdot\nabla|S_{n,l}^{\kappa}Y_{l,m}\rangle = -\, iA(t)\sqrt{\frac{4\pi}{3}}\kappa(n'-n)$$
$$\times\,\langle S_{n',l'}^{\kappa}|S_{n,l}^{\kappa}\rangle\,\langle l',m'|Y_{1,0}|l,m\rangle\,. \tag{3.28}$$

After some calculations we arrive at the matrix elements for the interaction blocks of the Hamiltonian:

$$(\mathbf{H}_0)_{n,n}^{l-1,l} = -\frac{iA(t)l}{2\sqrt{(2l-1)(2l+1)}}\sqrt{\frac{(n+2l)(n+2l-1)}{(n+l)(n+l-1)}} \tag{3.29}$$

$$(\mathbf{H}_0)_{n+2,n}^{l-1,l} = \frac{iA(t)l}{2\sqrt{(2l-1)(2l+1)}}\sqrt{\frac{n(n+1)}{(n+l)(n+l+1)}} \tag{3.30}$$

$$(\mathbf{H}_0)_{n,n}^{l+1,l} = \frac{iA(t)(l+1)}{2\sqrt{(2l+1)(2l+3)}}\sqrt{\frac{(n+2l+1)(n+2l+2)}{(n+l)(n+l+1)}} \tag{3.31}$$

$$(\mathbf{H}_0)_{n-2,n}^{l+1,l} = -\frac{iA(t)(l+1)}{2\sqrt{(2l+1)(2l+3)}}\sqrt{\frac{(n-1)(n-2)}{(n+l)(n+l-1)}}. \tag{3.32}$$

With the matrix elements at hand, the results shown in figure 3.7 were obtained in previous work by propagating equation (3.20) using the Arnoldi time propagator [73] in the atomic basis (the eigenstates of H_0) to avoid dealing with the overlap matrix for Sturmians.
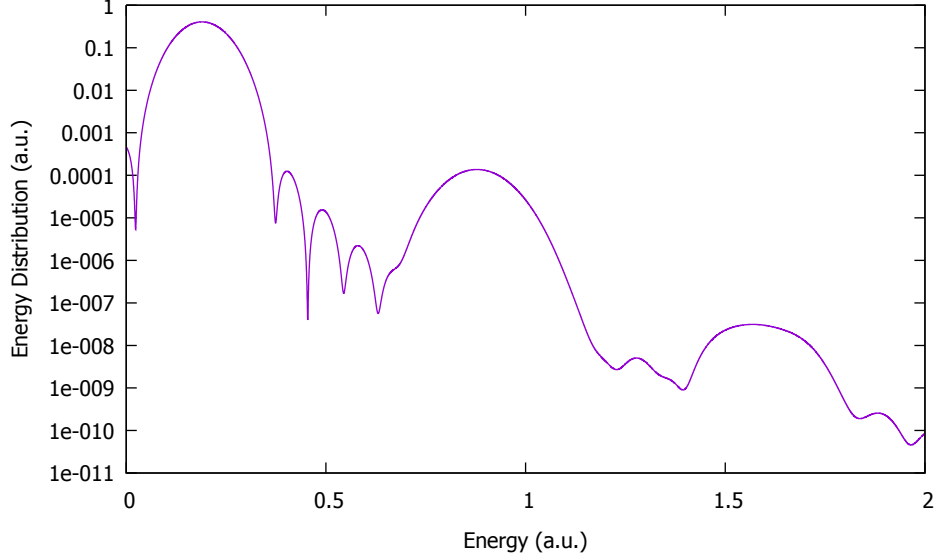
Figure 3.7: The energy distribution in logarithmic scale for the simulation of ground state hydrogen subject to an 8 cycle linearly polarised field with intensity $I = 10^{14}$ W/cm^2 and frequency $\omega = 0.7$ (a.u.) involving 8 angular momenta, 250 Sturmian functions per angular momentum with $\kappa = 0.3$. Note the ATI peaks at 0.9 and 1.6 a.u.

While more complicated, analytic expressions for the elements of the Hamiltonian in elliptically polarised fields can be derived when using Sturmian functions, too. Figure 3.8 below shows the energy distribution for comparable parameters to the case above, but for a circularly polarised laser field and calculated using the Crank-Nicolson time propagation method to be described in subsection 3.6.1, the electromagnetic field is defined as

$$\mathbf{A}(t) = (-A_x \sin(\omega t + \phi)\mathbf{e}_x + A_y \cos(\omega t + \phi)\mathbf{e}_y)\sin^2\left(\frac{\omega t}{2N}\right) \quad (3.33)$$

for $0 < t < 2N\pi/\omega = \tau$.
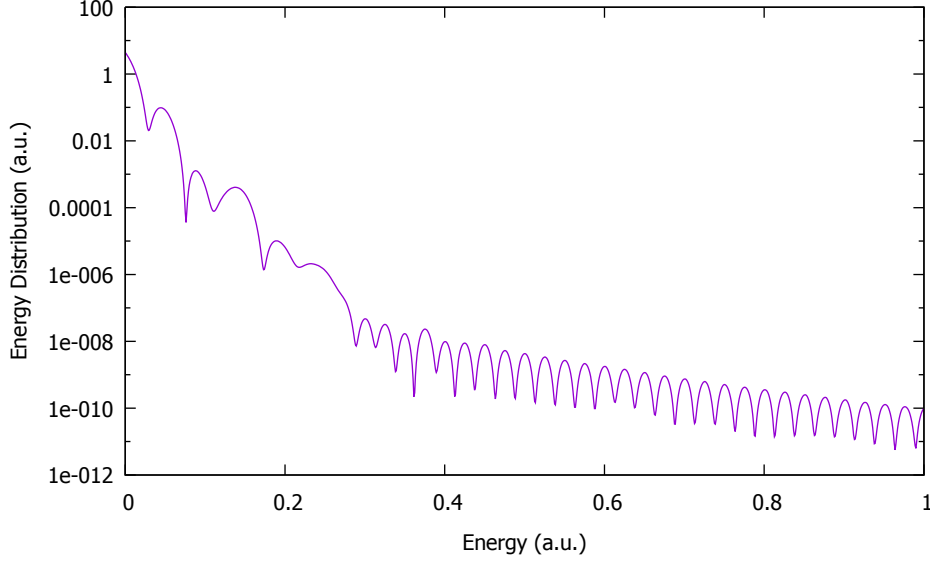
Figure 3.8: The energy cross section for the simulation of ground state hydrogen subject to an 8 cycle circularly polarised field with intensities $I_x = I_y = 10^{14}$W/cm^2 and frequency $\omega = 0.7$ (a.u.) involving 8 angular momenta, 250 Sturmian functions per angular momentum with $\kappa = 0.3$

3.3.3 B-Spline Basis

The Sturmians as a basis are rather restricted to the hydrogen atom. To treat a general atom we use an alternative basis called the *B-Spline* basis [6]. Instead of equation (3.18), we have

$$\Psi(\mathbf{r}, t) = \sum_{n,l,m} a_{n,l,m}(t) \frac{B_n(r)}{r} Y_{l,m}(\theta, \phi) \qquad (3.34)$$

where $B_n(r)$ are B-splines.

The first and most obvious difference between B-Splines and the Sturmians is that the B-Splines are calculated within a well-defined box or interval, $I = [a, b]$, rather than relying on a dilation parameter and the number of functions in the basis to define the range that Sturmian functions can accurately represent. The size of the box is an important attribute to consider, choosing a box too small will incur artificial reflections of ionised electrons on

the edge of the box. Choosing the box too large will unnecessarily impede the length of a calculation by increasing the the number of B-spline functions needed to represent the box sufficiently. So, much like the overarching problem with Sturmian functions, the use of B-splines also requires the user to choose the least number of functions to speed up the calculations without affecting the convergence of observables. Within the subject of laser physics, we may define the size of the box based on the ponderomotive energy (defined in Chapter 2) of the ionised electrons which, in turn, is defined by parameters of the laser.

A basis of B-spline functions is defined over an interval $I = [a, b]$. I is then divided into l subintervals by defining $l + 1$ *breakpoints* ξ_j in strict ascending order

$$a = \xi_1 < \xi_2 < ... < \xi_{l+1} = b. \qquad (3.35)$$

Associated with the interior breakpoints is a second set of non-negative integers ν_j, i.e. $j = 2, 3, ..., l$. These integers define the degree of continuity $C^{\nu_j - 1}$, the *continuity condition*, at the breakpoints in the interval. A continuity condition C^{-1} would define no continuity at the breakpoint. At the edges of the interval, $\xi_1 = a$ and $\xi_{l+1} = b$, we impose C^{-1}.

Finally we must define a sequence of *knots* $t_1 \leq t_2 \leq ... \leq t_m$ where $m \geq l+1$. Each B-spline is a piecewise polynomial function of degree, or *order*, k defined over the interval $[t_i, t_{i+k}]$. The *multiplicity* of the knot sequence is defined at each breakpoint. Given multiplicity $\mu_j = k - \nu_j$, we have μ_j knots at the breakpoint ξ_j. Thus, the knot sequence defines the continuity condition at each breakpoint. As stated beforehand, we require no continuity at the edges of the box, we are only interested in the region $[a, b]$ and so we impose $\mu_1 = k$ and $\mu_{l+1} = k$. In most cases, it is beneficial to produce maximal continuity,

C^{k-2}, at the interior breakpoints, and so for $j = 2, 3, ..., l$, the multiplicity at each breakpoint will be $\mu_j = 1$.

3.3.4 Computing a Basis of B-splines
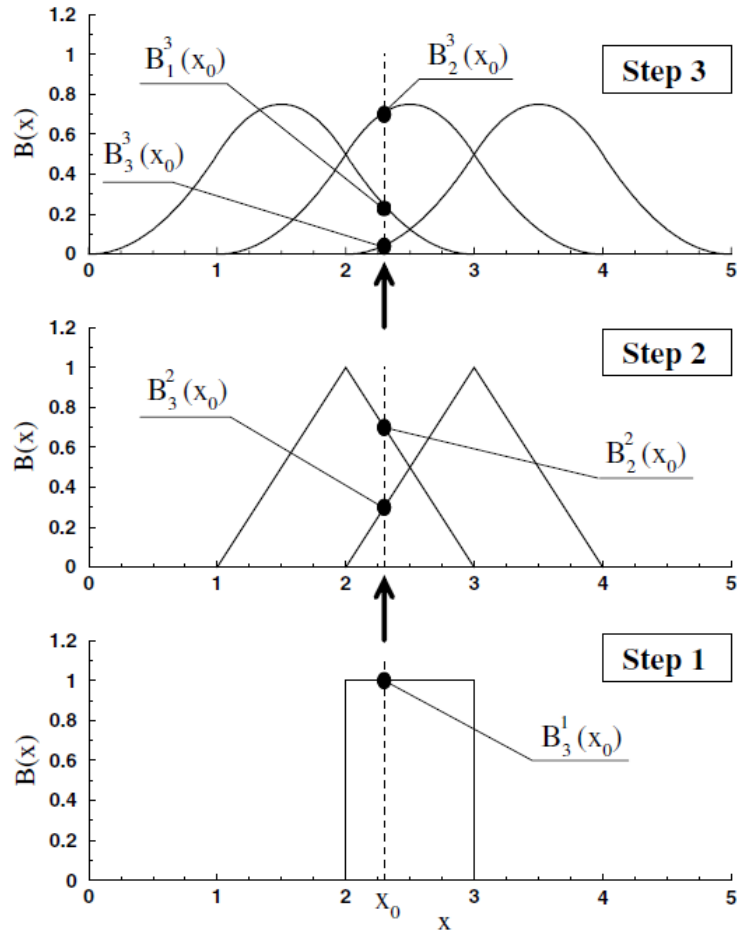
Figure 3.9: Recursive evaluation of B-splines up to order $k = 3$, relative to the knot sequence $\{0, 1, 2, 3, 4, 5\}$ [6].

Grid mesh points between breakpoints may be arbitrarily chosen because each B-spline in the basis is computed iteratively at a point x in the interval $[t_i, t_i + k]$. We may exploit the fact that B-splines are piecewise polynomial functions by selecting the mesh points to coincide with the abscissae of the Gaussian Quadrature, enabling extremely fast and exact integration.

Given the definition of a B-spline of order $k = 1$

$$B_i^1(x) = 1, \quad t_i \le x < t_{i+1} \quad \text{and} \quad B_i^1(x) = 0, \quad \text{otherwise,} \qquad (3.36)$$

we may recursively compute the value of $B_i^k(x)$ of arbitrary order k using the recurrence relation [27]

$$B_i^k(x) = \frac{x - t_i}{t_{i+k-1} - t_i} B_i^{k-1} + \frac{t_{i+k} - x}{t_{i+k} - t_{i+1}} B_{i+1}^{k-1}(x). \qquad (3.37)$$

Figure 3.9 displays graphically how equation (3.37) computes higher and higher orders of B-spline (up to order $k = 3$ in the example). The value of $B_3^1(x_0)$ in the lowest panel of figure 3.9 is defined using equation (3.36) with $t_3 = 2$ and $t_4 = 3$. Equation (3.37) is then used to produce the points shown in the middle panel of figure 3.9. The B-spline $B_3^1(x_0)$ appears in the recursive formulae for $B_2^2(x_0)$ and $B_3^2(x_0)$ and so the values of two separate B-splines are defined. The values $B_2^2(x_0)$ and $B_3^2(x_0)$ then produce the points shown in the topmost panel for third order B-splines. Note that the fully formed picture of the B-splines shown in figure 3.9 are built up by considering many points along the entire interval $[a, b] = [0, 5]$.

3.4 The Hydrogen Atom

We can compute the 'atomic' basis for the hydrogen atom by computing the eigenvalues and eigenvectors of the field free Hamiltonian within a box and to use them as a basis. We initially represent the full wave function as a linear combination of spherical harmonics and B-splines, in much the same way as the Sturmian representation

$$\Psi(\mathbf{r}) = \sum_{k,l,m} c_{k,l,m} \frac{B_k(r)}{r} Y_{l,m}(\theta, \phi). \tag{3.38}$$

The function $u_{n,l}(r)$ is the solution to the reduced radial equation:

$$\left(-\frac{1}{2}\frac{d^2}{dr^2} + \frac{l(l+1)}{2r^2} - \frac{1}{r} \right) u_{n,l}(r) = E_{n,l} u_{n,l}(r). \tag{3.39}$$

From equation (3.38) we have $u_{n,l}(r) = \sum_{k=1}^{N} a_i^{n,l} B_k(r)$ yielding the system

$$\mathbf{H}_0^l \cdot \mathbf{a} = E\mathbf{S} \cdot \mathbf{a} \tag{3.40}$$

where $\mathbf{a}$ contains the coefficients in equation (3.38).

The elements of the field free Hamiltonian and overlap matrices are

$$\begin{aligned}
[\mathbf{H}_0^l]_{i,j} = &-\frac{1}{2} \int_a^b B_i(r)\frac{d^2}{dr^2} B_j(r)dr \\
&+ \frac{l(l+1)}{2} \int_a^b \frac{B_i(r)B_j(r)}{r^2}dr - \int_a^b \frac{B_i(r)B_j(r)}{r}dr
\end{aligned} \tag{3.41}$$

and

$$[\mathbf{S}]_{i,j} = \int_a^b B_i(r)B_j(r)dr, \tag{3.42}$$

respectively. We can glean from the fact that $B_i^k(x)$ is non-zero in the interval $[t_i, t_i{+}k]$ that integrals involving B-splines are non-zero if and only if $|i{-}j| < k$. Hence, the Hamiltonian and the overlap matrix are both $2k-1$ banded.

Table 3.1 exhibits the eigenvalues computed by solving the generalised eigensystem in equation (3.40) using a basis of B-splines of order 9.

Table 3.2 highlights the accuracy of the B-spline basis when computing lower bound states for each orbital angular momentum. Choosing a finer mesh

close to the nucleus and a more sparse mesh at greater distances is conducive to higher accuracy when computing the bound states [78], [74].

```
l =          0
    -0.50000000E+00        -0.12500000E+00        -0.55555556E-01        -0.31250000E-01

l =          1
    -0.12500000E+00        -0.55555556E-01        -0.31250000E-01        -0.20000000E-01

l =          2
    -0.55555556E-01        -0.31250000E-01        -0.20000000E-01        -0.13888889E-01

l =          3
    -0.31250000E-01        -0.20000000E-01        -0.13888889E-01        -0.10204082E-01

l =          4
    -0.20000000E-01        -0.13888889E-01        -0.10204082E-01        -0.78125000E-02
```

Table 3.1: Eigenvalues computed by solving equation (3.40) using a basis 400 B-splines of order 9 in a box of size 400 a.u.

```
l =          0
    0.37956860E-11         0.83821838E-14         0.17725011E-14         0.13183898E-15

l =          1
    0.63837824E-14         0.43684200E-14         0.14002688E-13         0.68389779E-15

l =          2
    0.78232166E-14         0.25025121E-13         0.29101680E-15         0.42664558E-14

l =          3
    0.11865509E-14         0.19161339E-13         0.14326117E-13         0.10962532E-13

l =          4
    0.30271341E-13         0.25338142E-13         0.31345532E-13         0.11103098E-13
```

Table 3.2: Magnitude of the difference between the values of the true eigenvalues and those computed in figure 3.2.

3.5 The Argon Atom

For atoms with more complicated systems than that of hydrogen, where more than one electron exists, it is necessary to make approximations to reduce the complexity of the system. The approximation made is called the *Single Active Electron* (SAE) approximation. The premise behind the SAE approximation is simple: the laser field is assumed to only interact with one electron in the system. The approximation is effective when the probability of the other electrons within the system becoming excited or even ionised is negligible. The approximation is particularly well suited to the noble gases where the dominant

method of multiphoton ionisation is single electron sequential excitation [76].
For problems involving argon, to be shown in later chapters, this is an excellent
choice of approximation.

In order to model argon within the SAE, it is necessary to take care when
considering the ion-electron interactions close to the core. Muller [62] pro-
vides a broadly used pseudopotential that recovers the eigenenergies for the
bound states of argon through the solution of the following time independent
Schrödinger equation (TISE)

$$\left[-\frac{1}{2}\nabla^2 + V_0(r) + W_0(r) \right] \Psi(\mathbf{r}) = E\Psi(\mathbf{r}) \tag{3.43}$$

where $V_0(r)$ and $W_0(r)$ are given in [62] as

$$V_0(r) = -\frac{1 + Ae^{-Br} + (17 - A)e^{-Cr}}{r} \tag{3.44}$$

where the constants $A = 3.4$, $B = 1$ and $C = 3.682$ are chosen to reproduce
the configuration averages of the binding energies of the singly excited states
[60] and

$$W_0(r) = F\left[\left(\frac{R_x - R}{G}\right)^5 - \left(\frac{R_x - R}{G}\right)^4 \right] \tag{3.45}$$

where $F = 2.5$, $R_x = 3$, $R = 0.5$ and $G = 2.01785$. $V_0(r)$ also reproduces
the K-shell, L-shell and $3s$ ionisation potentials correctly as well as exhibiting
the correct asymptotic behaviour. Thus, $V_0(r)$ is an excellent approximation
to the electron-ion interaction excluding exchange, as long as core excitations
are absent, however, due to the deep potential well supporting inner shells, we
cannot use $V_0(r)$ as such.

To obtain a potential suitable for a simulation of argon in the single active
approximation, Muller [62] made use of the fact that the first radial node of the

p wave and the second node of the s wave nearly coincide. Muller imposes a hard-core boundary condition at $R = 0.5$ ($\Psi(\mathbf{r}) = 0$ for $0 < r < R$). This hard-core boundary only induces a small distortion of these waves and eliminates the K-shells and the L-shells. The d wave penetrates near this boundary and is sensitive to these small distortions. In order to deal with these defects, Muller includes a soft repulsive core $W_0(r)$. Beyond $R_x = 3$, the eigenfunctions in the well $W_0(r) + V_0(r)$ are identical to those in only $V_0(r)$ and together they yield the exact representation of the $3p$ energy.

One final thing to note is that only low angular momenta penetrate significantly below the R_x threshold. For all $l \geq 3$, the eigenfunctions remain purely hydrogenic. $V_0(r) + W(r)$ is known as the Muller effective potential for argon.

3.6 Time Propagation

3.6.1 Crank-Nicolson

The time dependent wave function is represented, for example, as a linear combination of B-spline functions and spherical harmonics

$$\Psi(\mathbf{r}) = \sum_{k,l,m} c_{k,l,m}(t) \frac{B_k(r)}{r} Y_{l,m}(\theta, \phi). \tag{3.46}$$

Substituting this form of the wave function into the time-dependent Schrödinger equation, we obtain a system of coupled differential equations

$$i\mathbf{S} \cdot \dot{\mathbf{c}}(t) = (H_0 + \mathbf{D}(t)) \cdot \mathbf{c}(t) \tag{3.47}$$

where $\mathbf{D}(t)$ contains the time-dependent part of the Hamiltonian and $\mathbf{S}$ is the block diagonal overlap matrix. We choose to keep the time interaction part

$\mathbf{D}(t)$ general in this section since we shall use a mix of dipole and non-dipole time dependent components in the Hamiltonian within this thesis.

Approximating $\dot{\mathbf{c}}(t)$ and $\mathbf{c}(t)$ with

$$\dot{\mathbf{c}}(t) = \frac{\mathbf{c}(t + \frac{\delta t}{2}) - \mathbf{c}(t - \frac{\delta t}{2})}{\partial t} \tag{3.48}$$

and

$$\mathbf{c}(t) = \frac{\mathbf{c}(t + \frac{\delta t}{2}) + \mathbf{c}(t - \frac{\delta t}{2})}{2} \tag{3.49}$$

we arrive at the implicit Crank-Nicolson propagation scheme correct to order δt^2:

$$\left(\mathbf{S} + \frac{i\delta t}{2}(H_0 + \mathbf{D}(t))\right) \cdot \mathbf{c}\left(t + \frac{\delta t}{2}\right) = \left(\mathbf{S} - \frac{i\delta t}{2}(H_0 + \mathbf{D}(t))\right) \cdot \mathbf{c}\left(t - \frac{\delta t}{2}\right). \tag{3.50}$$

3.6.2 Preconditioner

A preconditioner may be applied to the above system in order to simplify the original problem into something more manageable when using iterative methods. For example, one may require many passes through some iterative algorithm, but with a preconditioner, the number of passes should be significantly reduced depending on the complexity of the preconditioning applied.

For ease, allow $\mathbf{c}(t + \delta t) = \mathbf{x}$, $\mathbf{c}(t) = \mathbf{b}$ and

$$A = \mathbf{S} + \frac{i\delta t}{2}H_0, \tag{3.51}$$

the time-independent part of the system and let

$$B = -\frac{i\delta t}{2}\mathbf{D}(t). \tag{3.52}$$

We may recast equation (3.50) as

$$(A - B)\mathbf{x} = (\bar{A} + B)\mathbf{b}. \tag{3.53}$$

The objective of the preconditioner is to then approximate $(A - B)^{-1}$ and the one selected for the results shown later in this section is:

$$M = \left[\sum_{n=0}^{n_{order}} (A^{-1}B)^n \right] A^{-1} \tag{3.54}$$

where n_{order} is the order of the preconditioner. Then

$$M(A - B)\mathbf{x} = M(\bar{A} + B)\mathbf{b} \tag{3.55}$$

reduces to

$$\left(\mathbb{I} - (A^{-1}B)^{n_{order}+1} \right)\mathbf{x} = \left[\sum_{n=0}^{n_{order}} (A^{-1}B)^n \right] A^{-1}(\bar{A} + B)\mathbf{b}. \tag{3.56}$$

Finally, let both $\tilde{A} = \mathbb{I} - (A^{-1}B)^{n_{order}+1}$ and $\tilde{\mathbf{b}} = \left[\sum_{n=0}^{n_{order}} (A^{-1}B)^n \right] A^{-1}(\bar{A} + B)\mathbf{b}$ and we have the preconditioned system $\tilde{A}\mathbf{x} = \tilde{\mathbf{b}}$ ready to be solved for $\mathbf{x}$ using the Biconjugate Gradient Stabilised method (BiCGSTAB) routine.

We now move to describe the algorithm we chose to use for all the time propagation of the TDSE presented within this thesis. We found for the problems we consider, that the BiCGSTAB with preconditioning [82] provided efficient resolution of systems of equations of the form:

$$A\mathbf{x} = \mathbf{b} \tag{3.57}$$

where the vectors $\mathbf{x}, \mathbf{b} \in \mathbb{C}^n$ and A is an $n \times n$ matrix with elements $A_{ij} \in \mathbb{C}$ $\forall i, j \in \{1, 2, ..., n\}$. The time taken to invert the matrix A grows like $\mathcal{O}(n^3)$, and non-dipole terms fill the system A further and thus we look to iterative methods to approximate $\mathbf{x}$ without the need to directly invert the system.

In 1992, H. A. Van der Vorst developed the BiCGSTAB [82] as an improvement upon the numerically unstable Biconjugate Gradient method (BiCG) [32]. In order to describe the algorithm, it is necessary to cover some background material on the subject of Krylov subspaces.

3.6.3 Krylov Subspaces

The approximate solutions $\mathbf{x}_k$ to the system shown in equation (3.57) that Krylov subspace methods produce are

$$\mathbf{x}_k \in \mathbf{x}_0 + \mathcal{K}_k(\mathbf{r}_0, A), \qquad k = 1, 2, ... \tag{3.58}$$

where k is the dimension of the Krylov subspace, $\mathbf{x}_0$ is the initial candidate for the solution to the system and $\mathbf{r}_0 = \mathbf{b} - A\mathbf{x}_0$, the initial residue. The Krylov subspace is defined as follows:

$$\mathcal{K}_k(\mathbf{r}_0, A) = \{\phi(A)\mathbf{r}_0 | \phi \in \mathcal{P}_{k-1}\} \tag{3.59}$$

with

$$\mathcal{P}_n = \{\phi(\lambda) \equiv \sigma_0 + \sigma_1 \lambda + ... + \sigma_n \lambda^n | \sigma_0, \sigma_1, ..., \sigma_n \in \mathcal{C}^n\}. \tag{3.60}$$

That is, the Krylov subspace $\mathcal{K}_k(\mathbf{r}_0, A) = \text{span}\{\mathbf{r}_0, A\mathbf{r}_0, ..., A^{k-1}\mathbf{r}_0\}$. Note that

we may express the residual vector $\mathbf{r}_k$ corresponding to the kth iteration of the solution $\mathbf{x}_k$ in terms of a polynomial $P_k(A)$:

$$\mathbf{r}_k = \mathbf{b} - A\mathbf{x}_k = P_k(A)\mathbf{r}_k \qquad (3.61)$$

where

$$P_k \in \mathcal{P}_k, \quad P_k(0) = 1. \qquad (3.62)$$

The idea is to choose a polynomial P_k at each step to minimise the norm of the residual vector $\mathbf{r}_k$.

3.6.4 BiCGSTAB

The BiCGSTAB algorithm improves upon the erratic convergence of $\mathbf{r}_k = P_k(A)\mathbf{r}_0$ to zero by introducing a second polynomial Q_k to act upon the residues like so:

$$\mathbf{r}_k = Q_k(A)P_k(A)\mathbf{r}_0 \qquad (3.63)$$

with

$$Q_k(A) = (\mathbb{I} - \omega_1 A)(\mathbb{I} - \omega_2 A) \cdots (\mathbb{I} - \omega_k A). \qquad (3.64)$$

The choice of ω_i being crucial to minimising the norm of the residue at the kth iteration. We are now ready to introduce the BiCGSTAB algorithm:

Initialisation.

1. Choose $\gamma > 0$ to select the precision of the iterative procedure;

2. Choose an initial candidate solution $\mathbf{x}_0$ to the system;

3. Calculate $\mathbf{r}_0 = \mathbf{b} - A\mathbf{x}_0$;

4. Choose arbitrary vector $\hat{\mathbf{r}}_0$ such that $(\hat{\mathbf{r}}_0, \mathbf{r}_0) \neq 0$;

5. $\rho_0 = \alpha = \omega_0 = 1$;

6. $\mathbf{p}_0 = \mathbf{v}_0 = \mathbf{0}$.

Iterative procedure.

do $i = 1, 2, ...$

- $\rho_i = (\hat{\mathbf{r}}_0, \mathbf{r}_{i-1})$;

- $\beta = \frac{\rho_i \alpha}{\rho_{i-1}\omega_{i-1}}$;

- $\mathbf{p}_i = \mathbf{r}_{i-1} + \beta(\mathbf{p}_{i-1} - \omega_{i-1}\mathbf{v}_{i-1})$;

- $\mathbf{v}_i = A\mathbf{p}_i$;

- $\alpha = \frac{\rho_i}{(\hat{\mathbf{r}}_0, \mathbf{v}_i)}$;

- $\mathbf{s} = \mathbf{r}_{i-1} - \alpha\mathbf{v}_i$;

- $\mathbf{t} = A\mathbf{s}$;

- $\omega_i = \frac{(\mathbf{t},\mathbf{s})}{(\mathbf{t},\mathbf{t})}$;

- $\mathbf{x}_i = \mathbf{x}_i + \alpha\mathbf{p}_i + \omega_i\mathbf{s}$;

- if $||\mathbf{r}|| < \gamma$ then quit the procedure and take $\mathbf{x}_i$ to be the solution to the system;

- else $\mathbf{r}_i = \mathbf{s} - \omega_i\mathbf{t}$

end do

Note that to reduce the number of iterations through the BiCGSTAB routine, we initially set the order of the preconditioner to 1 but allow the order to vary from time step to time step. The order of the preconditioner is increased by one in time step $n+1$ if the BiCGSTAB routine is used more than once in time step n and reduced by one if the BiCGSTAB routine is not used all. This can occur when the preconditioning is enough to produce $\mathbf{r}_0$ in the initialisation part of the BiCGSTAB algorithm small enough to not warrant the iterative procedure which would normally follow. Varying the order of preconditioner allows us to use larger time steps and results in a moderate increase in the speed of computation for large calculations.

<center>Chapter 4</center>

<center>*The Propensity Rule*</center>

4.1 Introduction

If the frequency of the external laser field is varying slowly we can calculate the ionisation rate from the static field ionisation rate. In this so called adiabatic limit (which corresponds to the Keldysh parameter $\gamma \ll 1$) for circularly polarised radiation, the ionisation rate is equal to the static field value since the electric field is constant in magnitude while rotating. C. Z. Bisgaard and L. B. Madsen [15] derived formulae for the ionisation rates for static and slowly varying fields for hydrogen. Using the asymptotic form of the wave function of hydrogen within a Coulomb field, they showed that the ionisation rate for a static field from any initial state (n, l, m) of hydrogen to be

$$\omega_{ion} = \frac{|B|^2}{2^{|m|}|m|!} \frac{1}{\kappa^{\frac{2}{\kappa}-1}} \left(\frac{2\kappa^3}{E_0}\right)^{\frac{2}{\kappa}-|m|-1} e^{-\frac{2\kappa^3}{3E_0}}, \qquad (4.1)$$

where

$$B^2 = D^2 \frac{2l+1}{2} \frac{(l+|m|)!}{(l-|m|)!} \qquad (4.2)$$

and D is a normalisation constant coming from the asymptotic form of the radial Coulomb wave function for hydrogen which only depends on n and l but not m. The parameter $\kappa = \sqrt{2I_p}$, where I_p is the binding energy and E_0 is the amplitude of the electric field. This formula and its low frequency limit

<center>76</center>

can be generalised to other atoms such as argon in the single active electron approximation using effective values for n and l and is called the ADK formula after its creators. It is clear from this formula that the ionisation rate is therefore independent of the sign of m in the initial state. The dependence is only on $|m|$ in the adiabatic limit [15]. The question then arises - what if γ increases and the adiabatic assumption breaks down, is there is a propensity to ionise depending on the sign of m? In other words will a circularly polarised field deplete bound states that co-rotate with respect to the field more so than the bound states counter-rotating with the field? Initial studies by Gadja and Piraux in 1994 [35] partially addressed this question, where the two authors considered the initial $2p$ hydrogen state under the effect of a circularly polarised sine square pulse, while varying both the laser intensity and the initial azimuthal quantum number between $m = -1, m = 0$ and $m = 1$. In this case, the binding energy of $2p$ hydrogen is $I_p = 0.125$ a.u. and the frequency of the pulse was $\omega = 0.25$ a.u. They were able to provide numerical evidence of the *propensity rule* which states that as the electric field increases in strength, electrons rotating counter ($2p$ $m = -1$) to the field were ionised at a greater rate than those rotating with the field ($2p$ $m = 1$).

Barth and Smirnova, in a series of papers, examined the question as to whether there exists a propensity rule in general [10]. They produced an analytic semi-classical theory to describe the ionisation rate for electrons with initial states counter-rotating and co-rotating within a circularly polarised field in the non-adiabatic regime $\gamma \approx 1$ and in fact for any γ. They derived formulae, for short range potentials, that state there is a propensity to ionise from an initial state counter-rotating with the field. There is tentative experimental evidence to back up Barth and Smirnova's conclusion by Herath *et al* [40], however the experiment is very difficult to perform cleanly. Furthermore, first

order Coulomb corrections to Barth and Smirnova's theory for long range fields, given by Kaushal and Smirnova in [51], lessened the degree to which counter-rotating electrons ionised preferentially over co-rotating ones.

Recently Bauer *et al* [13] performed *ab initio* calculations and found that for certain conditions in hydrogen, the propensity rule does not hold. When moving from the multiphoton regime to the over the barrier ionisation (OBI) regime, the co-rotating electrons ionised more readily, contradicting the analytical theory by Barth, Smirnova and Kaushal ([10],[9] and [51]).

In this chapter we set out to explore the range of validity of the semi-classical theory of Barth and Smirnova based on of the theory of Perelomov, Popov and Terentev (PPT) [65] by performing a direct numerical integration of the TDSE with the inclusion of the full Coulomb potential. We consider the ionisation of the $3p$ of argon from initial states $m = 1$ and $m = -1$ for a range of frequencies and intensities in a 6 cycle pulse. The work by Barth and Smirnova assumed a continuous sinusoidal field, whilst we use a finite pulse but the measured quantities should otherwise be directly comparable.

Since the papers outlined so far in this introduction, Barth and Lein numerically solved the TDSE in 2 dimensions for neon subject to a circularly polarised electric field [8]. The ionisation probabilities from initial states $2p_-$ and $2p_+$ neon exhibited the same propensity rule predicted in Barth's earlier work with Smirnova in [9] and [10].

In addition to this, Lui and Barth investigated this propensity rule in nitric oxide subject to a circularly polarised electric field [56]. They argue that the ionisation rate from co-rotating and counter-rotating electrons, with respect to the electric field, should be the same as in the atomic picture. Furthermore, they state the propensity rule for ionisation rates is the same as the atomic case considered in [9] and [10] for any system with at least cylindrical symmetry.

By solving the TDSE within the single active electron approximation using a grid based Crank-Nicolson method, the pair provide ionisation ratios of the ionisation probabilities for nitric oxide subject to a 3 cycle circularly polarised electric field. Figure 2 in [56] shows good agreement between the analytical theory in [9] and [10] and the ionisation ratio of initial state co-rotating and counter-rotating nitric oxide after the numerical solution of the TDSE.

Kaushal and Smirnova have published three companion papers in August 2018 ([48], [49], [50]) that follow on from their 2013 paper [51] which first introduced long range Coulomb corrections to the ionisation rates based on PPT theory given by Barth and Smirnova in [9] and [10]. All three papers focus on non-adiabatic effects in the tunnelling regime using the analytic R-matrix method to include the effect of the core. The first paper [48] has a focus on the interplay of the two momentum kicks associated with the Coulomb potential. The first momentum shift is the addition momentum accrued by the laser field during the additional time interval the Coulomb correction gives to the ionisation time and the second is due to the electron-core interaction under the barrier [48].

The first paper goes further than [51] by the ionisation for higher (l, m) pairs. Specifically, the pair study the ionisation rates for p, d and f orbitals for $|m| \leq 1, 2$ and 3, respectively. The ionisation rate is shown to not only be dependent on the direction of rotation of the initial state with respect to the field. It becomes clear that as l increases, the nature of the orbital structure defines the ionisation rate, too. Initial states associated with orbitals that have no contribution in the plane of the circularly polarised electric field become the least likely candidates for ionisation, while initial states with orbitals that have large contributions to the plane of polarisation are ionised much more readily (see figure 1 and 2 of [48]). The ionisation ratios from initial states with oppo-

site signs of m for different atoms are calculated, each with a separate focus on p-, d- and f-orbitals. Unlike the previous work published, the ionisation ratio decreases slowly and smoothly with increasing electric field strength and fixed wavelength. The counter-rotating electrons still always remain more likely to be ionised than their co-rotating cousins [48].

The second of the three papers derive the quantum orbits and classical trajectories within the ionisation process using the ARM method, however, Kaushal and Smirnova provide an approximate ionisation ratio for ionisation yields of counter- to co-rotating electrons for $\gamma \ll 1$ with the Coulomb correction [49]. This approximate ratio agrees relatively well with the full ARM calculation, with a discrepancy of at most 8% for $|m| = 3$ in Ytterbium III.

The third and final paper in the series is concerned with spin polarisation in the non-adiabatic tunnelling regime, but also provides an approximate formula for the ionisation rate from a specific (l, m) pair. One of the dependencies on the initial state comes from orbital-specific Coulomb correction which is given as a prefactor [50]. Table 1 in [48] provides this prefactor up to and including the f-orbital.

4.2 Derivation of the Ionisation Rate in the PPT Theory of Barth and Smirnova

The adiabatic picture assumes that the barrier seen by the electron is 'static' in the sense that the electron does not feel the oscillations of the low frequency field when tunnelling. This assumption can be made because the tunnelling is said to happen 'faster' than the oscillations of the field. Experimentally however, the Keldysh parameter of a pulse is typically seen to fall in the region $\gamma \approx 1$, corresponding to the non-adiabatic regime. This regime assumes

the barrier is no longer static 'during' the time the electron tunnels and so the field's time dependence upon the barrier plays a role [10].

Within the non-adiabatic tunnelling regime for short range potentials, the ratio of ionisation from $3p_+$ and $3p_-$ ($m = 1$ and $m = -1$ for right circularly polarised light, respectively) argon orbitals has been answered analytically by Barth and Smirnova [10], [9] using the PPT theory [65], [66] in circularly polarised light.

The advantage of using PPT theory over the more widely used SFA is that PPT theory is gauge invariant whilst the SFA is certainly not. For short range potentials, the SFA will also predict the same ionisation rates for p_+ and p_- orbitals [12]. We know already there is clear numerical evidence from Gajda and Piraux [35] discussed above and also experimental results by Herath *et al* [40] in direct contradiction to what the SFA would predict.

Below we sketch the derivation of Barth and Smirnova to give a flavour of the complex analytic calculations involved at arriving at the final result for the ionisation rate, but we refer the reader to the original papers for the detailed derivation.

The fields defined in the literature by Barth and Smirnova are

$$\mathbf{E}_\pm = E_0[\cos(\omega t)\hat{\mathbf{e}}_x \pm \sin(\omega t)\hat{\mathbf{e}}_y] \tag{4.3}$$

and

$$\mathbf{A}_\pm = -A_0[\sin(\omega t)\hat{\mathbf{e}}_x \mp \cos(\omega t)\hat{\mathbf{e}}_y], \tag{4.4}$$

where $+$ and $-$ refer to right and left circularly polarised light, respectively and $A_0 = E_0/\omega$. We shall restrict our equations to right circularly polarised light.

4.2. DERIVATION OF THE IONISATION RATE IN THE PPT THEORY OF BARTH AND SMIRNOVA

They assume the electron ionisation is described by the TDSE in the SAE approximation and dipole approximation

$$i\frac{\partial}{\partial t}\Psi(\mathbf{r},t) = \left[-\frac{1}{2}\nabla^2 + V(\mathbf{r}) + \mathbf{r}\cdot\mathbf{E}(t) \right]\Psi(\mathbf{r},t) \qquad (4.5)$$

where $V(\mathbf{r})$ is the effective, short range potential.

The exact solution to equation (4.5) can be represented using the time dependent Green's function of the electron for motion in a circularly polarised field with $V(\mathbf{r}) = 0$:

$$G(\mathbf{r},t,\mathbf{r}',t_i) = \frac{\theta(t-t_i)}{(2\pi)^3}\int d\mathbf{k}e^{i\mathbf{v}(t)\cdot\mathbf{r}-i\mathbf{v}(t_i)\cdot\mathbf{r}'}e^{-\frac{i}{2}\int_{t_i}^t \mathbf{v}(\tau)^2 d\tau} \qquad (4.6)$$

where

$$\mathbf{v}(t) = \mathbf{k} + \mathbf{A}(t) \qquad (4.7)$$

is the instantaneous electron velocity and $\mathbf{k}$ is the final momentum at the detector [9]. The solutions to equation (4.5) with $V(\mathbf{r}) = 0$ are the Volkov states. The exact solution with the inclusion of a short range potential $V(\mathbf{r})$ is then the following

$$\begin{aligned}\Psi(\mathbf{r},t) = \int d\mathbf{r}'G(\mathbf{r},t,\mathbf{r}',t_0)\Psi(\mathbf{r}',t_0)- \\ i\int_{t_0}^t dt_i \int d\mathbf{r}'G(\mathbf{r},t,\mathbf{r}',t_i)V(\mathbf{r}')\Psi(\mathbf{r}',t_i).\end{aligned} \qquad (4.8)$$

This first term on the right hand side of equation (4.8) spreads out with respect to time and so does not contribute to the flux and falls off proportional to $1/\sqrt{t}$. So, at infinity, this term does not affect the ionisation rate.

We assume we can neglect the difference between the bound orbital for the

free atom $\varphi_{l,m}(\mathbf{r'})e^{iI_p t_i}$ and the wave function $\Psi(\mathbf{r'}, t_i)$ for short range potentials [65]. The same assumption cannot be made for the Coulomb potentials, but corrections can be applied (see [51]). Thus, using the field free TDSE, Barth and Smirnova replace the term $V(\mathbf{r'})\Psi(\mathbf{r'}, t_i)$ by

$$V(\mathbf{r'})\varphi_{l,m}(\mathbf{r'})e^{iI_p t_i} = \frac{1}{2}(\nabla_{\mathbf{r'}}^2 - 2I_p)\varphi_{l,m}(\mathbf{r'})e^{iI_p t_i}. \tag{4.9}$$

Barth and Smirnova assume the field is turned on at time $t_0 \to -\infty$ adiabatically and rewrite equation (4.5) as

$$\Psi(\mathbf{r}, t) = \frac{i}{(2\pi)^{\frac{3}{2}}} \int_{-\infty}^{t} dt_i e^{iI_p t_i} \int d\mathbf{k} e^{i\mathbf{v}(t)\cdot\mathbf{r}} e^{-\frac{i}{2}\int_{t_i}^{t} \mathbf{v}^2(\tau)d\tau} \phi_{l,m}(\mathbf{v}(t_i)) \tag{4.10}$$

where

$$\phi_{l,m}(\mathbf{v}(t)) = \frac{1}{2}[\mathbf{v}^2(t) + 2I_p]\tilde{\varphi}_{l,m}(\mathbf{v}(t)) \tag{4.11}$$

and

$$\tilde{\varphi}_{l,m}(\mathbf{k}) = \frac{1}{(2\pi)^{\frac{3}{2}}} \int d\mathbf{r} e^{-i\mathbf{k}\cdot\mathbf{r}} \varphi_{l,m}(\mathbf{r}) \tag{4.12}$$

is the momentum space representation of the wave function. By converting to cylindrical coordinates, (k_ρ, θ, k_z), the exponential factors of equation (4.10) shown in equations (4.4) and (4.7) are represented as

$$i\mathbf{v}(t) \cdot \mathbf{r} = if(k_\rho, \theta, \phi, t)\rho + ik_z z, \tag{4.13}$$

and

$$-\frac{i}{2}\int_{t_i}^{t}\mathbf{v}(\tau)^2 d\tau = -\frac{i}{2}(k^2 + A_0)^2(t - t_i) - i\mathbf{k}\cdot[\boldsymbol{\xi}(t) - \boldsymbol{\xi}(t_i)], \qquad (4.14)$$

where

$$f(k_\rho, \theta, \phi, t) = k_\rho\cos(\theta - \phi) - A_0\sin(\omega t - \phi) \qquad (4.15)$$

and

$$\boldsymbol{\xi}(t) = \mathbf{E}(t)/\omega^2. \qquad (4.16)$$

Now we sketch the derivation of the time averaged ionisation rate from the solution of equation (4.10). The time averaged ionisation rate is equal to the time averaged radial flux at the infinity $\rho \to \infty$

$$\omega(E_0, \omega) = \lim_{\rho\to\infty}\overline{J(\rho, t)}. \qquad (4.17)$$

Equation (4.17) is calculated by evaluating the integral

$$J(\rho, t) = \rho\int_{-\infty}^{\infty}dz\int_{0}^{2\pi}d\phi j_\rho(\rho, \phi, z, t), \qquad (4.18)$$

where

$$j_\rho(\mathbf{r}, t) = \frac{i}{2}\left(\Psi(\mathbf{r}, t)\frac{\partial}{\partial\rho}\Psi^*(\mathbf{r}, t) - \Psi^*(\mathbf{r}, t)\frac{\partial}{\partial\rho}\Psi(\mathbf{r}, t)\right). \qquad (4.19)$$

is the radial component of the current of the wave function.

From this point onward, we shall outline the important steps leading to the main result given in [9] by making frequent references to equations within the paper by Barth and Smirnova.

4.2. DERIVATION OF THE IONISATION RATE IN THE PPT THEORY OF BARTH AND SMIRNOVA

To deal with the z-component of the integral in equation (4.18), Barth and Smirnova represent equation (4.19) as a product of integrals over $\mathbf{k}$ involving the temporally periodic function

$$F(\mathbf{k}, t) = \phi_{l,m}(\mathbf{v}(t))e^{i\mathbf{k}\cdot\boldsymbol{\xi}(t)}. \tag{4.20}$$

This function is then expanded into the Fourier series

$$F(\mathbf{k}, t) = \sum_{n=-\infty}^{\infty} F_n(\mathbf{k}, \omega)e^{-in\omega t} \tag{4.21}$$

with coefficients

$$F_n(\mathbf{k}, \omega) = \frac{1}{2\pi} \int_{-\pi}^{\pi} d(\omega t)F_\pm(\mathbf{k}, t)e^{in\omega t}. \tag{4.22}$$

Note that the quantity

$$|F_{n\pm}(\mathbf{k}, \omega)|_{k=k_n}^2 \tag{4.23}$$

is the general formula for the probability of the n-photon process at $k = k_n$.

Equation (4.17) is simplified by using equations (22) and (24) in [9] and the integration over z takes place. The integration over ϕ is handled in appendix A of [9]. The limit of the radial flux at infinity is given by equation (29) in [9]. The residue method is then applied and equation (32) in [9] yields the radial flux at infinity as a summation from $n = n_0$ to ∞, where n_0 is the minimum number of photons required for ionisation.

By time averaging over one laser cycle, Barth and Smirnova use equation (32) in [9] in equation (4.17) to represent the final formula for the ionisation rate as a summation over multiphoton channels:

$$\omega(E_0, \omega) = \sum_{n \geq n_0}^{\infty} \omega_n(E_0, \omega), \qquad (4.24)$$

where

$$\omega_n(E_0, \omega) = 2\pi \int d\mathbf{k}\delta\left(\frac{k^2}{2} - \frac{k_n^2}{2}\right)|F_n(\mathbf{k}, \omega)|^2. \qquad (4.25)$$

In order to evaluate equation (4.25), the saddle point method is employed to calculate the quantity given in equation (4.23). The first instance of the dependence of the ionisation rate on the sign m for circular pulses is given in equations (73) and (74) in [9] in the factor $|e^{im\phi_v(t_i)}|^2_{k=k_n}$ within the evaluated expression for equation (4.23). The function $\phi_v(t_i)$ is the tunnelling momentum angle and is complex for $m \neq 0$ which results in $|e^{im\phi_v(t_i)}|^2_{k=k_n} \neq 1$.

The full formulae for the ionisation rates for s, p_0 and $p_\pm$ orbitals are given in equations (76 - 78) in [9]. These formulae are very complicated and still require integration over k_z to evaluate in full. These equations are simplified further by approximating the integrands by Taylor series in k_z up to second order yielding equations (88 - 90) in [9] where equation (90) describes the ionisation rate for $p_\pm$ orbitals.

Equations (88 - 90) in [9] are expressed as summations over $n-$photon processes where $n \geq n_0$. To achieve a simple formula for the ionisation rate, the summation over n is replaced with an integration over the variable

$$\zeta = \frac{2n_0}{n} - 1 \in (-1, 1]. \qquad (4.26)$$

For $\omega \ll I_p$, the saddle point method is applied to the integration over ζ, where $\zeta = \zeta_0$ is the unique maximum of the exponent in equations (88-90) in [9] and the resulting final formula for $l = 1$ initial states, the crowning

achievement of Barth and Smirnova, becomes:

$$\omega^{p\pm}(E_0,\omega) = |C_{\kappa 1}|^2 I_p \frac{E_0}{2(2I_p)^{\frac{3}{2}}} h^{p\pm}(\gamma) e^{-\frac{2(2I_p)^{\frac{3}{2}}}{3E_0} g(\gamma)} \qquad (4.27)$$

where

$$g(\gamma) = \frac{3\zeta_0}{\gamma^2(1-\zeta_0^2)} \sqrt{(1+\gamma^2)(\zeta_0^2/\gamma^2+1)} \qquad (4.28)$$

does not depend on orbitals and where

$$h^{p\pm}(\gamma) = h^s(\gamma) \frac{3(1+\gamma^2)}{2(1-\zeta_0^2)} \left(\sqrt{\frac{\zeta_0^2/\gamma^2+1}{1+\gamma^2}} - \frac{\zeta_0}{\gamma}\mathrm{sgn}(m) \right)^2 \qquad (4.29)$$

with $h^s(\gamma)$ dependent on γ and ζ_0

$$h^s(\gamma) = (1-\zeta_0)\sqrt{\frac{(1+\gamma^2)(1-\zeta_0^2)}{(1+\zeta_0^2/\gamma^2)(1+\zeta_0^2+2\zeta_0^2/\gamma^2)}}. \qquad (4.30)$$

For a given γ, ζ_0 is a solution to the transcendental equation

$$\mathrm{arctanh}\left(\sqrt{\frac{\zeta_0^2+\gamma^2}{1+\gamma^2}} \right) = \frac{1}{1-\zeta_0} \sqrt{\frac{\zeta_0^2+\gamma^2}{1+\gamma^2}}. \qquad (4.31)$$

The constant $|C_{\kappa,1}|^2$ in equation (4.27) comes from the normalisation constant

of the wave function in coordinate space asymptotically far away from the core

which is in general of the form

$$\varphi_{l,m} = C_{\kappa,l}\kappa^{\frac{3}{2}} \frac{e^{-\kappa r}}{\kappa r} Y_{l,m}(\theta,\phi). \qquad (4.32)$$

The dependence of the ionisation rate on the sign of m is clearly displayed

in the factor $h^{p\pm}(\gamma)$ in equation (4.27). Note, that $g(\gamma) \approx 1-\gamma^2/15$ for $\gamma \ll 1$

and so in the adiabatic limit $\gamma \to 0$, the exponential in equation (4.27) reduces

to the exponential for the ionisation rate found within ADK theory [15] with

its hydrogenic form given in equation (4.1).

Finally, the simplified asymptotic ratios of the ionisation rates for counter-and co-rotating rates for right circularly polarised light are

$$\frac{\omega^{p-}(E_0, \omega)}{\omega^{p+}(E_0, \omega)} \approx 1 + \frac{4\gamma}{3} + \frac{8\gamma^2}{9} > 1 \qquad (\gamma \ll 1), \qquad (4.33)$$

$$\frac{\omega^{p-}(E_0, \omega)}{\omega^{p+}(E_0, \omega)} \approx (2 \log \gamma)^2 > 1 \qquad (\gamma \gg 1). \qquad (4.34)$$

Hence, the probability for a counter-rotating electron to ionise is always larger than the probability to ionise from a co-rotating electron with respect to the field within PPT theory.

4.3 The Propensity Rule in the Over the Barrier Ionisation Regime

An initial attempt was made by Bauer *et al* [13] to examine the range of validity of Barth and Smirnova's theory. They considered the three initial 2p states of hydrogen, namely, $m = -1, 0, 1$. However, because of the low ionisation potential for the hydrogen 2p states, Bauer *et al* were only able to explore a limited region of the parameter space, in particular the over the barrier regime.

Nevertheless, they found that for certain circular field parameters, the propensity to ionise from initial state counter-rotating electrons as opposed to initial state co-rotating electrons can flip when considering the multiphoton and over the barrier or barrier suppression ionisation regime (BSI).

By solving the TDSE directly using a basis of Sturmian functions, Bauer *et al* were able to identify that for a fixed wavelength of 800 nm, an increase in field intensity produced a flip in the propensity rule. Specifically, this inver-

sion of the rule was found at intensities below $10^{13} W/cm^2$ where the counter

rotating electron was in fact less likely to ionise than its co-rotating cousin.

There was also clear evidence of a large degree of excitation occurring before

the strong-field ionisation, indicating that one must include these excited sta-

tes in the theoretical description of the process if one is to understand the

process from a theoretical standpoint - something that Barth and Smirnova

did not include in their calculations when employing PPT theory to study the

propensity rule.

Bauer *et al* acknowledge that their numerical calculations are not a direct

comparison with the work done by Barth and Smirnova [9]. In order to directly

compare with Barth and Smirnova it is necessary to produce a numerical study

of the non-adiabatic regime where $\gamma \approx 1$ and $E \leq E_{BSI}$, where E_{BSI} is the

point at which the total combined potential of the Coulomb potential and the

laser lies below the binding energy of the electron ([77], [4], [31]). The threshold

for the electric field strength at which the BSI regime becomes dominant is at

$$E_{BSI} = \frac{I_p^2}{4Z}. \tag{4.35}$$

The non-adiabatic regime is able to be specified by its lower and upper

limits, $I_{min} = 4\omega^2 I_p^2$ where $\gamma = 1$ and $I_{max} = I_{BSI} = 2E_{BSI}^2$ (peak intensity is

two times the electric field amplitude squared in the case of circularly polarised

light). So, if $I_{max} < I_{min}$ then no non-adiabatic tunnelling ionisation occurs.

With fixed frequency and variable intensity, in this case it is possible to go

directly from the multiphoton regime to the BSI [5]. For the binding energy

of $2p$ hydrogen, one would need a pulse with frequency $\omega < \omega_{lim} = 0.0078 a.u.$

A frequency this low would prove very tricky to model faithfully with current

computational power.

Hence to explore the validity of Barth and Smirnova's theory we need to work with a different atom, namely a noble gas, and we choose to work with argon.

4.4 Argon in Circularly Polarised Light

The binding energy of the $3p$ ground state of argon (0.5821 a.u.) in the single electron approximation is much larger than that of $2p$ hydrogen (0.125 a.u.) discussed in the previous section. The main drawback in using hydrogen to model interactions in the non-adiabatic tunnelling regime was that the frequency of the laser driving the interaction had be $\omega \leq 0.0078a.u.$ [13]. This would lead to a huge number of (l, m) pairs to be required in a calculation for convergence and extremely large radial box sizes to quell significant reflections. Argon's $3p$ state increases the frequency limit to $\omega \leq 0.0785166a.u.$ such that $I_{min} \leq I_{max}$. This fact alone makes the non-adiabatic tunnelling regime much more accessible with current computational power. It is important to note that on top of the requirement we place on the frequency of the pulse, it is also necessary that the field's electric amplitude falls below the BSI regime limit. For the case of $3p$ argon, this limit is $I_{BSI} \leq 5.03722 \times 10^{14}W/cm^2$. With all of this mind, we shall focus our efforts in this section to exploring the ionisation probability and rate of co- and counter-rotating electrons of ground state argon subject to laser pulses where parameters fall around $\gamma \approx 1$. In the case of circularly polarised light, the Keldysh parameter is defined as such

$$\gamma = \frac{\omega \sqrt{2I_p}}{\sqrt{\frac{I}{2}}} \tag{4.36}$$

since the peak intensity $I = 2E_0^2$, due to the fact $I = 2 < \mathbf{E}^2 >$ alongside the

definition of the electric field in equation 4.3.

4.4.1 TDSE Calculations for Argon

We investigate ground state argon subject to the circularly polarised vector potential given by equation (3.33). A right circularly polarised pulse propagating along the z-axis implies that $3p$, $m = 1$ co-rotates with the laser and that $3p$, $m = -1$ rotates against the laser. Thus, we shall denote the two ground states of argon as $3p_+$ and $3p_-$, respectively.

We used the Muller Potential described in Chapter 3 (see equations (3.43) to (3.45)) to represent the electron's motion in argon and we expanded the wave function in a basis of B-splines and spherical harmonics including all allowed values of m. We used the Crank-Nicolson method to integrate the resultant coupled time dependent equations together with the bi-conjugate gradient method also described in Chapter 3 (see equation (3.50)). For the following calculations, the time step remained fixed at $\delta t = 0.1$ a.u. for all frequencies. The minimum angular momentum number also remains fixed at $l_{min} = 0$ throughout all calculations presented in this chapter, since the selection rules for $3p_-$ and $3p_+$ are the same. The maximum angular momentum number does vary depending on the frequency: for $\omega = 0.0569$ we have $l_{max} = 80$; $\omega = 0.06$ and $\omega = 0.07$ required $l_{max} = 60$; $\omega = 0.08$ required $l_{max} = 56$; $\omega = 0.09$ required $l_{max} = 48$ and all remaining frequencies used $l_{max} = 40$. The size of the box for each frequency also varied, the case of $\omega = 0.0569$ used the largest box at $r_{max} = 1100$ a.u.; $\omega = 0.06$ and $\omega = 0.07$ required $r_{max} = 1000$ for convergence; $\omega = 0.08, 0.09$ and 0.1 required $r_{max} = 800, 700$ and 500, respectively; $\omega = 0.11$ and 0.12 used a box size of $r_{max} = 400$; $\omega = 0.13 - 0.17$ were calculated using a box of size $r_{max} = 250$ and all remaining frequencies used a box size of $r_{max} = 200$ for convergence.

The following calculations were performed over 6 cycles for a fixed peak intensity of $I = 2.64541 \times 10^{14} W/cm^2$. This intensity has been chosen specifically so that $\gamma = 1$ when the wavelength of the pulse is 800 nm, the lowest frequency we consider in these tests. As we increase the frequency of the pulse, the Keldysh parameter strictly increases.

We look at three predictions of Barth and Smirnova theory, namely the ionisation probability versus frequency, the ionisation probability versus intensity and the ionisation yield versus energy. They present calculations for krypton, which has a very similar ionisation potential to argon at 0.5 a.u. Their formulae only depend on the field strength, the frequency and the ionisation potential.

4.4.2 Ionisation Probabilities Versus Frequency

Figure 4.1 shows their results. They clearly show that the ionisation rate is larger for the counter-rotating electron and it increases monotonically with frequency.

Figure 4.2 displays our calculations for the ionisation probability after a 6 cycle right circularly polarised pulse has been switched off for varying frequencies, ranging from $\omega = 0.0569 - 0.3$ a.u. To compute the ionisation probability after the pulse, we first calculate the eigenvalues and eigenfunctions of the atomic Hamiltonian $\mathcal{H}_0$ in the B-spline basis and convert the wave function to the atomic basis as follows:

$$\mathbf{a}_{l,m}(\tau) = \left(\mathbf{E}_l^{\text{B-spline}}\right)^T \mathbf{S} \mathbf{c}_{l,m}(\tau). \tag{4.37}$$

In equation (4.37) we have denoted the overlap matrix of the B-spline functions as $\mathbf{S}$, the matrix of eigenvectors for the B-spline atomic Hamiltonian for
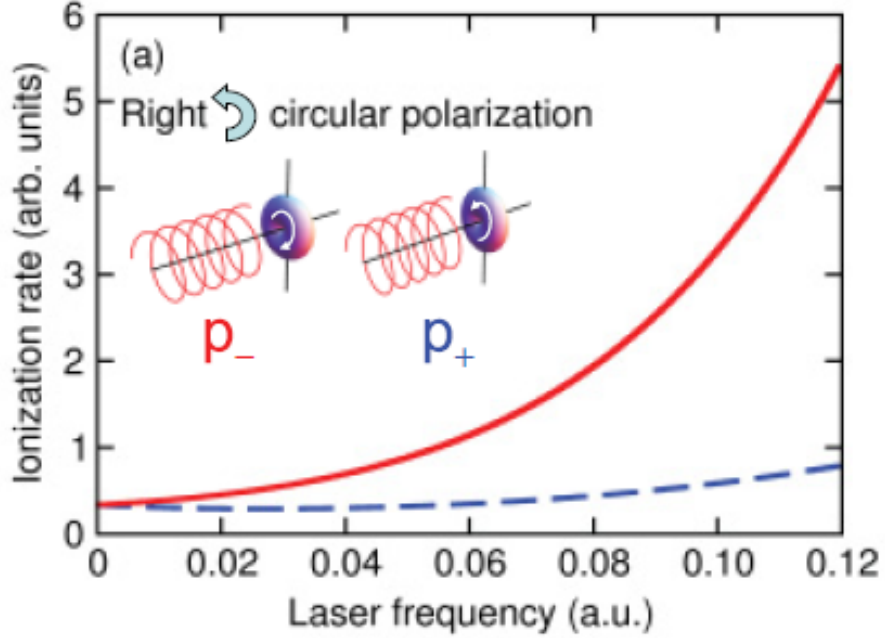
Figure 4.1: Ionisation rate versus frequency for counter and co-rotating ground state $4p$ krypton subject to right circularly polarised light with $E_0 = 0.06$ a.u. (peak intensity $I = 2.52648 \times 10^{14} W/cm^2$) computed using equations (4.27) - (4.31) with $C_{\kappa,l} = 1$ in equation (4.32) [10].

Figure 4.2: Ionisation probability versus frequency for the $3p$, $m = 1$ and $3p$, $m = -1$ initial states of argon subject to a right circularly polarised pulse over 6 cycles for fixed peak intensity $I = 2.64541 \times 10^{14} W/cm^2$ calculated by propagating the TDSE directly with Crank-Nicolson.
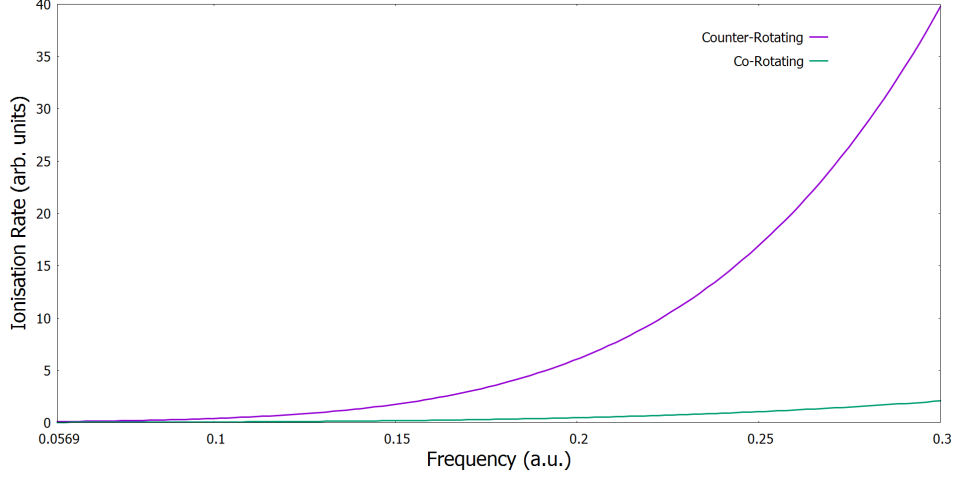
Figure 4.3: Ionisation rate versus frequency for counter and co-rotating ground state $3p$ argon subject to right circularly polarised light with peak intensity $I = 2.64541 \times 10^{14} W/cm^2$ computed using equations (4.27) - (4.31) with $C_{\kappa,l} = 1$ in equation (4.32).

a given l as $\mathbf{E}_l^{\text{B-spline}}$ and the vectors of coefficients for a specific (l, m) pair of the wave function at the end of the pulse as $\mathbf{c}_{l,m}(\tau)$ and $\mathbf{a}_{l,m}(\tau)$ in the B-spline and atomic basis, respectively. Note that $\mathbf{E}_l^{\text{B-spline}}$ has as its columns the eigenvectors of $\mathcal{H}_0$. At this stage we sum the magnitude squared of the coefficients (denoted by $a_{n,l,m}(\tau)$) of each l, m pair of $\mathbf{a}_{l,m}$ over the total number of bound states and subtract the total from 1 to achieve the ionisation probability:

$$P_{\text{ion}} = 1 - \sum_{l,m} \sum_{n=1}^{n_{\text{bound}}} |a_{n,l,m}(\tau)|^2. \qquad (4.38)$$

We can clearly see evidence that the propensity rule holds true up until $\omega = 0.19$ a.u., at which point the ionisation probability for the counter-rotating electron briefly becomes lower than its co-rotating counterpart before peaking at $\omega = 0.24$ a.u. Around $\omega = 0.265$ a.u. the propensity rule flips again and we even see evidence that ionisation from $3p_+$ begins to increase significantly more than from $3p_-$.

Figure 4.4 presents the ratio of the ionisation probability from $3p_-$ over

$3p_+$ ground state argon. Interestingly, this ratio increases up to approximately 4 until $\gamma = 2$ and then drops precipitously to $\omega_+^{p-}(E_0, \omega)/ \omega_+^{p+}(E_0, \omega) \approx 1$ for $0.19 < \omega < 0.2$ a.u. There is a second peak in the ratio at $\omega = 0.24$, followed by a second steep fall in the ratio, such that $\omega_+^{p-}(E_0, \omega)/\omega_+^{p+}(E_0, \omega) \approx 0.5$ for the final few frequencies we consider.
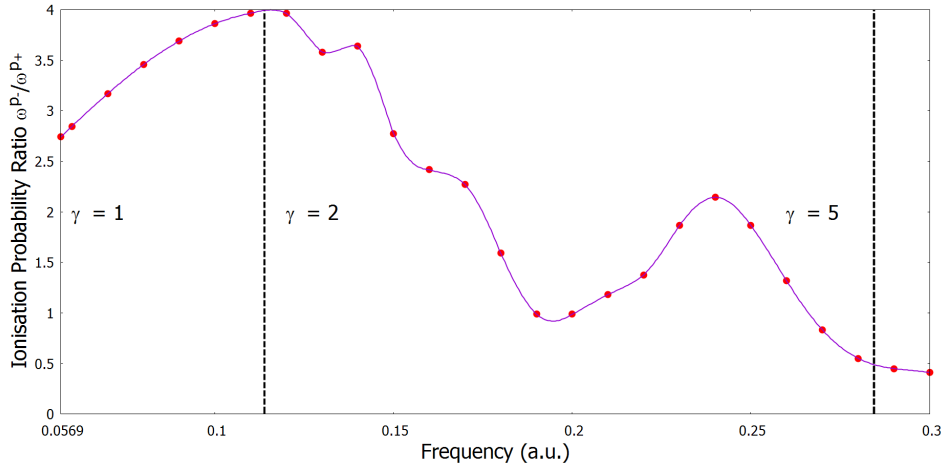
Figure 4.4: The ratio of the probability to ionise from $3p_-$ over $3p_+$ ground state argon versus frequency when subject to a right circularly polarised pulse over 6 cycles for fixed peak intensity $I = 2.64541 \times 10^{14} W/cm^2$ computed by directly propagating the TDSE with the Crank-Nicolson method.

Barth and Smirnova use PPT theory to paint a different picture as to what should occur with a short-range potential (see figure 4.1). They found that the ground state krypton counter-rotating electron ($I_p = 0.5$ a.u.), $4p_-$, was ionised at far greater rate relative to $4p_+$ ground state krypton than we see when directly solving the TDSE for argon, which has a similar ground state binding potential of $I_p = 0.5821$ a.u.. PPT theory [10] seemingly predicts the ratio to continue to rise, whereas our findings suggest that the opposite is true as ω and in turn, γ, increase past a certain threshold.

In order to achieve a more direct comparison with the ionisation rate predicted by PPT theory in [10], we used equations (4.27) - (4.31) to calculate the behaviour of $3p$ argon in right circularly polarised light shown in figure 4.3 using

the same peak intensity as figure 4.2. To calculate the ionisation rates for $3p$ argon, the parameters in equations (4.27) - (4.31) were $I_p = 0.5821$ a.u., $C_{\kappa,l} = 1$, $E_0 = 0.06139$ a.u. (corresponding to peak intensity $I = 2.64541 \times 10^{14} W/cm^2$) and the quantity ζ_0 in equation (4.31) was solved with Newton-Raphson. We restricted the frequency range to the same range as shown in figure 4.2 (0.0569 - 0.3 a.u.) and it is clear the formulae given in [10] breakdown in the multiphoton regime considerably. The ionisation rate of the counter-rotating electron becomes larger by a factor of approximately 19 at $\omega = 0.3$ a.u., however, relatively good agreement with numerical results is found within the non-adiabatic tunnelling regime $\gamma \approx 1$.

A shortfall of solving the TDSE directly using numerical methods is that we are comparing an ionisation probability in figure 4.2 to an ionisation rate in figures 4.1 and 4.3. Figure 4.5 displays the ionisation probabilities of $3p$ argon for the same parameters as in figure 4.2 except for the number of cycles has been reduced from 6 to 4. The results in figure 4.5 corroborate the fact that the propensity does indeed breakdown after a certain value of γ. Shortening the length of the pulse only changed the relationship between the counter-rotating and co-rotating ionisation probabilities to a small degree about $\omega \approx 0.2$. About this point, the ionisation probability of the counter-rotating electron dips below that of the co-rotating electron in figure 4.2 but does not do the same in figure 4.5. Aside from that fact, there is no appreciable difference between the two calculations.

Our findings do have more in common with the prediction given in [51] whereby first order long-range Coulomb corrections are added to PPT theory using analytical R-matrix theory to re-evaluate the propensity. The addition of a long-range correction has a significant effect on the ratio $\omega_+^{p-}/\omega_+^{p+}$, showing a dampening of the ratio from a peak of over 7 using PPT alone to just under

4. The ratio begins to decrease after about 6eV ($\omega \approx 0.22$ a.u.), a feature seen in argon in figure 4.4 after $\omega = 0.12$ a.u. It is worth noting the binding energy ($I_p = 0.79248$ a.u.) for the neon atom considered in figure 4.6 is higher than that of ground state argon.
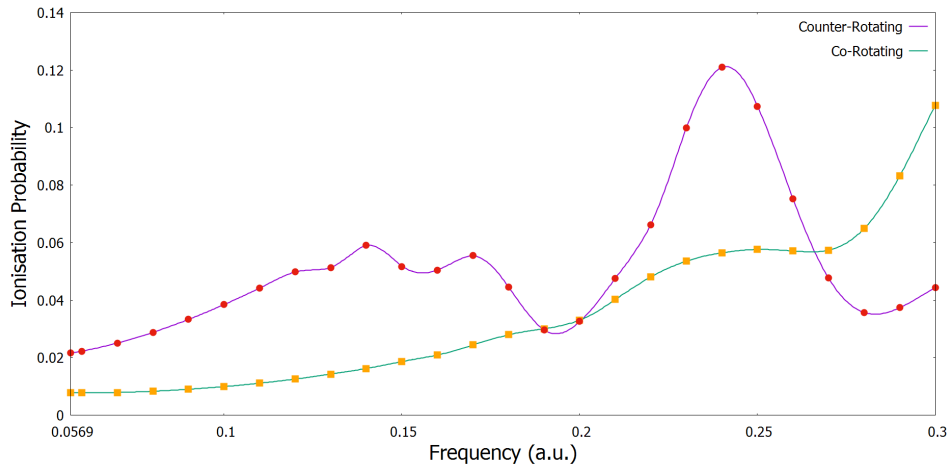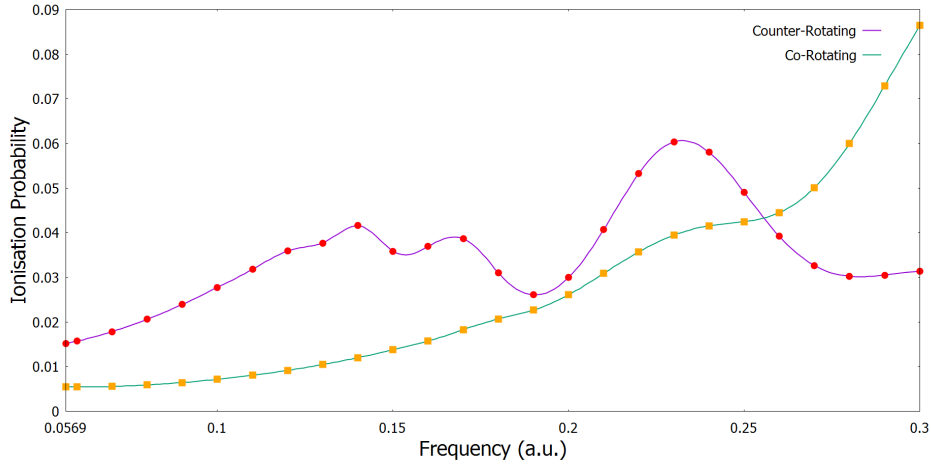

Figure 4.5: Ionisation probability versus frequency for the $3p$, $m = 1$ and $3p$, $m = -1$ initial states of argon subject to a right circularly polarised pulse over 4 cycles for fixed peak intensity $I = 2.64541 \times 10^{14} W/cm^2$ calculated by propagating the TDSE directly with Crank-Nicolson.
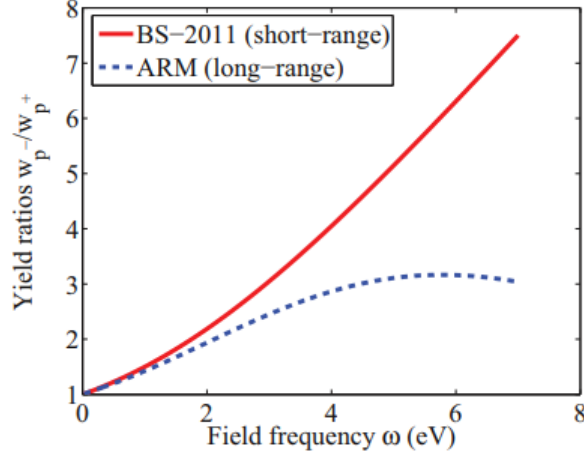
Figure 4.6: Ionisation rate ratio from p_- and p_+ orbitals versus frequency for a neon atom subject to a right circularly polarised pulse with intesity $I = 1.6 \times 10^{15} W/cm^2$. The red, solid line was produced using the PPT theory and short range potential shown in [10] and the blue, dashed line is the outcome of employing the analytical R-matrix (ARM) method [51].

4.4.3 Ionisation Probability Versus Intensity

Barth and Smirnova then look at the ionisation rate versus intensity and found similar behaviour to that of ionisation rate versus frequency in displayed figure 4.7 that is presented in log-log scale [10]. It is clear that as the intensity increases from $0.2 - 2 \times 10^{14} W/cm^2$, the counter-rotating electron is preferentially ionised over the co-rotating electron.
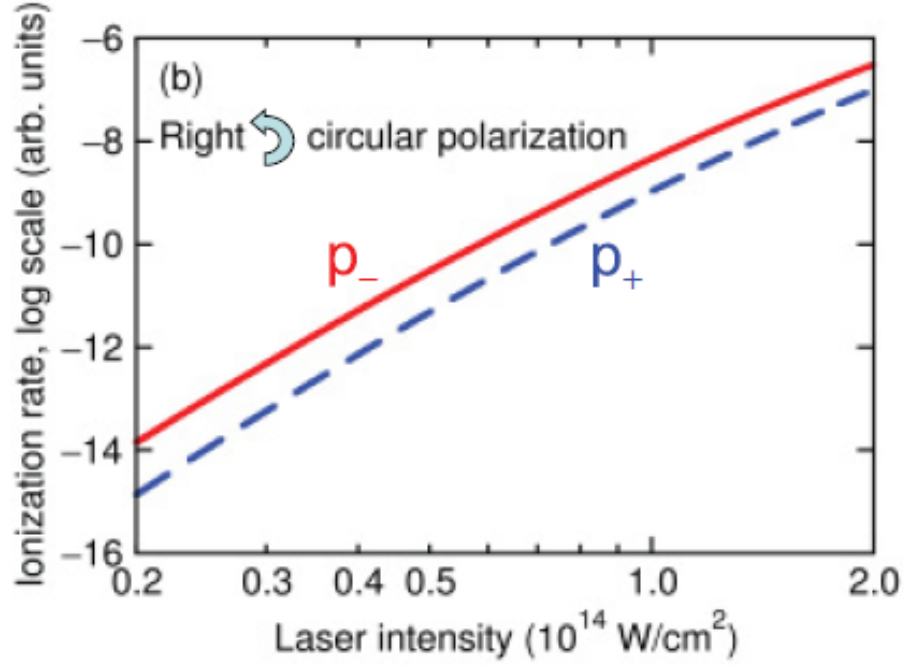
Figure 4.7: Ionisation rate versus intensity (W/cm^2) for counter and co-rotating ground state $4p$ krypton for 800 nm right circularly polarised light [10]. Note that these results do not include a Coulomb correction and are only results of equation (4.27).
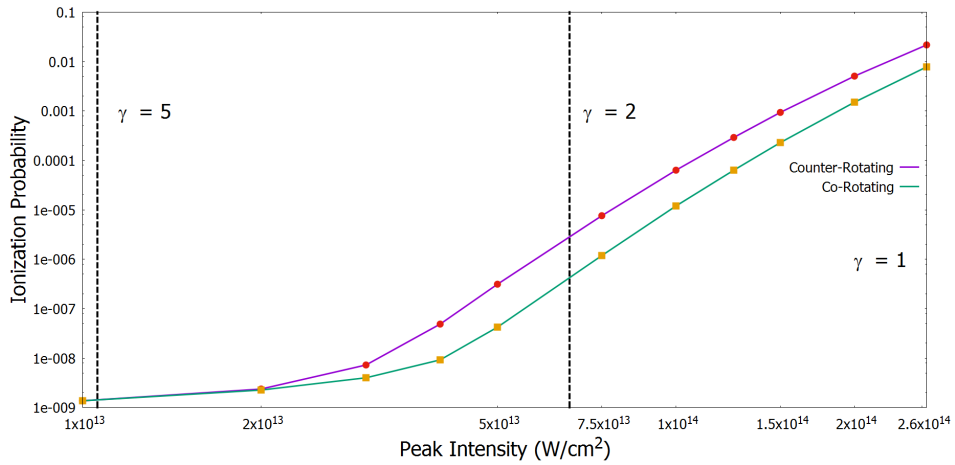
Figure 4.8: Ionisation probability versus peak intensity (W/cm^2) of ground state $3p$ argon for counter and co-rotating electrons subject to 6 cycle, right circularly polarised light with wavelength 800 nm computed by propagating the TDSE with the Crank-Nicolson method.

We see the same phenomena when directly solving the TDSE. There is a substantial increase in the probability to ionise from a counter-rotating initial state for the majority of the plot. There are points at which the counter-rotating electron is ten times more likely to ionise over the co-rotating electron. At $2 \times 10^{13} W/cm^2$, however, the ionisation probability between the two initial states becomes equal. At this stage, we are in the multiphoton ionisation regime and Barth and Smirnova's theory does not appear to agree with our results.

4.4.4 Ionisation Yield Versus Energy

We show in figure 4.9 the yield versus energy as calculated by Barth and Smirnova [10]. We have calculated the ionisation yield by calculating the probability of ionising with energy E_i by projecting the wave function onto the field free continuum states of energy E_i (denoted as $\psi_{E_i}(\mathbf{r})$)

$$\frac{dP}{dE}(E_i) = |\langle \psi_{E_i}(\mathbf{r})|\Psi(\mathbf{r},\tau)\rangle|^2. \tag{4.39}$$

We approximate the continuum using discrete states and carry out the projection in the atomic basis

$$\frac{dP}{dE}(E_i) = \frac{dP}{dE}\left(\frac{E_{i-1} + E_i + E_{i+1} + E_{i+2}}{4}\right) \tag{4.40}$$

$$= \frac{|\langle \psi_{E_i}(\mathbf{r})|\Psi(\mathbf{r},\tau)\rangle|^2}{E_{i+1} - E_{i-1}} + \frac{|\langle \psi_{E_{i+1}}(\mathbf{r})|\Psi(\mathbf{r},\tau)\rangle|^2}{E_{i+2} - E_i} \tag{4.41}$$

which simplifies to

$$\frac{dP}{dE}\left(\frac{E_{i-1} + E_i + E_{i+1} + E_{i+2}}{4}\right) = \sum_{l,m} \frac{|a_{E_i,l,m}(\tau)|^2}{E_{i+1} - E_{i-1}} + \frac{|a_{E_{i+1},l,m}(\tau)|^2}{E_{i+2} - E_i} \tag{4.42}$$

where $a_{E_i,l,m}(\tau)$ represent atomic wave function coefficients corresponding to the continuum state with energy $E_i > 0$. This procedure assures that the $\psi_{E_i}(\mathbf{r})$ are correctly energy normalised.

We shall cover a second method to produce the ionisation yield involving projection onto ingoing Coulomb wave functions in subsection 5.3.3.

The spectra displayed in figure 4.10 exhibits one similarity and one difference with the predictions given by Barth and Smirnova [10]. We find that the peaks of the spectra exist at a point larger than U_p, in agreement with figure 4.9 [10]. The argument for this shift in the peaks of the spectra is due to the fact that the initial velocity of tunnelled electrons is non-zero and contributes in a significant way to the energy spectra. In the adiabatic limit, the initial velocity after ionisation is zero and so the peak kinetic energy occurs at precisely U_p for a circularly polarised pulse.

PPT predicts the point at which there is an equal number of electrons ionised from p_+ and p_- occurs at final kinetic energy $E^0_{kin} = I_p + U_p$. This corresponds to the point at which there is no transverse momentum in either co- or counter-rotating orbital. Clearly, this is not the case when directly solving the TDSE. We find the point at which an equal number of electrons are ionised occurs at an energy lower than E^0_{kin}.

4.4.5 Excitation and Ground State Probabilities

One quality of laser-atom interactions that PPT theory does not account for is the probability to excite, but not ionise, the initial state. Bauer *et al* [13] performed a number of calculations with $2p$ hydrogen subject to an 800 nm 10 cycle, right circularly polarised laser field with varying intensities. With these parameters, hydrogen enters the BSI regime from the multiphoton regime at $I = 1.1 \times 10^{12} W/cm^2$. Significant excitation occurs in the multiphoton regime
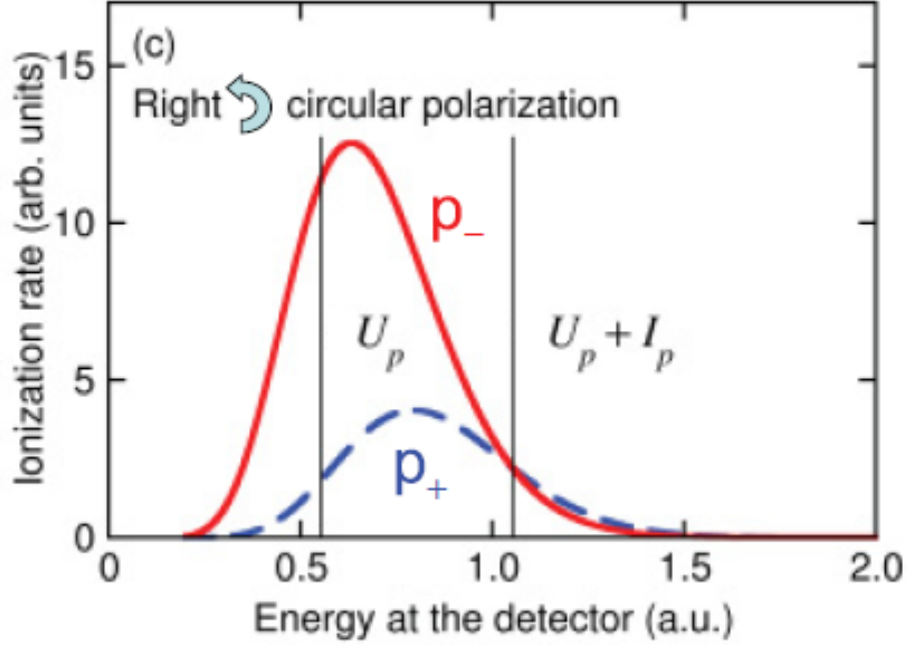
Figure 4.9: Photoelectron energy distribution at the detector for counter and co-rotating ground state $4p$ krypton subject to 800 nm right circularly polarised light with $E_0 = 0.06$ a.u. ($I = 2.52648 \times 10^{14} W/cm^2$) produced using equation 19 in [10].
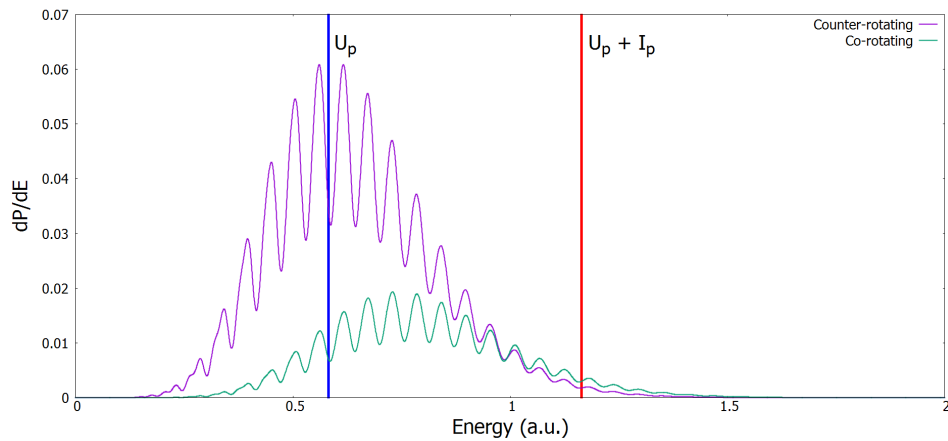
Figure 4.10: Energy spectra for photoelectrons emitted after ground state argon was subject to a right circularly polarised 800 nm 6 cycle laser pulse with peak intensity $I = 2.64541 \times 10^{14} W/cm^2$. Note that the peak in the spectra for circularly polarised light should occurs at $E = U_p$, but there is an error in the definition of U_p in [10]. The results shown here are comparable with figure 4.9 when this error is accounted for.

for $2p_+$ $(2p, m = 1)$, however it peaks at almost exactly the point at which over the barrier ionisation should become the dominant mechanism for ionisation at $1.1 \times 10^{12} W/cm^2$. By directly solving the TDSE for hydrogen, the degree of excitation was available to Bauer *et al* [13]. The counter-rotating electronic state $2p_-$ has consistently lower excitation probability relative to $2p_+$ (see the red line in figures 4.11 and 4.12) up until $I = 6 \times 10^{13} W/cm^2$ where they both seem to settle at the same excitation probability of around 0.2, even as intensity increases to up to $2 \times 10^{15} W/cm^2$. Surprisingly, there is significant excitation at these intensities which can be justified by assuming these excitations happen near the end of the pulse where the intensity is diminished.

A calculation involving $2p$ hydrogen in the non-adiabatic regime is unrealistic with current computational memory constraints, but $3p$ argon allows us to explore the excitation probability in the non-adiabatic regime quite comfortably. We calculate the probability to remain in the initial state by taking the magnitude squared of the coefficient in the atomic basis representation of the initial state

$$P_{\text{initial}} = |a_{n,l,m}^{\text{initial}}(\tau)|^2 \tag{4.43}$$

and we calculate the total excitation by

$$P_{\text{exci}} = 1 - P_{\text{ion}} - P_{\text{initial}} \tag{4.44}$$

where P_{ion} is described in equation (4.38). Our results for excitation probability versus frequency are displayed in figure 4.13.

At $\gamma \approx 1$, there are insignificant levels of excitation for both counter- and co-rotating electrons. In fact the probability for excitation remains almost zero until $\omega = 0.12$ a.u. which corresponds to $\gamma \approx 1.4$ for both counter and co-rotating electrons. As frequency increases, however, a large disparity
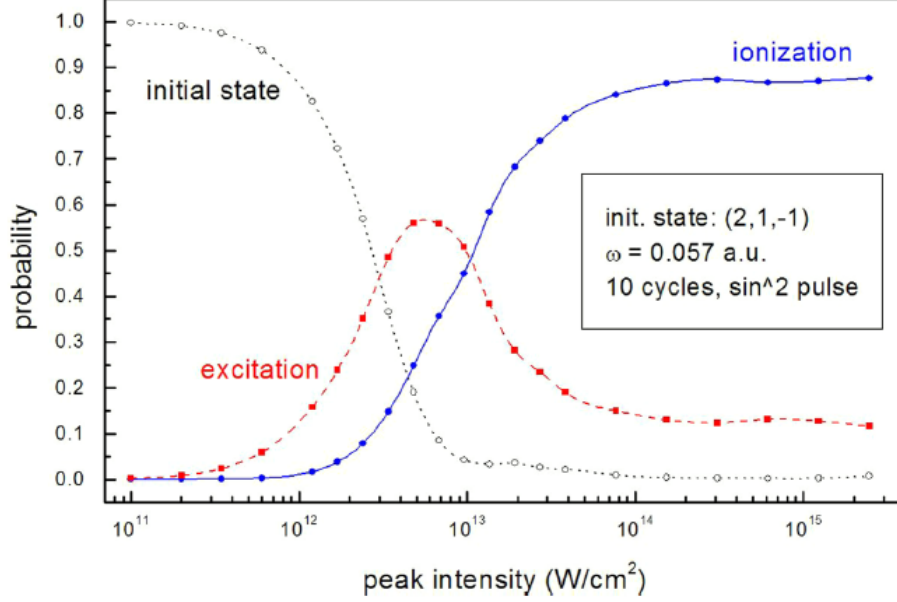
Figure 4.11: Probability of ionisation (blue solid lines with solid circles), excitation (red dashed lines with solid squares) and ground state probability (black dotted line with open circles) obtained by numerically propagating the TDSE for $2p_-$ hydrogen subject to a 10 cycle 800 nm right circularly polarised pulse [13].

between the excitation probability in counter and co-rotating initial state argon emerges. This suggests that multiphoton transitions become manifest at an earlier γ for the counter-rotating ground state electron. This pattern continues as ω increases and we clearly see the excitation probability remains much larger for $3p_-$ than $3p_+$. Significant excitation only begins to occur at $\omega = 0.26$ for the co-rotating electron, which corresponds to $\gamma \approx 4.57$ and starts to exhibit the same oscillatory behaviour of the excitation probability that the counter-rotating electron undergoes.

The most striking feature of the plot shown in figure 4.13 is the oscillatory behaviour of the excitation probability for the counter-rotating electron as the frequency varies. These peaks occur at $\omega = 0.16$ ($\gamma = 2.812$), $\omega = 0.193$ ($\gamma = 3.392$) and $\omega = 0.24$ ($\gamma = 4.218$). The position of these peaks match
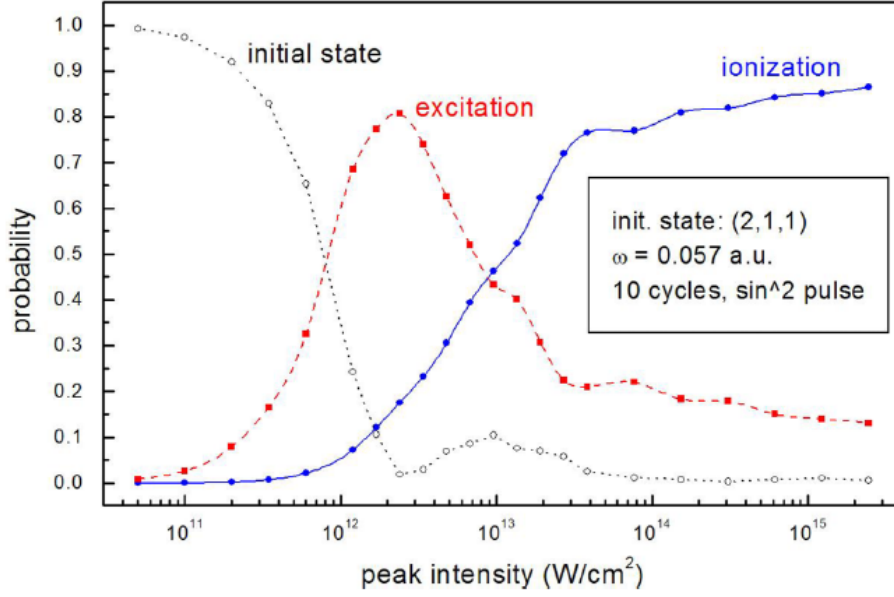
Figure 4.12: Probability of ionisation (blue solid lines with solid circles), excitation (red dashed lines with solid squares) and ground state probability (black dotted line with open circles) obtained by numerically propagating the TDSE for $2p_+$ hydrogen subject to a 10 cycle 800 nm right circularly polarised pulse [13].
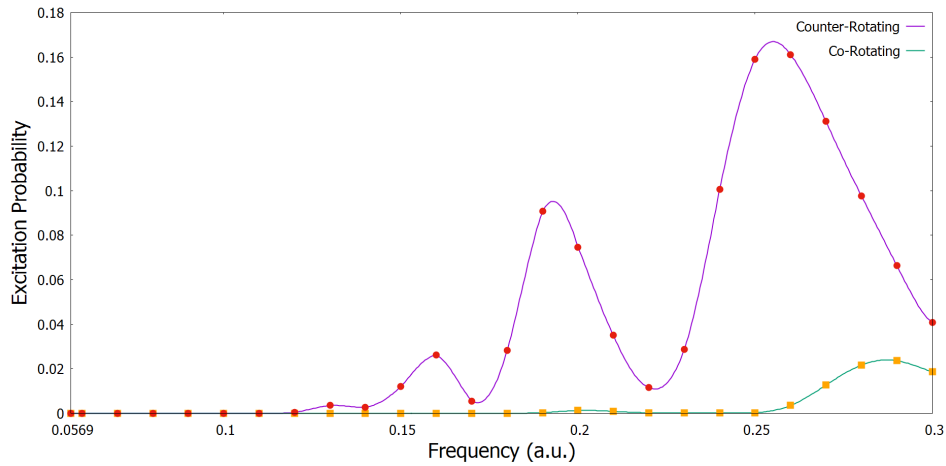
Figure 4.13: Excitation probability versus frequency for $3p_-$ and $3p_+$ ground state argon subject to a right circularly polarised 800 nm, 6 cycle pulse with fixed peak intensity $I = 2.6451 \times 10^{14} W/cm^2$ computed by propagating the TDSE with the Crank-Nicolson method.

the position of the troughs for the counter-rotating electron's probability to remain in the initial state if we look to figure 4.14.

If we compare the position of the peaks in excitation for $3p_-$ argon to the ionisation probability in figure 4.2, we see that there is a dip in ionisation probability for $\omega = 0.16$ and $\omega = 0.193$. In order to investigate this feature, we calculate the individual populations of the excited states at the end of the pulse at the frequencies where these peaks occur i.e. $|a_{n,l,m}(\tau)|^2$ where $a_{n,l,m}(\tau)$ is the coefficient of atomic state (n, l, m) in the atomic basis.

For $\omega = 0.16$, the majority of the excited states are f, $m = 3$ states which correspond to 4 photon absorptions from $3p_-$ after Stark shifting is taken into account. None of the excited states comprised more than 1% of the total wave function when taken individually. In order to ionise from $3p_-$ at $\omega = 0.16$, 5 photon absorptions are required. The case of $\omega = 0.193$ is similar in that we see 3 photon absorptions excite a broad set of d, $m = 2$ states and again, none comprised over 1% of the total wave function. 4 photon transitions are required for ionisation.

The final peak at $\omega = 0.24$ is different in that there is a coincident peak in the ionisation probability in figure 4.2. Upon analysing the wave function, the only significant excitation occurs in the $4p$, $m = 1$ state which requires 2 photon transitions to reach from initial state $3p$ argon. Interestingly, all 3 cases only excite the highest m state possible for a particular l. The $4p$, $m = 1$ state accounts for approximately 10% of the total wave function, which is virtually all of the excitation probability. The fact that only one state has been excited and there is a coincident peak in ionisation suggests a resonance occurs for this frequency between $4p$, $m = 1$ and the continuum. Figure 4.15 displays the rise in the population of the $4p$, $m = 1$ state as frequency increase from $\omega = 0.23 - 0.3$.
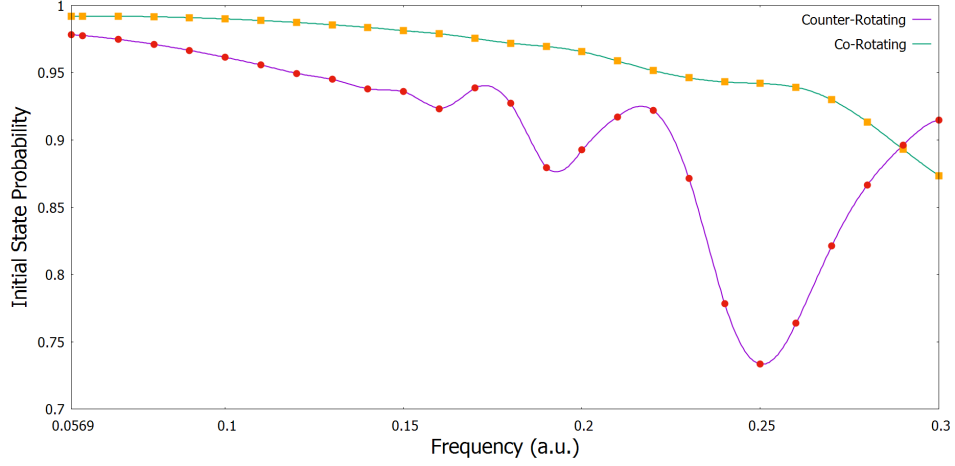
Figure 4.14: Initial state probabilty for $3p_-$ and $3p_+$ ground state argon versus frequency when subject to a right circularly polarised 800 nm, 6 cycle pulse with fixed peak intensity $I = 2.6451 \times 10^{14} W/cm^2$ computed by propagating the TDSE with the Crank-Nicolson method along with equation (4.43).
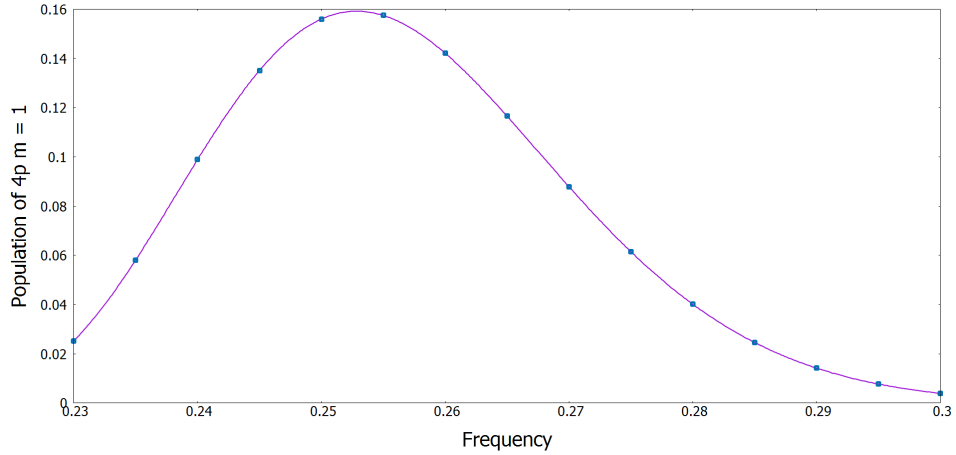
Figure 4.15: Excitation probability to state $4p$, $m = 1$ from $3p_-$ ground state argon versus frequency when subject to a right circularly polarised 800 nm, 6 cycle pulse with fixed peak intensity $I = 2.6451 \times 10^{14} W/cm^2$. This figure was computed by evaluating $|a_{4,1,1}(\tau)|^2$, the coefficient of $4p$, $m = 1$ in the atomic representation of the wave function at the end of the pulse.

4.5 Conclusion

From figures 4.2 and 4.4 it is clear that the propensity rule for counter-rotating electrons with respect to the circularly polarised field holds true for frequencies that place the interaction within the non-adiabatic regime (up to about $\gamma = 2$). This qualitatively corroborates the theoretical findings given by Barth and Smirnova in [10] and [9], as well findings by Kaushal and Smirnova [51] in that first order long-range Coulomb corrections added to PPT theory serve to diminish the ratio $\omega_+^{p-}/\omega_+^{p+}$. The long-range corrections provide a physical picture of the change in the ratio consistent with the results computed using the direct numerical integration TDSE performed in this chapter. However it is clear that approximating the effect of the Coulomb field in PPT theory does not lead to correct quantitative agreement with the TDSE and presumably experiment. As soon as significant excitation occurs at $\omega = 0.12$, PPT theory is less able to reliably predict the ionisation ratio of counter- and co-rotating electrons. PPT theory does not take into account excitation in the atomic system where as the TDSE does. In relation to experimental data on the propensity rule in argon presented by Herath *et al* [40], the maximum ionisation ratio computed through the direct numerical integration of TDSE falls just at the edge of the large error bars given by Herath *et al*. They consider a less intense pulse, but find the ratio to be anywhere between 4 and 10.

As the frequency leaves the non-adiabatic tunnelling regime and enters the multiphoton ionisation regime, the analytic theory and the propensity rule break down and we see that around $\omega = 0.19 - 0.2$ and $\omega = 0.265 - 0.3$, and possibly beyond that point, the co-rotating electron is preferentially ionised over the counter-rotating electron.

An interesting conclusion we can draw from the results presented in this

chapter, is that for all frequencies considered, there is always a larger probability to excite initial state argon from a counter-rotating m state. Co-rotating electrons have very little chance to excite up until around $\omega = 0.25$ where we see significant excitation begin to occur. Counter-rotating electrons exhibit oscillatory behaviour when plotting excitation probability against frequency (see figure 4.13). The populated states are the result of integer photon absorptions from the initial state in the highest m value available to the angular momentum number they inhabit. The reason why this behaviour is not seen in the co-rotating electron and why the only peak in excitation at $\omega = 0.28$ in figure 4.13 does not align with the peak in excitation at $\omega = 0.24$ for the counter-rotating electron is not clear. This could be an aim for future research.

Chapter 5

Transverse Electron Momentum Distributions in the Tunnelling and Over The Barrier Regimes

5.1   Introduction

Delone and Krainov predicted a Gaussian shape for the momentum distributions of photoelectrons transverse and perpendicular to the plane of polarisation of a laser field with linear or elliptical polarisation within the tunnelling regime in the strong field approximation (SFA) without Coulomb correction [29]. Since then, a great deal of experimental and numerical work has been done to check the formulae provided by Delone and Krainov. Experiments performed by Arissian *et al* [3] in argon using $800 - 1400$ nm circularly polarised light in the non-adiabatic ionisation regime concluded that the theory provided good agreement with their results. Excitation by circularly polarised light inhibits recollision with the parent-ion after ionisation and thus, the momentum distribution perpendicular to the plane of polarisation is predominantly a result of the tunnelling process.

However, the theory given in [29] was shown not to be a good predictor of momentum distributions in linearly polarised light for helium, neon and argon by Rudenko *et al* [72]. The momentum distributions perpendicular to the

110

plane of polarisation of the laser field were shown to exhibit a cusp-like shape about the origin ($p_\perp = 0$), indicating a large influence with the parent-ion after ionisation. Of particular interest is the case of argon, where the parameters used in the experiment place the interaction in the tunnelling regime. The predicted shape of the transverse momentum electron distribution (TEMD) in the SFA without Coulomb correction is Gaussian, in stark contrast to what is observed.

Ivanov further explored TEMDs for ground state hydrogen in [42] through the direct solution of the TDSE. The calculations presented in [42] were confined to the tunnelling regime to directly compare with Delone and Krainov [29]. Ivanov varied the polarisation of the pulse from linear to circular with a number of intermediary ellipticities and found the cusp-like shape observed by Rudenko *et al* [72] in calculations involving linearly or close to linearly polarised light. As the ellipticity was increased, the Gaussian shape predicted by the SFA without Coulomb correction appeared in the TEMDs. Ivanov concluded that the reason for the change in shape of the TEMD for ground state hydrogen was due to the distribution of the angular momentum number l of the resulting photoelectrons. Linear fields were shown to produce photoelectrons with relatively low angular momentum compared to that of the photoelectrons resulting from interactions with circular fields. This was deemed important to the behaviour at $p_\perp = 0$ because of the singularity at $E = 0$ in the continuum Coulomb wave function. Wave packets containing photoelectrons with distributions concentrated at low angular momentum accentuate the effect of this singularity in the form of a cusp about the origin of the TEMD.

Experimental and numerical studies were performed by Ivanov *et al* [45] in argon and neon across ionisation regimes and different polarisations of laser fields. The calculations involving argon were in the tunnelling regime and the

TEMDs displayed the same behaviour as ground state hydrogen in [42] when polarisation was varied. Agreement with Delone and Krainov [29] was found in interactions involving a high degree of ellipticity, but the cusp appeared once more when linearly polarised light was used. Neon, however, was subjected to fields in the over the barrier ionisation (OBI) regime. The TEMDs in this case were shown to be insensitive to the polarisation of the laser field and the cusp remained intact as ellipticity increased. The reasoning provided for this was that for interactions in the OBI regime, the angular momentum for photoelectrons is low, similar to that of linearly polarised light in the tunnelling regime for ground state hydrogen in [42].

We investigated the range of validity of the SFA without Coulomb correction and made comparisons with experimental work from Rudenko [72] and the theoretical results from [42] and [45] to understand the role of the interplay between the parent-ion and the electron in the TEMDs after ionisation with respect to ellipticity, ionisation regime and the initial state of the atom. By computing the momentum distribution perpendicular to the plane of polarisation, we are able to isolate the role of the parent-ion after ionisation. The TEMDs in Ivanov's work do not distinguish between the different m states of initial state argon. We present the TEMDs for $1s$ and $2p$ hydrogen in the tunnelling ionisation and OBI regimes and for $3p$ argon in the tunnelling regime, for different values of m when p orbitals are considered, to explore the effects of the Coulomb field on the electron after ionisation.

5.2 Background

Delone and Krainov [29] used the tunnelling approximation within the SFA without Coulomb correction [2] (the quasi-static limit of PPT theory that was

discussed in Chapter 4) to calculate the analytical expression for the longitudinal and transverse ionisation rates, i.e. parallel and perpendicular to the polarisation plane,

$$W(p_{\parallel}) \propto \exp\left(-\frac{1}{3}p_{\parallel}^2 \omega^2 \left(\frac{2I_p}{I}\right)^{\frac{3}{2}} \right) \tag{5.1}$$

$$W(p_{\perp}) \propto \exp\left(-p_{\perp}^2 \left(\frac{2I_p}{I}\right)^{\frac{1}{2}} \right) \tag{5.2}$$

where I_p represents the ionisation potential for the target atom and I, the peak intensity and ω the frequency. An extension to this theory for elliptically polarised light has been given in [69]:

$$W(p_{\perp}) \propto \exp\left(-p_{\perp}^2 \left(\frac{2I_p(1+\epsilon^2)}{I}\right)^{\frac{1}{2}} \right) \tag{5.3}$$

where ϵ is the degree of ellipticity. It is important to note that these formulae are Gaussian in shape about the origin and initial experiments, as mentioned above, gave reasonably good agreement between the predictions they offered and experiment for both linear and circularly polarised fields.

With the introduction of the 'reaction microscope' [28], much higher resolution experiments ($\delta p = 0.02$ a.u.) were able to be performed, along with the ability to detect the momentum of electrons and ions in all directions. Shortly after this breakthrough, many papers were published where disparities between the theory above and the experimental results were highlighted. They found, for linear polarisation, a double peak for the longitudinal momentum distribution centred at zero and a cusp-like shape at the origin for the momentum distribution transverse to the field in contradiction to the SFA without Coulomb correction [61] [72].

Figure 5.1 shows the pronounced cusp at the origin for helium, neon and
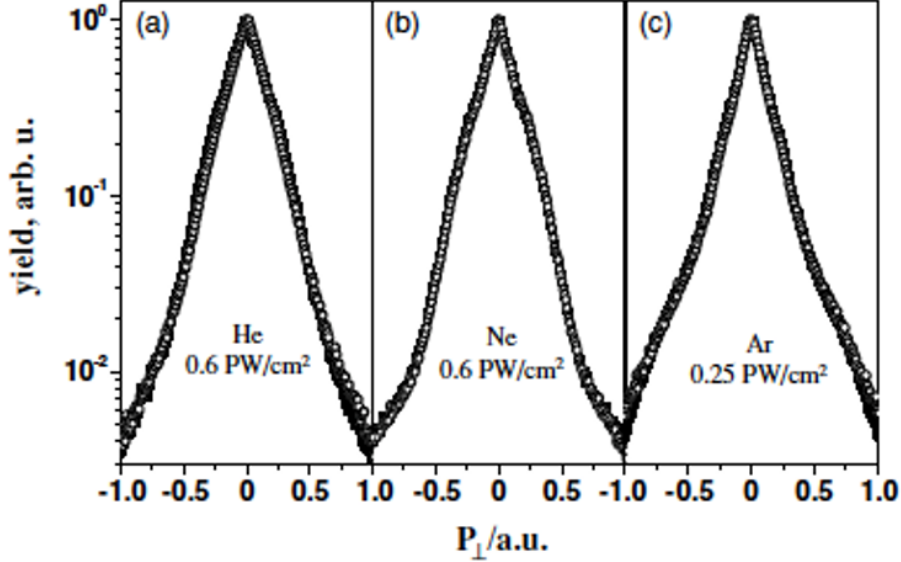
Figure 5.1: Rudenko *et al*'s [72] transverse momentum distributions for single ionisation of He (a), Ne (b) and Ar (c) by 25fs laser pulses. Note that $1PW/cm^2 = 10^{15}W/cm^2$.

argon subject to a linearly polarised pulse in the tunnelling regime. This is completely at odds with the predictions given by equation (5.3) where the Coulomb interaction is ignored after ionisation. Rudenko *et al* performed classical trajectory Monte-Carlo simulations, modified for tunnelling (CTMC-T), with and without the Coulomb potential included, as well as an SFA calculation with a Coulomb-Volkov final state. The inclusion of the Coulomb potential saw a cusp appear, which can be explained by considering the fact the electron continuum wavefunction has a singularity at zero momentum. This singularity arises from the exponential term $e^{\frac{Z\pi}{pr}}$ as $p \to 0$ in the definition of the ingoing continuum Coulomb wave function in equation (B.2) of Appendix B. This term is dominant for small p and produces asymptotic behaviour about $p = 0$. This singularity is also present in the Coulomb-Volkov state where the cusp is also seen. Excluding the Coulomb potential in the CTMC-T calculation returns the transverse momentum electron distribution (TEMD) to the Gaussian curve

predicted above. Rudenko *et al* were keen to stress that only low energy electrons are affected by the singularity of the continuum wavefunction, that is to say, electrons that have low momentum in both longitudinal and transverse directions. Finally, the cusp-like structure is unlikely to be explained through 'Coulomb-focusing' because this is known to be suppressed for pulses with too few cycles [16].
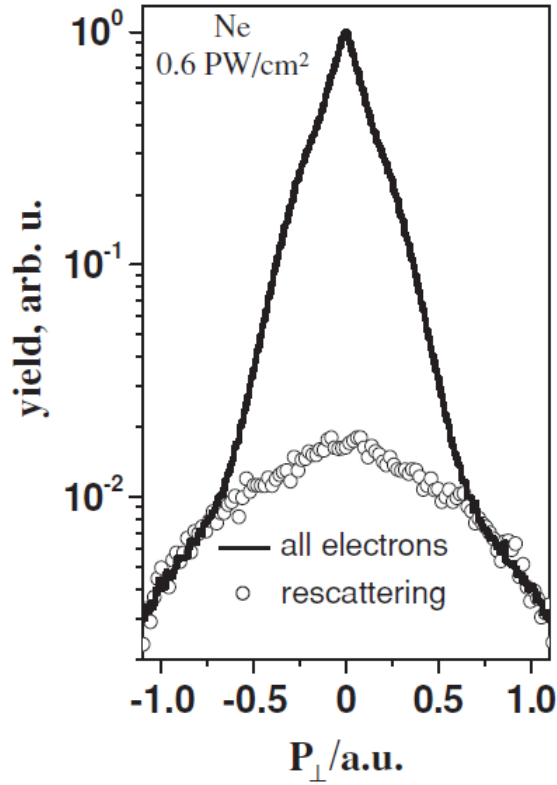
Figure 5.2: The TEMD for neon shown in 5.1 panel (b) where electrons with momentum $2\sqrt{U_p}$ have been removed [72].

There is a change in slope in each of the panels of figure 5.1 for higher momenta, however this change is most pronounced through neon in panel (b). The reason for this change of slope can be explained in figure 5.2. By omitting electrons with longitudinal momentum less than $2\sqrt{U_p}$ from their TEMD, corresponding to the maximum drift momentum that the laser field can classically impart onto the electron, the resulting plot overlays with the

change in slope. This implies that the change in slope is caused by a significant amount of rescattering. Recall that rescattered electrons can accrue energies as high as $10U_p$ if it back scatters at an angle of $180°$ off the parent-ion. Electron rescattering is included within the CTMC-T calculations, but the amount of rescattering is underestimated when compared with what is found in the experimental data.

Analogous cusp-like features have been seen before in another context, specfically ion-atom collisions. Burgdörfer (see [18] and [17]) explored the question of the cusp-like structure in the transverse electron momentum distributions about zero for helium and hydrogen when colliding with neutral targets (transverse in this context is perpendicular to the beam of projectile hydrogen or helium atoms). Burgdörfer shows that the cusp is strongly dependent on the initial state of the atom. Figures 5.3 and 5.4 show that for certain states of helium, there is a clear cusp and for $2p_0$ there is a clear reversal of this structure: an inverted cusp. The states in which a cusp appears are those where the initial state, (n, l, m), has the property that $l + m$ is even. The cusp inverts for odd $l + m$ as seen in figure 5.4. The Coulomb wave normalisation factor is defined as

$$|N(v)|^2 = \exp(\pi Z/v)|\Gamma(1 - iZ/v)|^2, \tag{5.4}$$

where Z is the charge and has a singularity at $v \to 0$ which was shown to give rise to the cusp in ion-atom collisions [17], similar to what is seen in Rudenko *et al*'s work [72] in electron-laser interactions. We show later that an inverted cusp also manifests itself in the context of laser-atom interactions.
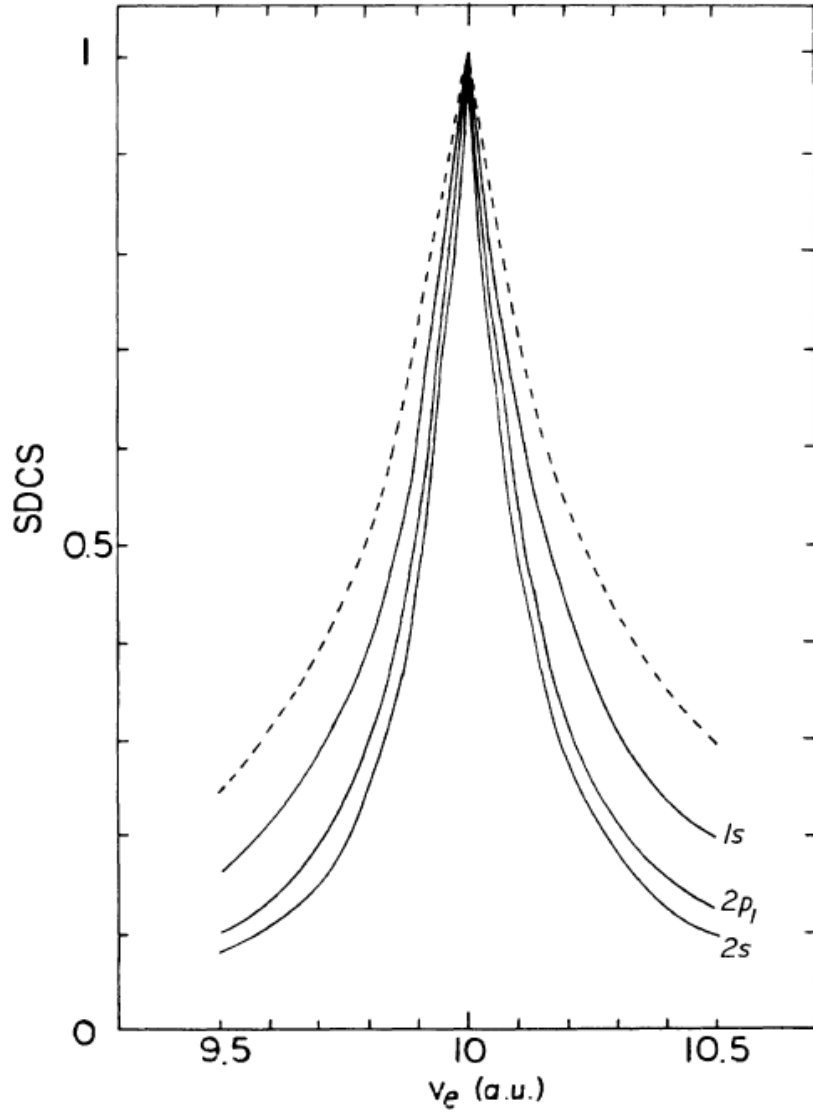
Figure 5.3: Cusp is manifest in the electron loss to continuum (ELC) for various states of He$^+$ colliding with H a velocity 10 a.u. [18].

117
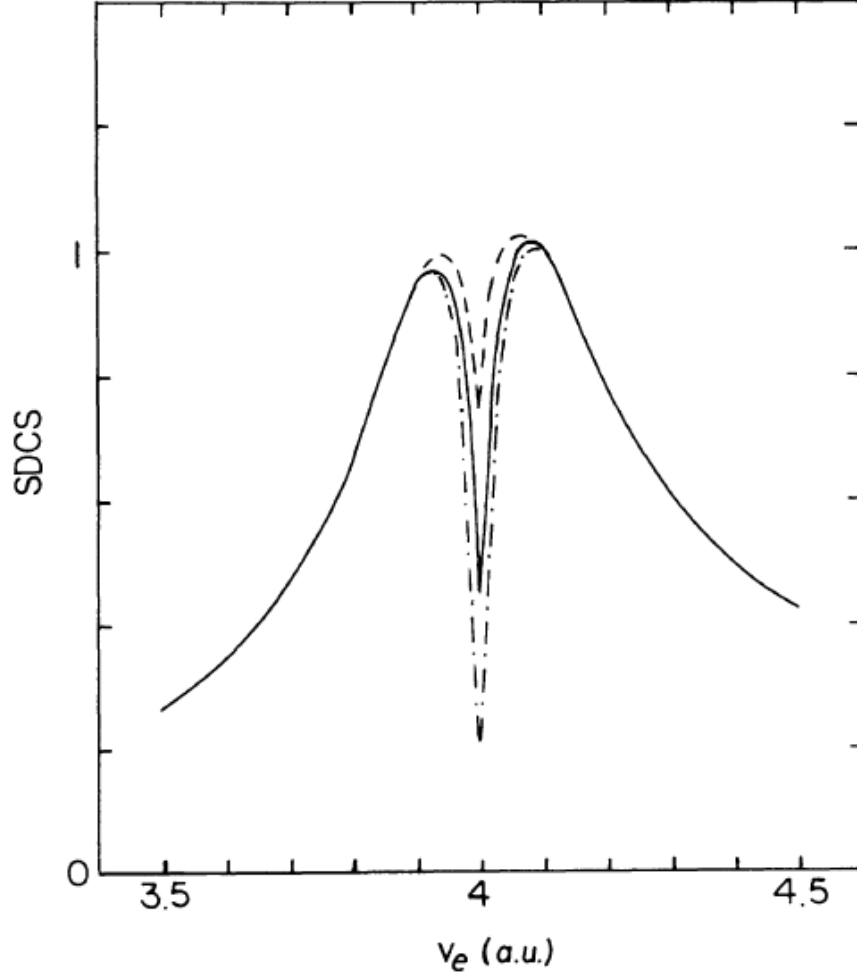
Figure 5.4: The ELC for $He^+(2p_0)$ colliding with hydrogen (solid line), helium (dashed line) and argon (dashed and dotted line) [18].

There is a marked change in electron momenta transverse to the field when considering differing degrees of ellipticity in the tunnelling regime. Ivanov [42] showed that hydrogen returns to follow the smooth Gaussian shape described in equation (5.3) as the ellipticity increases, while decreasing the ellipticity forms a cusp once more. Ivanov plotted the squared norms of $|\Psi_l|^2$ to express the idea that as one increases the ellipticity of the pulse, the likelihood of finding the electron populating low lying angular momenta decreases. Ivanov reasoned that for higher angular momentum population densities, the electron

is less likely to be found near the parent-ion and in turn, less affected by the Coulomb force. This was evidenced by the removal of the first ten angular momenta which resulted in the TEMD to become Gaussian. This is what we would expect to see when we consider the importance of the interaction between the Coulomb force and low energy electrons that Rudenko [72] emphasises is integral to the formation of the cusp at the origin.

Ivanov agreed that the origin of the cusp was indeed due to the behaviour of the continuum Coulomb wave function, however, argued that this ignored the dynamics of the ionisation process [43]. Ivanov proposes the cusp arises from behaviour of the projection of the final wave function onto the continuum Coulomb wave function about $p_\perp = 0$, the momentum perpendicular to the direction of the electric component of the laser field. In particular, Ivanov demonstrates that the first derivative of the transverse electron momentum distribution $W(p_\perp)$ is discontinuous with respect to $p_\perp$ at the origin. Therefore, if the final wave function at the end of the pulse is dominated by low energy continuum states, then this discontinuity becomes pronounced [43].

The TEMD of neon in the OBI regime subject to linearly and circularly polarised light has been demonstrated to retain the cusp about the origin when moving to circular polarisation in the most recent paper by Ivanov *et al* on this topic [45]. Again, when scrutinising the density of the angular momenta, even circularly polarised light in the OBI regime will only populate the lower l states because fewer photon absorptions are required for ionisation. Thus, the electron is more exposed to Coulombic effects.

5.3 Theory and Numerical Method

To calculate the transverse momentum electron distribution for hydrogen and argon subject to an electromagnetic field, it is necessary to first of all calculate the wave function at the end of the pulse. We do this by solving the TDSE through direct numerical integration as described in Chapter 3. After computing the final wave function, we project onto ingoing Coulomb wave functions to compute the final state momentum distribution. Finally, to compute the TEMD, we integrate over the plane of polarisation to isolate the momentum distribution of photoelectrons perpendicular to the field.

5.3.1 Hydrogen

For hydrogen, we solve the time dependent Schrödinger equation within the velocity gauge

$$i\frac{\partial}{\partial t}\Psi(\mathbf{r},t) = \left(\mathcal{H}_0 + \mathbf{A}\cdot\hat{\mathbf{p}}\right)\Psi(\mathbf{r},t) \tag{5.5}$$

and define $\mathbf{A}$ within the dipole approximation using

$$A(t) = \frac{A_0}{\sqrt{1+\epsilon^2}}f(t)\left(-\sin(\omega t + \phi)\hat{\mathbf{e}}_{\mathbf{x}} + \epsilon\cos(\omega t + \phi)\hat{\mathbf{e}}_{\mathbf{y}}\right), \tag{5.6}$$

defined as non-zero for $0 < t < 2N\pi/\omega = \tau$ with the function, $f(t) = \sin^2(\omega t/2N)$, defined as a sine squared envelope function over N cycles and ϵ being the measure of ellipticity of the pulse. If $\epsilon = 0$, the pulse is linearly polarised and if $\epsilon = 1$, the pulse is circularly polarised.

When dealing with hydrogen, we can represent the wave function in terms of Sturmian functions as described in Chapter 3:

$$\Psi(\mathbf{r}, t) = \sum_{n,l,m} c_{n,l,m}(t) \frac{S_{n,l}^{\kappa}(r)}{r} Y_{l,m}(\hat{\mathbf{r}}). \tag{5.7}$$

The Hamiltonian for equation (5.5) is tridiagonal in the atomic interaction blocks and bidiagonal in the blocks pertaining to the laser interaction. Therefore, there is at most 7 non-zero elements per row in the Hamiltonian which reduces the load on memory constraints substantially. Another advantage to using Sturmian functions is that the projection onto ingoing Coulomb functions is analytical, reducing the time expended in the calculation of the TEMD substantially. This shall be covered in detail in subsection 5.3.3.

Substituting equation (5.7) into the time dependent Schrödinger equations yields a coupled system of first order differential equations to solve at each time step solved using Crank-Nicolson, with preconditioning, of the form

$$A\mathbf{x} = B. \tag{5.8}$$

This equation is solved for $\mathbf{x}$ using the BiCGSTAB routine descibed in Chapter 3.

The direct solution of the TDSE yields a very accurate description of the wave function after an interaction with an electromagnetic field. This allows us to draw conclusions from tunnelling ionisation and OBI regimes for different initial states of hydrogen.

5.3.2   Argon

To compute the wave function at the end of the pulse in argon, we solve the following TDSE within the single active electron approximation

$$i\frac{\partial}{\partial t}\Psi(\mathbf{r}, t) = \left(\mathcal{H}_0 + \mathbf{A} \cdot \hat{\mathbf{p}}\right)\Psi(\mathbf{r}, t) \tag{5.9}$$

where

$$\mathcal{H}_0 = -\frac{1}{2}\nabla^2 + V_0(r) + W_0(r) \tag{5.10}$$

with the effective potential for argon $V_0(r) + W_0(r)$, the Muller potential [62], as described in Chapter 3.

The Hamiltonian matrix elements are only analytical for the Sturmian functions when considering hydrogenic problems. Argon requires an effective potential to correctly represent the behaviour near the core. In particular, the first 3 angular momenta are represented by the Muller potential and so numerical integration is required to evaluate the Hamiltonian matrix elements in the Sturmian basis. Instead, the basis we chose to model argon with are the B-spline functions since the elements of $\mathcal{H}_0$ for B-splines are not analytical, therefore any potential can be used in conjunction with the B-spline functions. As stated in Chapter 3, numerical integration with the B-spline basis is very fast since the mesh points used to construct the B-splines can be chosen to coincide with the abscissae of the Gaussian Quadrature.

The Muller potential [62] places a hard-core boundary condition at $R = 0.5$ a.u. which means that the linear dependencies of the Sturmian functions in equations (3.22) - (3.24) would no longer apply. Therefore, all integrations involving Sturmians would have to be performed numerically and the tridiagonal nature of the Sturmian functions would no longer hold.

The wave function then takes the form

$$\Psi(\mathbf{r}, t) = \sum_{k,l,m} c_{k,l,m}(t) \frac{B_k(r)}{r} Y_{l,m}(\hat{\mathbf{r}}). \tag{5.11}$$

Equation (5.11) is substituted into equation (5.9) to produce a system of coupled first order differential equations as we did for the Sturmian functions.

The resulting system is then solved using the Crank-Nicolson method with preconditioning and the BiCGSTAB algorithm.

5.3.3 Calculating the TEMD

To compare with the predictions of Delone and Krainov [29] with respect to the momentum distribution of photoelectrons along the axis perpendicular to the elliptical field polarisation plane given in equation (5.2), it is necessary to project the final wave function at the end of the pulse onto the ingoing scattering wave $\psi_{\mathbf{p}}^{-}(\mathbf{r})$ to produce the ionisation amplitude, $a(\mathbf{p})$, at momentum $\mathbf{p}$

$$a(\mathbf{p}) = \langle \psi_{\mathbf{p}}^{-}(\mathbf{r}) | \Psi(\mathbf{r}, \tau) \rangle. \tag{5.12}$$

With this quantity at hand, to calculate the momentum distribution along the z-axis or the TEMD, we integrate over the $x - y$ plane in momentum space with $p_z = p_\perp$:

$$W(p_z) = \int \int |a(\mathbf{p})|^2 dp_x dp_y. \tag{5.13}$$

The ingoing scattering states can be represented in terms of the Sturmian functions in the form shown below:

$$\psi_{\mathbf{p}}^{-,*}(\mathbf{r}) = \sum_{n,l,m} a_{n,l}(p) \frac{S_{n,l}^{\kappa}(r)}{r} Y_{l,m}^{*}(\hat{\mathbf{r}}) Y_{l,m}(\hat{\mathbf{p}}). \tag{5.14}$$

Note that this expresses the conjugate form of the ingoing scattering state, the representation of equation (B.1) in the Sturmian basis. The Sturmian functions are closely related to the hydrogenic radial wave functions and as such, one of the advantages in using the Sturmian basis is that there are a

large number of analytical results to draw from. In this instance, we may express the coefficient $a_{n,l}(\mathbf{p})$ in an analytic way, skipping altogether the need to project hydrogenic continuum wave functions onto the final wave function after the pulse has stopped. The coefficients are known to take the form

$$
\begin{aligned}
a_{n,l}(p) = \quad & \frac{(-1)^{n-1}}{2l+1}\sqrt{\frac{2n\kappa}{\pi}}(4l\kappa)(4i\kappa p)^l\sqrt{\frac{(n-l-1)!}{(n+l)!}} \\
& \times \frac{\Gamma[l+1-\frac{iZ}{p}]}{(\kappa^2+p^2)^{l+1}}\exp\frac{Z}{\kappa}\left(\frac{\pi}{2}-2\theta\right) \\
& \times P_{n-l-1}^{l+1}\left(\cos(2\theta);\frac{-Z}{\kappa},\frac{-Z}{\kappa}\right)
\end{aligned}
\tag{5.15}
$$

where $\theta = \arctan(p/\kappa)$. The derivation of equation (5.15) is covered in detail in Appendix B. The functions $P_n^\gamma(x;a,b)$ are the Pollaczek polynomials (see [7]) which satisfy the recurrence relation

$$
(n+1)P_{n+1}^\gamma(x;a,b) = 2[(n+\gamma+a)x+b]P_n^\gamma(x;a,b)-(n+2\gamma-1)P_{n-1}^\gamma(x;a,b)
\tag{5.16}
$$

for $n > 0$ and $P_0^\gamma(x,a,b) = 1$ and $P_1^\gamma(x,a,b) = 2[(\gamma+a)x+b]$. The Pollaczek polynomials also have the generating function

$$
\sum_{n=0}^{\infty} P_n^\gamma(x,a,b)t^n = (1-te^{i\theta})^{-\gamma+iw(\theta)}(1-te^{-i\theta})^{-\gamma-iw(\theta)}
\tag{5.17}
$$

where $x \in [-1,1]$, $x = \cos(\theta)$, $w(\theta) = (a\cos(\theta)+b)/\sin(\theta)$. Two other interesting properties of the Pollaczek polynomials are that for $a = b = 0$, they reduce to the Legendre polynomials and that they are orthogonal when the conditions $a \geq |b|$ and $\gamma > 0$ are satisfied.

Substituting equation (5.14) into equation (5.12) and integrating with

$\Psi(\mathbf{r}, \tau)$ given in equation (5.7) and using the analytical coefficients in equation (5.15), we are able to write the ionisation amplitude like so

$$a(\mathbf{p}) = \sum_{l,m} \left[\sum_{n',n} a_{n,l}(p) c_{n',l,m}(\tau) \int_0^\infty S_{n',l}^\kappa(r) S_{n,l}^\kappa(r) dr \right] Y_{l,m}(\hat{\mathbf{p}}) \qquad (5.18)$$

where we make use of the property

$$\int_0^\infty S_{n',l}^\kappa(r) S_{n,l}^\kappa(r) = 0, \qquad |n' - n| > 1 \qquad (5.19)$$

to restrict the inner sum to $n - 1 \leq n' \leq n + 1$ and the integrals

$$\int_0^\infty S_{n',l}^\kappa(r) S_{n,l}^\kappa(r) \qquad |n' - n| \leq 1 \qquad (5.20)$$

are all known analytical functions of κ, n and l, which helps to speed up the calculation further still.

We then transform to cylindrical coordinates in momentum space so that for $p_\rho^2 = p_x^2 + p_y^2$ and $\theta = \arctan(p_\rho/p_z)$. On substituting into equation (5.13) and integrating over ϕ, which reduces the double sum to a single sum over m due to a factor of $\delta_{m,m'}$, we finally have:

$$\int \int |a(\mathbf{p})|^2 dp_x dp_y = \int \sum_{l,l',m} I_{l',m}^*(p) I_{l,m}(p) P_{l',m}(\cos(\theta)) P_{l,m}(\cos(\theta)) p_\rho dp_\rho \tag{5.21}$$

where

$$I_{l,m}(p) = \sum_{n',n} a_{n,l}(p) c_{n',l,m}(\tau) \int_0^\infty S_{n',l}^\kappa(r) S_{n,l}^\kappa(r) dr \qquad (5.22)$$

is an entirely analytical quantity provided the coefficients $c_{n,l,m}(\tau)$ have been

calculated beforehand. The integral in equation (5.21) is calculated for each p_z by fixing p_z and integrating over p_ρ numerically.

The calculation of the TEMDs for argon adds an additional level of computational complexity. The first few angular momenta of the wave function for argon are unable to be represented in terms of Sturmian functions and so, it is necessary to use B-spline functions to represent the wave function instead. The projection onto the ingoing Coulomb functions is not analytical for the B-spline functions and so equation (5.15) cannot be used to skip this integration. Denoting the number of points considered in our integration along p_ρ as N_{p_ρ}, amounts to having to perform $N_{p_\rho} \times \frac{N_l}{2} * (N_l + 1)$ (the total number of (l, m) pairs considered) integrations per $p_\perp$ along the transverse direction.

Switching to the B-spline basis changes the way we compute the quantity $I_{l,m}(p)$. We instead project the final wave function onto an ingoing Coulomb wave function defined as

$$\psi_{\mathbf{p}}^{-,*}(\mathbf{r}) = \frac{1}{\sqrt{p}} \sum_{l=0}^{\infty} \sum_{m=-l}^{l} (-i)^l e^{i\delta_l} \phi_E^l(r) Y_{l,m}^*(\hat{\mathbf{r}}) Y_{l,m}(\hat{\mathbf{p}}) \qquad (5.23)$$

where $\delta_l = arg(\Gamma[l+1-iZ/p])$ is the Coulomb phase shift in the lth partial wave and $\phi_E^l(r)$ is the energy normalised radial Coulomb function which is computed using the algorithm in [64]. Substituting equation (5.23) into equation (5.12) we can compute equation (5.13) and we get $I_{l,m}(p)$ given by

$$I_{l,m}(p) = \frac{(-i)^l e^{i\delta_l}}{\sqrt{k}} \int_0^{r_{max}} \phi_E^l(r) \sum_{k=1}^{N} c_{k,l,m}(\tau) B_k(r) dr \qquad (5.24)$$

where N is the total number of B-splines we use to represent each (l, m) pair. From this point, we can simply perform the integration in equation (5.21).

Both representations for the wave functions as described above were used to compute TEMDs in hydrogen as a check, but for argon, we only used B-

splines. Note that we neglected the non-Coulomb behaviour of the first few partial waves in argon by projecting solely on Coulomb functions. We have found this to have negligible effect on the energy distribution at the end of the pulse when comparing the projection of the final wave function onto ingoing Coulomb wave functions and through the pseudo state method outlined in equation (4.42).

The energy and the angle resolved spectrum associated with the wave function $\Psi(\mathbf{r}, \tau)$ can be calculated by projecting onto the ingoing Coloumb wave function of momentum $\mathbf{p}$ like so

$$\frac{\partial P}{\partial E \partial \Omega_k}(E, \theta_k, \phi_k) = |\langle \psi_{\mathbf{p}}^-(\mathbf{r}) | \Psi(\mathbf{r}, \tau) \rangle|^2. \quad (5.25)$$

5.4 Results

To study the effect on the dynamics of electrons in the transverse direction as we move from linear to circular light in both the tunnelling regime and the OBI regime, we initially focus on hydrogen. It is critical to be able to distinguish which ionisation regime a specific interaction lies in order to contextualise the electron behaviour. The parameter in equation (4.35) defines the point at which over the barrier ionisation becomes dominant. Ivanov defines the parameter E_{OBI} slightly differently due to the definition of the circularly polarised field in [45] being such that $I = E_0^2$ rather than $I = 2E_0^2$ given here. If $E_0 < E_{OBI}$ and the Keldysh parameter is such that $\gamma < 1$ then adiabatic tunnelling is the dominant mechanism for ionisation. If $\gamma \approx 1$ with $E_0 < E_{OBI}$ then non-adiabatic tunnelling takes over and finally, if $E_0 > E_{OBI}$ we find ourselves in the OBI regime.

Ivanov moves from the tunnelling regime to the OBI regime by considering

argon and neon, respectively. Argon in the $3p$ state requires a peak intensity of $I_{OBI} = 9.9 \times 10^{14} W/cm^2$ while neon requires just $I_{OBI} = 1.1 \times 10^{13} W/cm^2$. The choice of intensities that Ivanov *et al* employ for both atoms leaves $\gamma \approx 0.7$ [45].

The point at which over the barrier ionisation becomes dominant for $1s$ hydrogen is $I_{OBI} \approx 2.74 \times 10^{14} W/cm^2$, whereas for $2p$ hydrogen, the peak intensity required to enter the OBI regime is a mere $I_{OBI} \approx 1.1 \times 10^{12} W/cm^2$. By choosing peak intensity $I = 10^{14} W/cm^2$ we are able to scrutinise both regimes with relative ease while keeping the laser parameters fixed.

We vary the ellipticity of the pulse but choose the duration and wavelength of the laser to be fixed at 4 cycles and 800 nm to compare with results by Ivanov in [42] and [45]. The Keldysh parameter for $1s$ and $2p$ hydrogen subject to these conditions is $\gamma \approx 1.5$ and $\gamma \approx 0.75$, respectively.

Convergence was achieved with 400 Bsplines, 50 total angular momenta ($l_{max} = 49$ for $1s$ hydrogen, $l_{max} = 50$ for $2p$ hydrogen) and a time step of $\delta t = 0.05$ a.u. in all cases for hydrogen. A total number of 50 angular momenta amounts to 1275 (l, m) pairs or the sum of the first 50 integers.

5.4.1 Atomic Hydrogen in the Tunnelling Regime

To consider the two different regimes, tunnelling and OBI, we calculate the TEMD from $1s$ and $2p$ initial state hydrogen, respectively. We shall also distinguish between $m = 0$ and $m = 1$ for $2p$ hydrogen ($m = 1$ and $m = -1$ are symmetric).

To investigate the dampening of the cusp in the tunnelling regime as a function of ellipticity, we calculated TEMDs for $\epsilon = 0, 0.25, 0.5, 0.75$ and 1. The purple TEMD in figure 5.5 exhibits the cusp-like feature about $p_\perp = 0$ for the linear polarisation case that Rudenko *et al* [72] also observed in helium,

neon and argon for linear pulses in the tunnelling regime. Another feature that is similar to figure 5.1 is the change in slope at 0.25 a.u. attributed to rescattering after omitting electrons with momentum below $2\sqrt{U_p}$. We see the cusp and a very slight change in slope persist when moving to $\epsilon = 0.25$.

When increasing the ellipticity to $\epsilon = 0.5$, the cusp is barely visible and a semblence of a Gaussian curve begins to emerge, signalling the point at which we may say the SFA without Coulomb correction [29] is a good predictor of electron behaviour in the transverse direction. By the time we reach $\epsilon = 0.75$ and the fully circular case, the Gaussian shape consistent with the formulae given by Delone and Krainov [29] and Popov [69] within the strong field approximation is clearly shown. The change in slope seen in linearly polarised light is not present in the TEMD for circularly polarised light suggesting negligible electron-ion rescattering which is expected from a circular field. It is then evident that the SFA without Coulomb correction breaks down in the tunnelling regime for linearly polarised light.
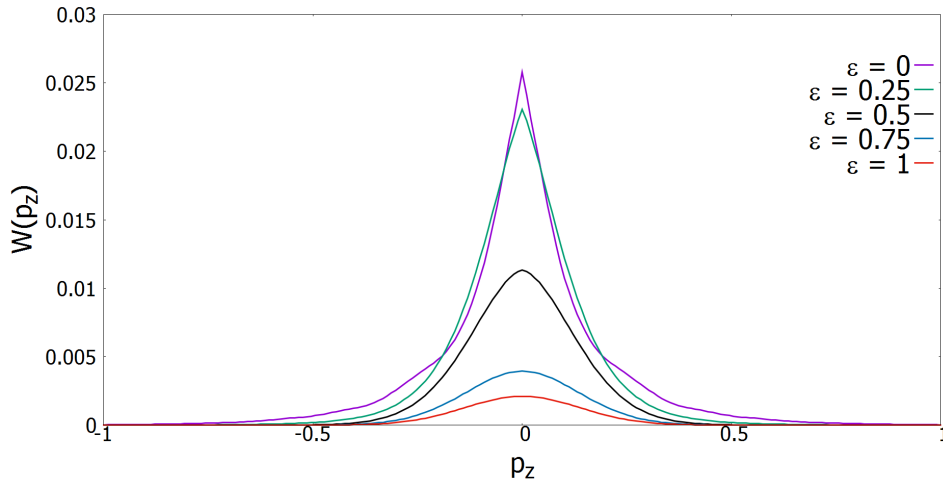
Figure 5.5: (Colour online) TEMD after the initial ground state was subjected to a 4 cycle 800 nm pulse with peak intensity $10^{14} W/cm^2$. A cusp can be seen in $\epsilon = 0$ and 0.25, this cusp evolves into a Gaussian curve as we move to circular polarisation.

The cusp can be explained when we consider the distribution of the angular

momentum number l as we move from linear to circular polarisation in conjunction with the fact that the normalisation constant of the continuum wave function in Coulomb field has a singularity about $p = 0$. If one observes a large proportion of low energy photoelectrons after the pulse, then this singularity becomes very apparent in the form of a cusp in the TEMD as p_z or $p_\perp \to 0$.

Figure (5.6) displays one reason for the breakdown of the cusp after ground state hydrogen was subjected to a linearly and circularly polarised field by taking the square norm of the wave packet for each l over the states in the continuum after converting to the atomic basis

$$|\Psi(\mathbf{r}, t)_l|^2 = \sum_{-l \leq m \leq l} \sum_k |a_{k,l,m}(\tau)|^2 \qquad (5.26)$$

where $a_{k,l,m}(\tau)$ are the coefficients of the wave function in the atomic basis defined in subsection 4.4.5 of Chapter 4.

The ionised electron for linearly polarised light (figure 5.6a) is most likely to populate angular momenta in the range $0 < l < 15$ with a peak at $l = 7$. The circular case shows a shift upward for the continuum wave function to be most densely populated around $l = 18$ lending further credence to the theory that the cusp is based on the preponderance of low l and low energy photoelectrons described in [42].
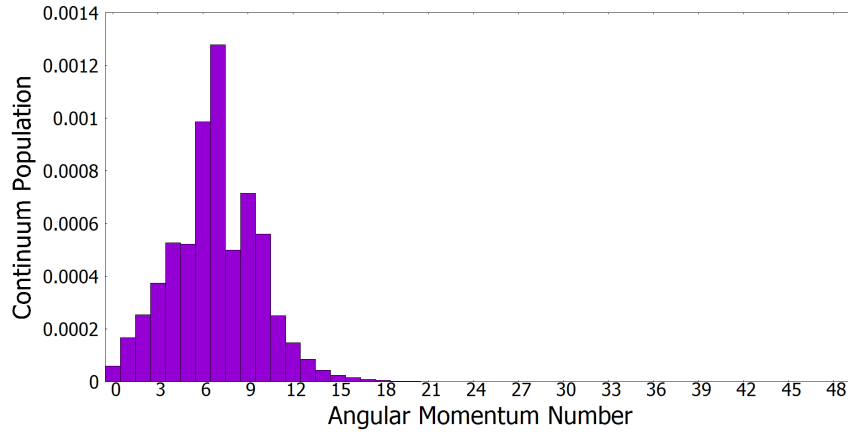
(a) Linearly polarised light
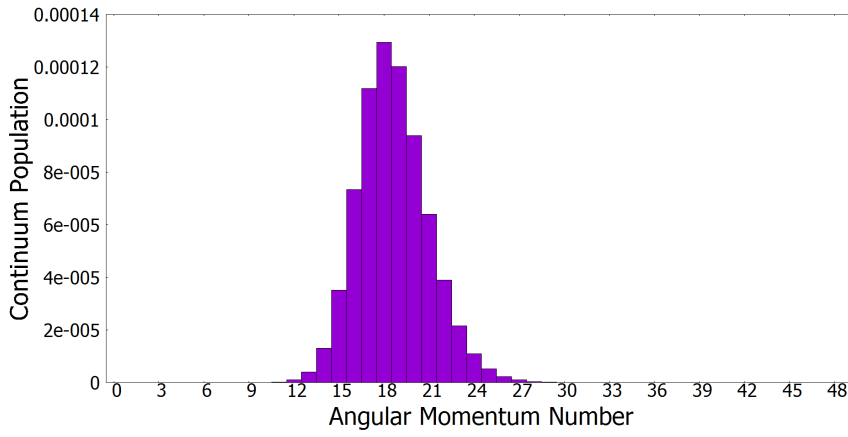
(b) Circularly polarised light

Figure 5.6: The density of l states in the continuum after initial state $1s$ hydrogen was subject to a 4 cycle, 800 nm pulse with peak intensity $10^{14}W/cm^2$.
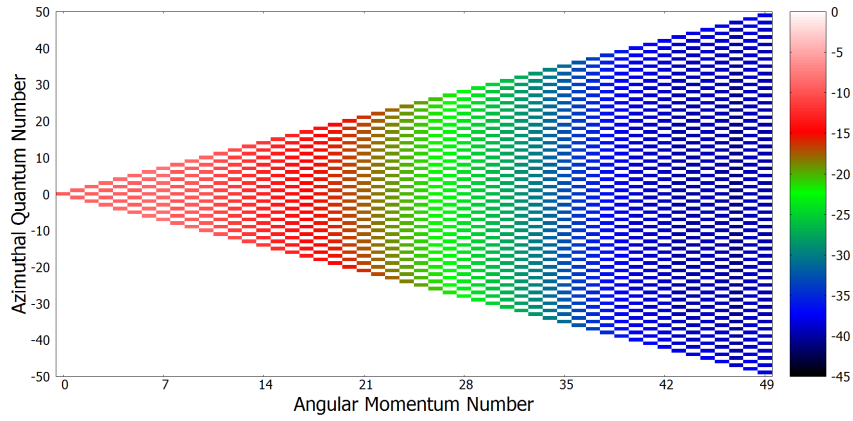
(a) Linearly polarised light
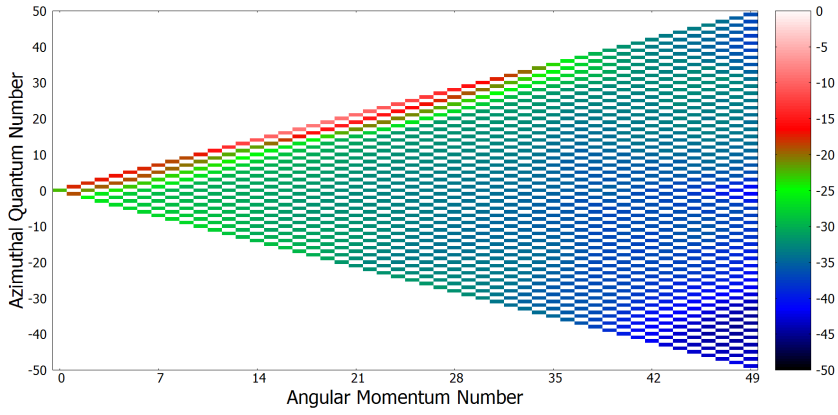
(b) Circularly polarised light

Figure 5.7: The density of (l, m) states in the continuum after initial state $1s$ hydrogen was subject to a 4 cycle, 800 nm pulse with peak intensity $10^{14} W/cm^2$. The numbering down the scale on the right of the density plot represents descending powers of 10. All density plots of (l, m) states in this chapter have this in common.

The distribution of m states is also different depending on the polarisation of the light source. Since the propagation direction of our field is along the z-axis, the linear field has different selection rules than the conventional $l \to l\pm1$, $m \to m$ when a photon is absorbed. Instead the selection rule is $l \to l \pm 1$, $m \to m \pm 1$. By plotting the distribution of (l, m) continuum states in figure 5.7, we can see a very evenly spread population density between the m states, something we would expect from a linearly polarised pulse. On the other hand, for circularly polarised light there is a very clear propensity for the positive m states to be populated. This would of course be the opposite should the direction of the circular field reverses. Populating higher m states in larger proportions than lower m states serves to push the electron further still from the parent-ion after ionisation has occurred reducing the effect of the Coulomb force.

5.4.2   Over the Barrier Ionisation Regime

To investigate the OBI regime, we alter the initial state of our system. Specifically we chose the initial states $2p$, $m = 0$ and $2p$, $m = 1$. The minimum peak intensity required in the OBI regime for a 4 cycle, 800 nm pulse and considering the $I_p = 0.125$ a.u. in these cases is $I_{OBI} = 1.1 \times 10^{12} W/cm^2$. The intensity we selected for our calculations was much higher at $I = 10^{14} W/cm^2$, placing the interactions squarely within the OBI regime.

We look to compare with the results given by Ivanov *et al* [45] for neon in the OBI regime subject to a 4 cycle 800 nm pulse with $I = 2 \times 10^{14} W/cm^2$. Figure 5.8 displays Ivanov *et al*'s TEMD from [45] for metastable Ne* subject to the linearly polarised pulse, we see there is reasonably good agreement with experiment and a cusp at the origin in line with findings by Rudenko [72].

Figure 5.9 shows the TEMD for Ne* subject to the circularly polarised
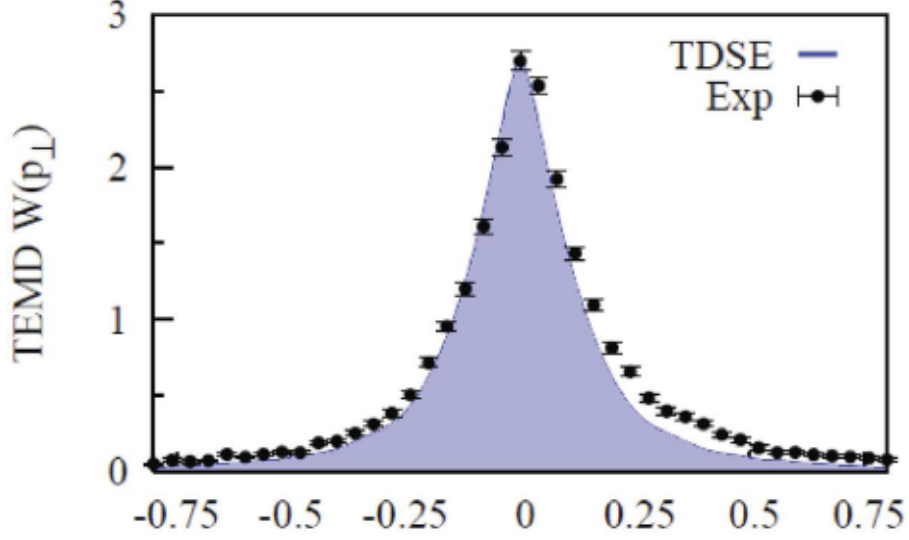
Figure 5.8: Metastable Ne* subject to subject to a linearly polarised 4 cycle 800 nm pulse with $I = 2 \times 10^{14} W/cm^2$. The points are experimental values [45].

pulse. The experimental values are offset towards $p_\perp > 0$ while the calculated values from the TDSE are symmetric about the origin. A cusp is also clearly seen in the circularly polarised case for the OBI regime. It is important to be aware in the following discussion that Ivanov *et al* sum over the initial m states and do not present TEMDs for individual initial m states. We shall present results for $2p$, $m = 1$ hydrogen and $2p$, $m = 0$ separately.

Figure 5.10 displays the cusp about p_z or $p_\perp = 0$ for both types of pulse. We observed a slight change in slope for the TEMD attributed to the linear pulse in line with findings from Rudenko *et al* suggesting that rescattering is also present in the OBI regime for linear polarisation (shown in purple in figure 5.10). Again, there is little evidence of rescattering in the TEMD corresponding to the circular pulse (shown in green in figure 5.10). Fewer photon absorptions to ionise is indicated in the distribution of continuum l states (figure 5.11). There is a higher probability of finding the electron in s and p states after being exposed to linear light, however, the distributions between
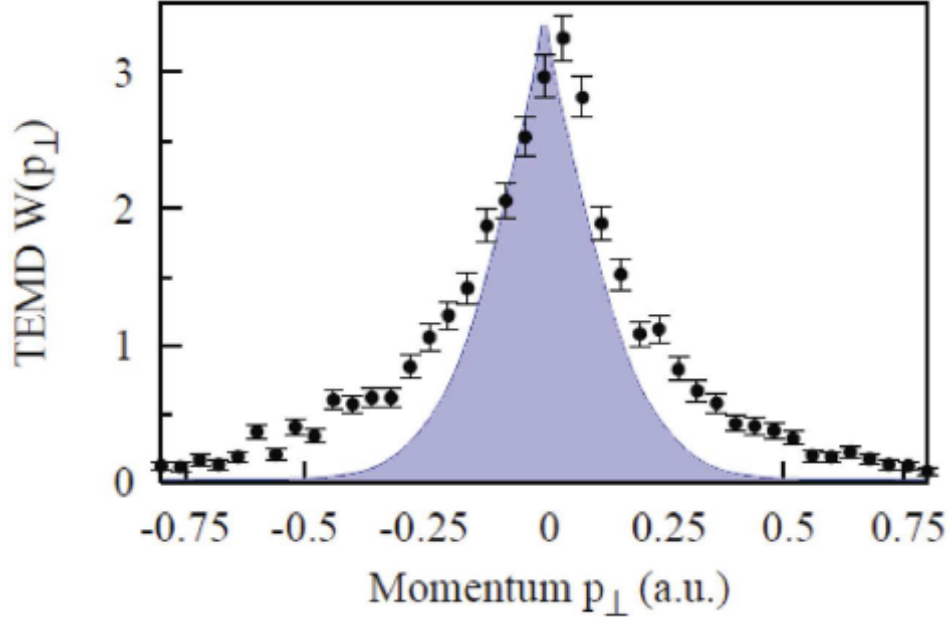
Figure 5.9: Metastable Ne* subject to subject to a circularly polarised 4 cycle 800 nm pulse with $I = 2 \times 10^{14} W/cm^2$. The points are experimental values [45].
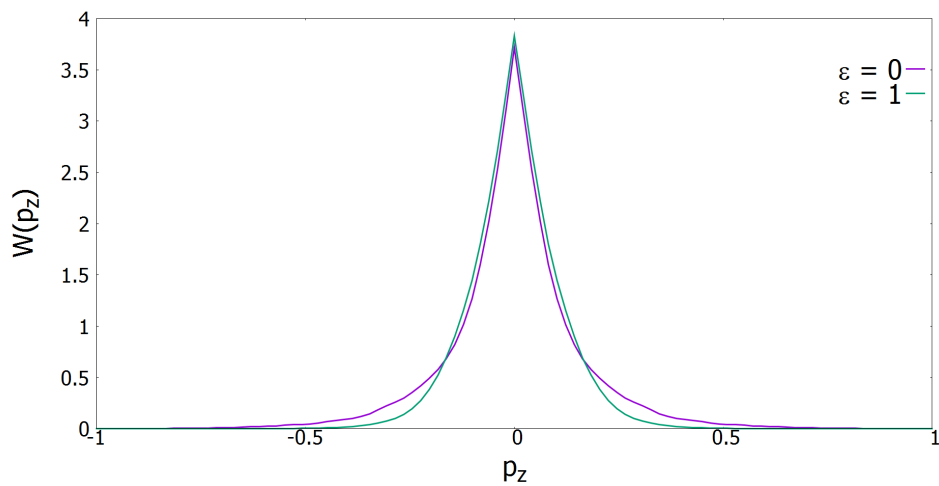
Figure 5.10: The TEMDs of initial state $2p$, $m = 1$ hydrogen after being subjected to a 4 cycle, 800 nm pulse with peak intensity $10^{14} W/cm^2$. Both linear (purple line) and circular (green line) light caused a cusp-like structure in the subsequent transverse momentum distributions for the ionised electrons.

the two types of pulse are largely the same. Both are densely populated in the lower l states, and thus are likely to be found closer to the parent-ion where the attractive Coulomb force remains a dominant feature, presenting a complete breakdown of the SFA without Coulomb correction to describe transverse electron dynamics in the OBI regime.

If we compare our findings in figure 5.10 with those of Ivanov *et al* in figures 5.8 and 5.9, we see good qualitative agreement between metastable Ne* and $2p$ hydrogen in the OBI regime.

Figure 5.12a tells a similar story to figure 5.7 in that the density of continuum (l, m) states is evenly spread over m for linear polarisation. The difference between the two figures however is seen in figures 5.7b and 5.12b. The majority of the density of continuum (l, m) states are almost exclusively found in (l, l) and $(l, l - 2)$ states for the tunnelling regime. Interestingly, in the OBI regime, there is a much greater spread of m states that are significantly populated per l.
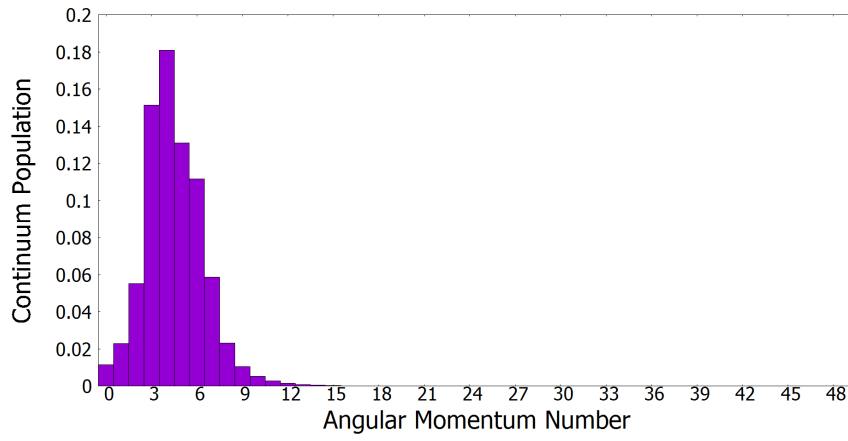
(a) Linearly polarised light
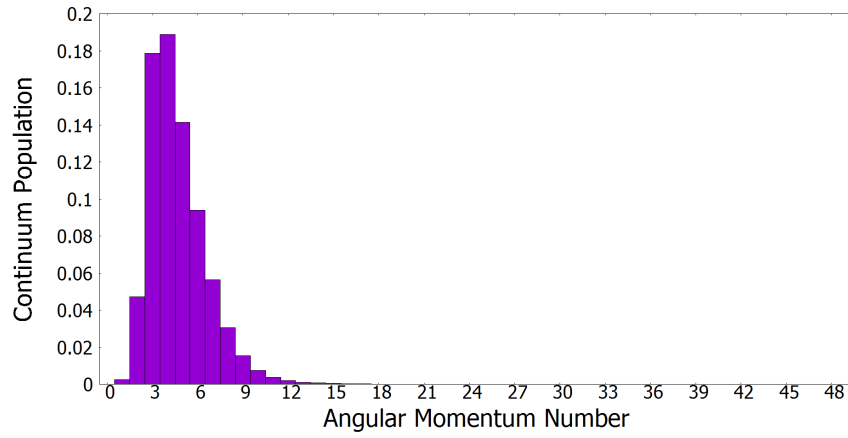
(b) Circularly polarised light

Figure 5.11: The density of l states in the continuum after initial state $2p$, $m = 1$ hydrogen was subject to a 4 cycle, 800 nm pulse with peak intensity $10^{14}W/cm^2$.

(a) Linearly polarised light

(b) Circularly polarised light

Figure 5.12: The density of (l, m) states in the continuum after initial state $2p$, $m = 1$ hydrogen was subject to a 4 cycle, 800 nm pulse with peak intensity $10^{14} W/cm^2$.

5.4.3 The Inverted Cusp
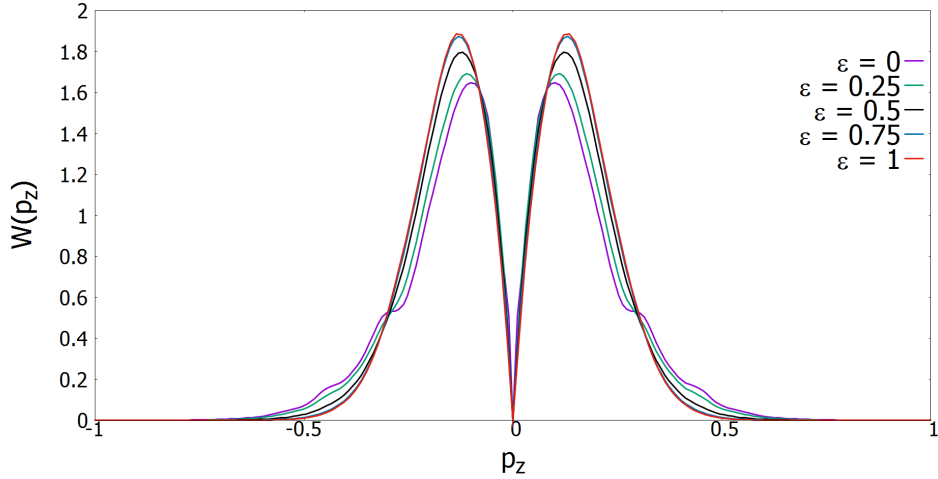
Figure 5.13: The TEMDs of initial state $2p$, $m = 0$ hydrogen after being subjected to a 4 cycle, 800 nm pulse with peak intensity $10^{14} W/cm^2$. All ellipticities exhibit the feature of an inverted cusp at the origin.

We next change the initial state to $2p$, $m = 0$ hydrogen. In this case we find an inverted cusp for the TEMD for all ellipticities as seen in figure 5.13. This is analogous to what Burgdörfer found in [17] for ion-atom collisions where the initial state has odd parity, i.e. $l + m$ is odd. The selection rules for both linear and circular pulses from $2p$, $m = 0$ exclude any states where the parity of (l, m) is even. The relevance of this becomes clear when one plots $|Y_{l,m}|^2$ for (l, m) odd and (l, m) even. Figure 5.14 shows the regions electrons can inhabit, figure 5.14a shows that the $x - y$ plane is able to be accessed by electrons in the $(l, m) = (0, 0)$ state. For states in $(l, m) = (1, 0)$, however, the value of $Y_{1,0}(\frac{\pi}{2}, \phi)$ in the $x - y$ plane (where $z = 0$) is 0, and so no electrons can be found with momentum $p_z = 0$ when the initial state has odd parity and has the selection rules $l \rightarrow l \pm 1$, $m \rightarrow m \pm 1$. Plotting any $|Y_{l,m}|^2$ for (l, m) odd will show that the function reduces to zero at any point on the $x - y$ plane.

Since Ivanov et al did not perform separate TEMDs for Ne* in the OBI regime, the effect of choosing an initial state with odd parity was masked

behind the large cusp-like features in the TEMDs for the initial states with even parity in figures 5.8 and 5.9.

The linear TEMD in figure 5.13 has two clear changes in slope. This can be explained by the rescattering theory given by Rudenko *et al* [72] that has been seen in $1s$ and $2p$, $m = 0$ TEMDs for linear polarisation in the figures 5.5 and 5.10, however in this instance it suggests there are multiple rescatterings occurring. We see the same rescattering to a lesser extent in the case of $\epsilon = 0.25$, meaning that there rescattering occurs regardless of whether your initial state is $1s$ or $2p$. Again, when we reach $\epsilon = 0.5, 0.75$ and 1, there is no evidence of a change in slope that can be attributed to rescattering.

We can see that there is zero chance for an electron to be found with zero transverse momentum in all cases, which corroborates the fact that the parity of the initial state dictates the behaviour of low transverse momentum electrons in a very distinct manner: the complete inversion of the cusp at zero transverse momentum in the OBI regime.

The density plots of the l and (l, m) states (figures 5.15 and 5.16, respectively) are very similar to that of $2p$, $m = 1$. Both types of pulse only incur population in low l states and the (l, m) density plot for the circular pulse (figure 5.16b) features a higher spread of m states that are populated per l than the initial state of $1s$ populated in figure 5.7b. It is important to note that we are in the OBI regime here and that we should expect to see effects of the Coulomb potential due to the preponderance of low l electrons in the continuum. There will be a comparison between initial state argon with odd and even parity to determine the effect that the Coulomb force has on the TEMD in the tunnelling regime.
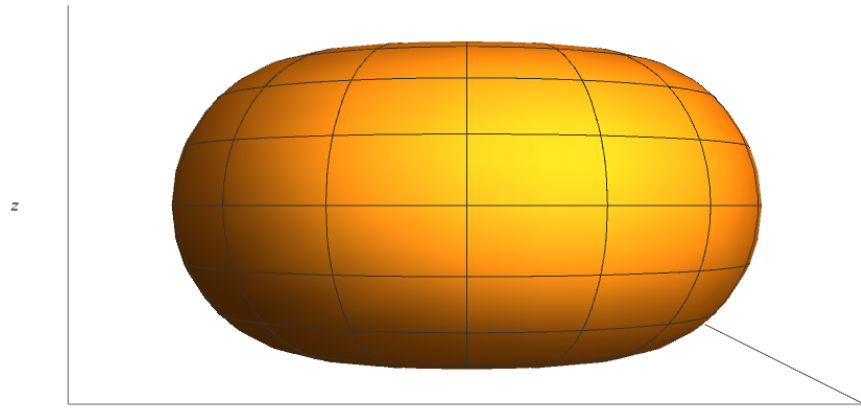
(a) $|Y_{0,0}|^2$
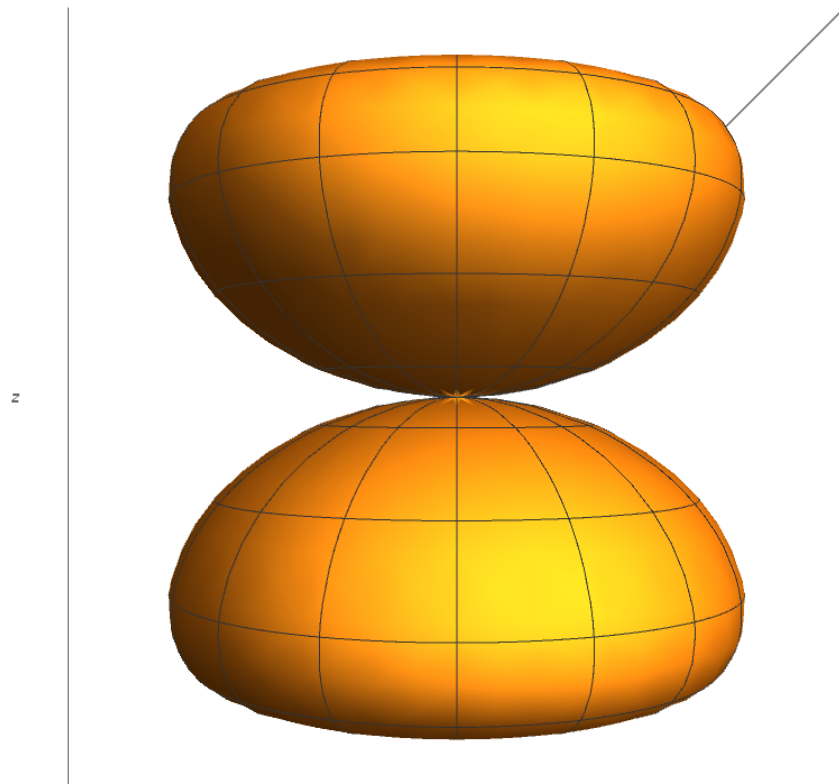
(b) $|Y_{1,0}|^2$

Figure 5.14: Plots of $|Y_{l,m}|^2$ showing the regions electrons are able to exist in for (l, m) states $(0, 0)$ and $(1, 0)$.
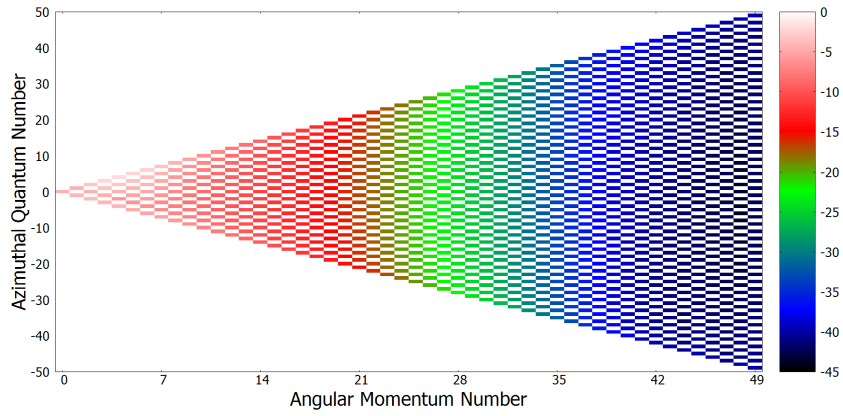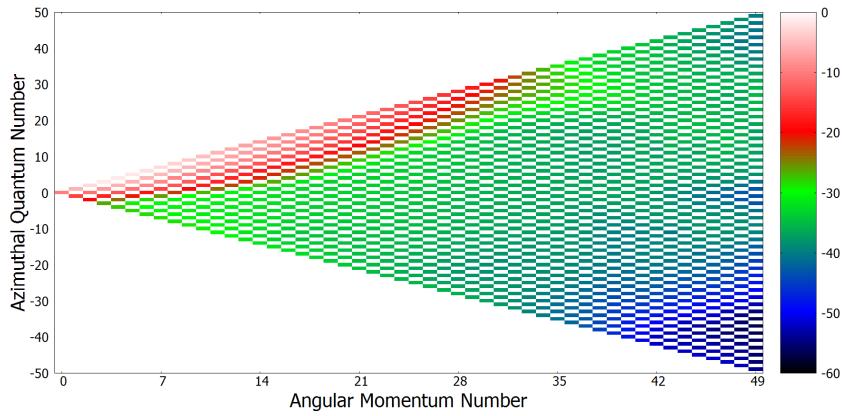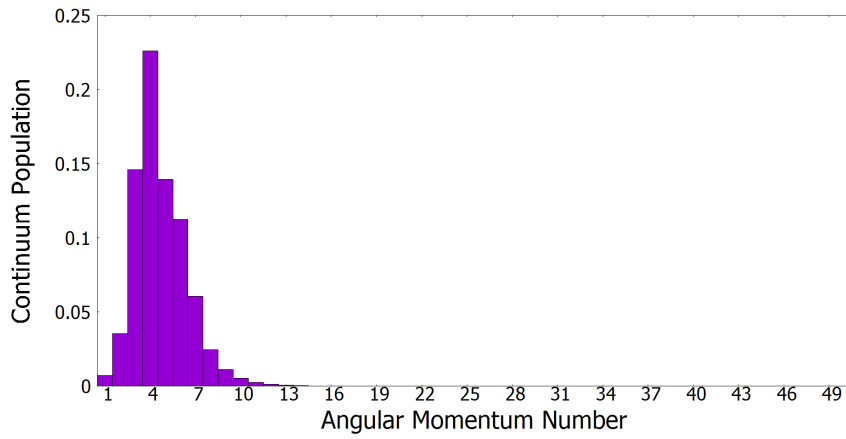
(a) Linearly polarised light
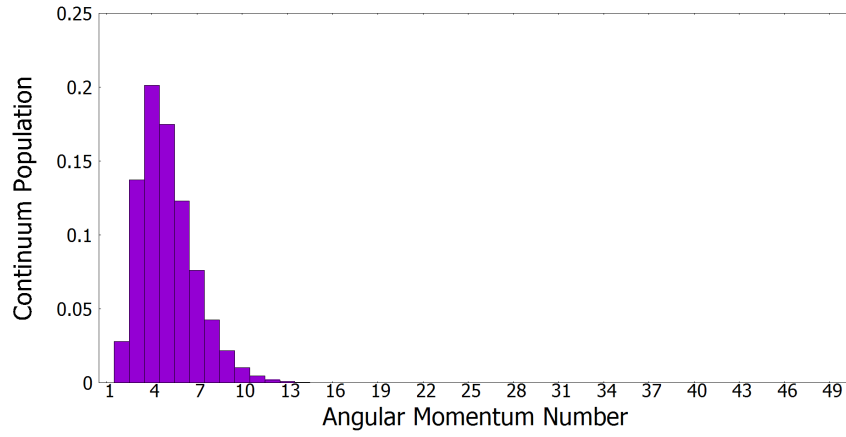
(b) Circularly polarised light

Figure 5.15: The density of l states in the continuum after initial state $2p$, $m = 0$ hydrogen was subject to a 4 cycle, 800 nm pulse with peak intensity $10^{14}W/cm^2$.
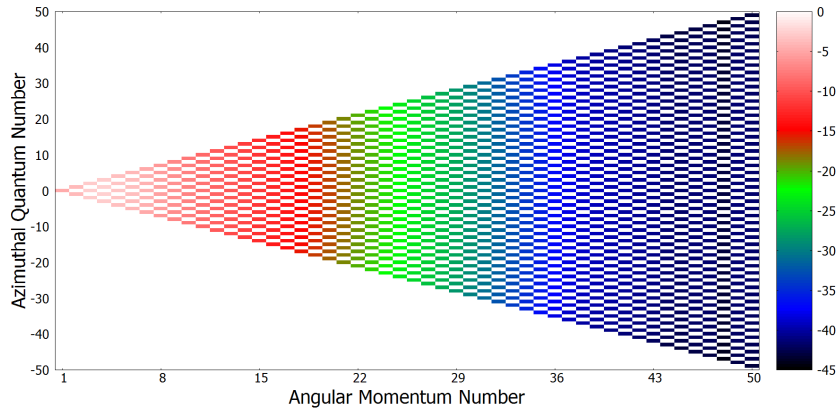
(a) Linearly polarised light
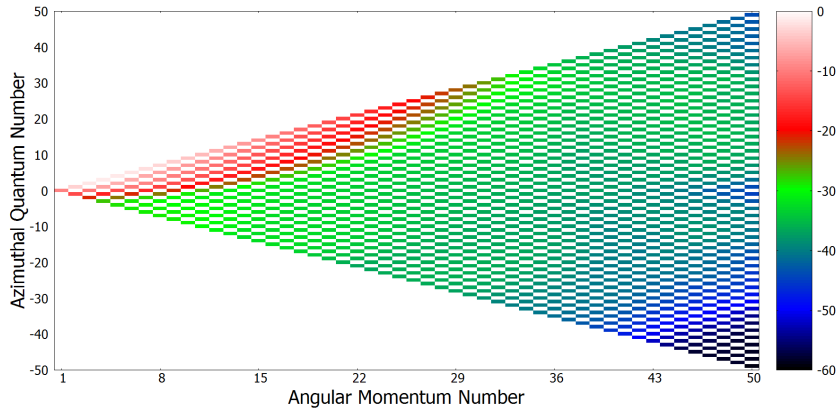

(b) Circularly polarised light

Figure 5.16: The density of (l, m) states in the continuum after initial state $2p$, $m = 0$ hydrogen was subject to a 4 cycle, 800 nm pulse with peak intensity $10^{14}W/cm^2$.

5.5   Argon in the Tunnelling Regime

Ivanov *et al* [45] produced results both experimental and numerical to suggest
that this cusp extends to argon and neon. They showed the persistence of the
cusp in neon but dampening of the cusp in argon in figure 5.18 as the ellipticity
of their respective fields increased, exactly what was seen for hydrogen in
the same regimes. Interestingly, however, the experimental results did not
overlay with the numerical results. In fact they observed good agreement
for calculations involving linear fields seen in figures 5.17 and 5.8, but gradual
divergence between experimental and numerical results in both neon and argon
as the ellipticity increased. The experimental TEMDs displayed much broader
distributions and even a small amount of asymmetry about the origin.

We chose to examine the behaviour of electron momentum transverse to
the field in $3p$, $m = 0$ and $3p$, $m = 1$ argon. This leaves us with one initial state
with even parity and the other with odd parity, allowing us to directly compare
with the behaviour shown in hydrogen in the tunnelling and OBI regimes and
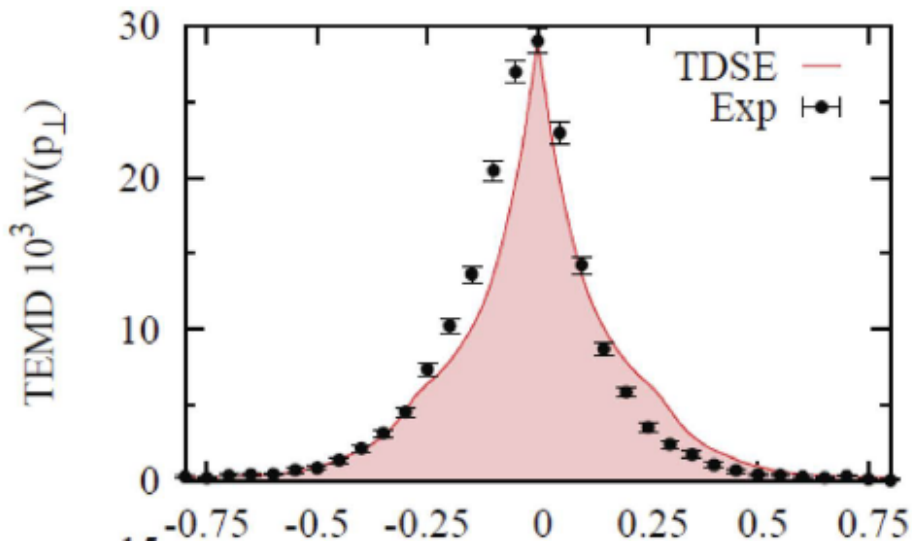
Figure 5.17: Ground state $3p$ argon subject to subject to a linearly polarised
4 cycle 800 nm pulse with $I = 4.8 \times 10^{14} W/cm^2$. The points are experimental
values [45].
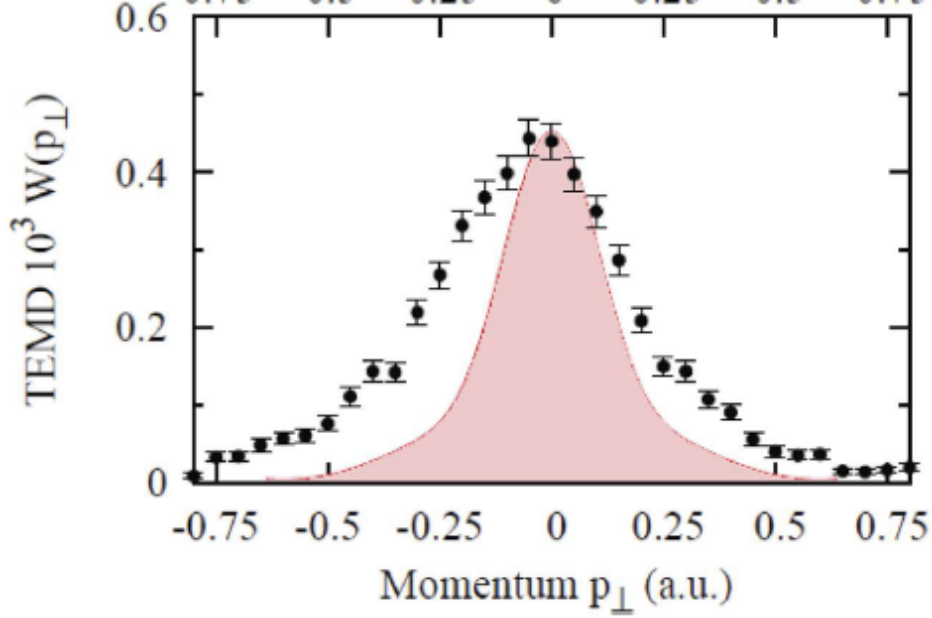
Figure 5.18: Ground state $3p$ argon subject to subject to a circularly polarised 4 cycle 800 nm pulse with $I = 4.8 \times 10^{14} W/cm^2$. The points are experimental values [45].

to disentangle the information given by Ivanov *et al* in figures 5.17 and 5.18 where the contribution from individual m values are hidden. Note, that in the dipole approximation and single active electron (SAE) approximation, the selection rules for argon mirror that of hydrogen.

Within the SAE and knowing that the binding potential of ground state argon is $I_p = 0.5821$ a.u., we must select the peak intensity of our field to be $I < I_{OBI} \approx 3 \times 10^{15} W/cm^2$. And so, the peak intensity for a 4 cycle, 800 nm laser pulse was chosen to be $I = 4.8 \times 10^{14} W/cm^2$, in line with [45] in the figures above. For full convergence, we required 80 angular momenta and 900 B-splines over a 600 a.u. box. We could not achieve convergence using the parameters described in the argon calculations by Ivanov [45].

For initial state $3p$, $m = 1$ ground state argon subject to a laser pulse in the tunnelling regime, we should expect to see similar behaviour to what we observed in $1s$ hydrogen in figure 5.5 and in [42]. To a large degree, we

do see the same effect on the dampening of the cusp as we move to circular polarisation in argon. The purple line in figure 5.19 displays the cusp at the origin, exactly like in $1s$ hydrogen.

The circular polarisation case of $3p$, $m = 1$ argon, however, has a steeper Gaussian TEMD than that of $1s$ hydrogen subject to circular polarisation. This indicates that the ratio of total ionisation in argon subject to linear polarisation to argon subject circular polarisation is much smaller than the same ratio in $1s$ hydrogen where the linear TEMD dwarfs the circular TEMD. This can be attributed to the fact that the selected peak intensity of the laser in the case of argon is closer to the OBI regime than for $1s$ hydrogen, specifically, a factor of 6 compared to a factor of 22.

We then consider the case of odd parity initial state argon and uncover the hidden features of the TEMDs shown by Ivanov *et al* in figures 5.17 and 5.18 [45]. Figure 5.20 shows the TEMDs for linear and circular polarisation for $3p$, $m = 0$ argon subject to the same laser parameters described above. Both of the TEMDs exhibit an inverted cusp at the origin which was to be expected when we consider figure 5.14b, however, there is a significantly smaller amount of ionisation occurring in the circular polarisation case than in the linear polarisation case. This appears to be symptomatic of interactions within the adiabatic tunnelling regime. When compared to figure 5.13, the TEMDs for odd parity initial state hydrogen in the OBI regime, there is in fact an increase in the ionisation probability as we move from linear to circular polarisation, the opposite to what we find in the tunnelling regime.

Both cases of initial state argon that we consider, when subject to linear polarisation, have the distinctive changes in slope that can be attributed to rescattering, in line with what we see in linear and close to linear polarisation in hydrogen.
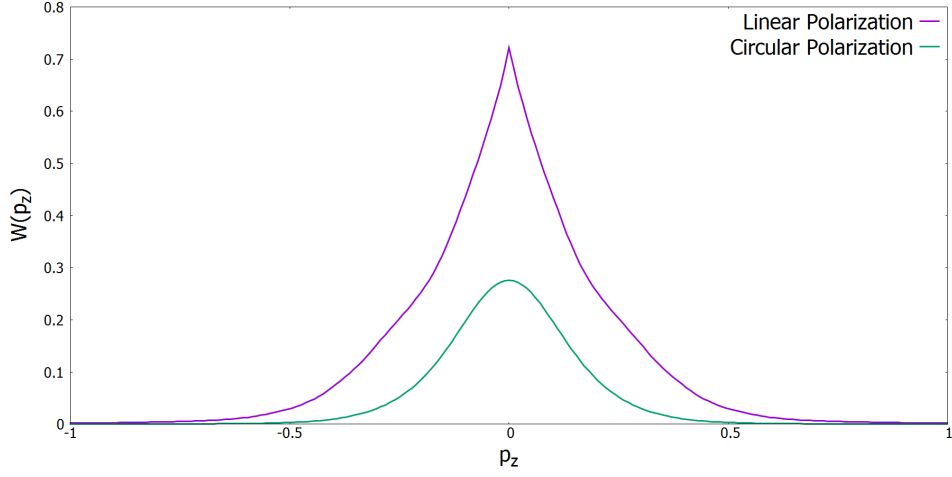
Figure 5.19: The TEMDs of initial state $3p$, $m = 1$ argon after being subjected to a 4 cycle, 800 nm pulse with peak intensity $4.8 \times 10^{14} W/cm^2$. A cusp appears in the linear case (purple line) and a Gaussian is seen in the circular case (green line).
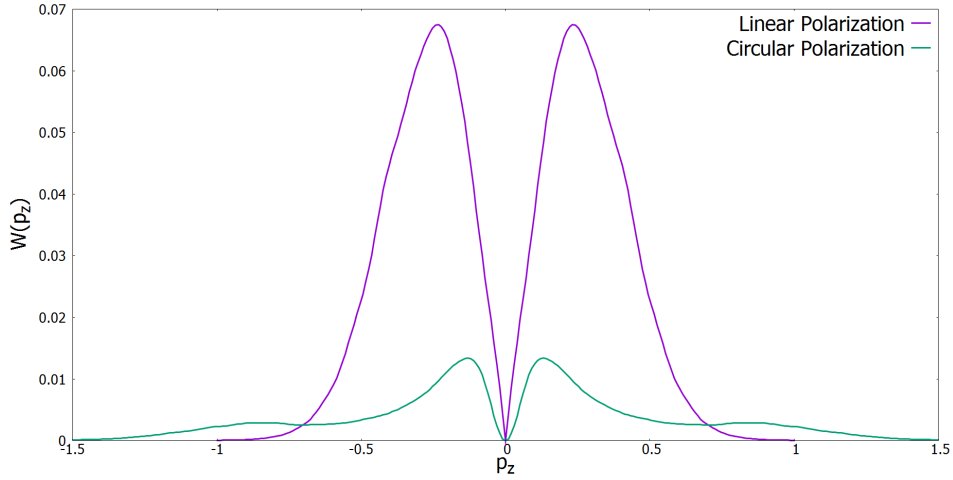
Figure 5.20: The TEMDs of initial state $3p$, $m = 0$ argon after being subjected to a 4 cycle, 800 nm pulse with peak intensity $4.8 \times 10^{14} W/cm^2$. An inverted cusp appears in both linear and circular polarisation.

For $3p$ argon subject to circular polarisation, we see that the distribution of population of the angular momentum number l in the continuum is extremely skewed to the higher end of the spectrum.

We find a significant population of the photoelectrons in the region $l = 40-$ 70 in figures 5.21 and 5.23 and a large spread of m states for the $l = 55 - 70$ in
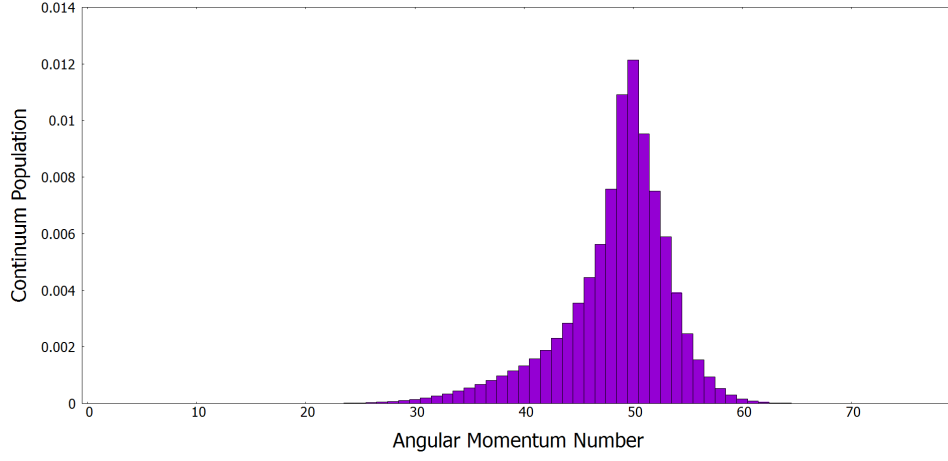
Figure 5.21: The distribution of the angular momentum number population of photoelectrons for $3p$, $m = 1$ argon subject to circularly polarised light.
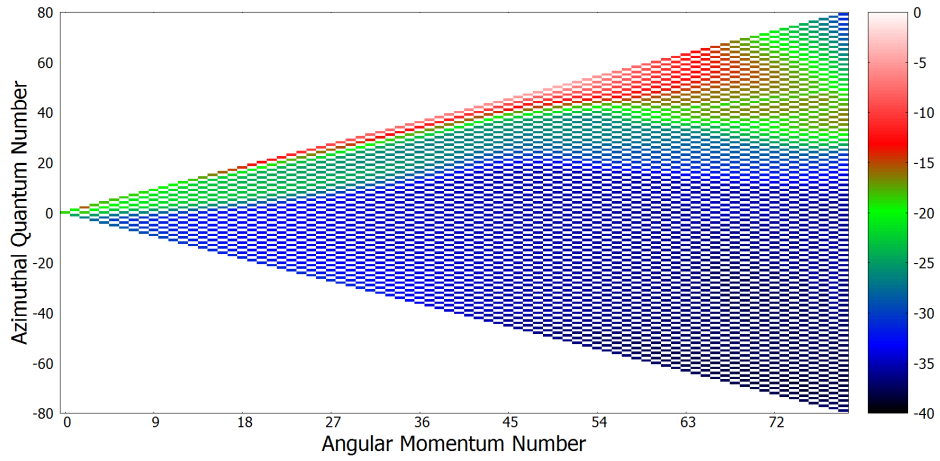
Figure 5.22: The distribution of the (l, m) states of photoelectrons for $3p$, $m = 1$ argon subject to circularly polarised light.

figures 5.22 and 5.24. This describes a different picture to that of $1s$ hydrogen subject to circular light in figure 5.7b, where we observe a very concentrated distribution of m states per l.
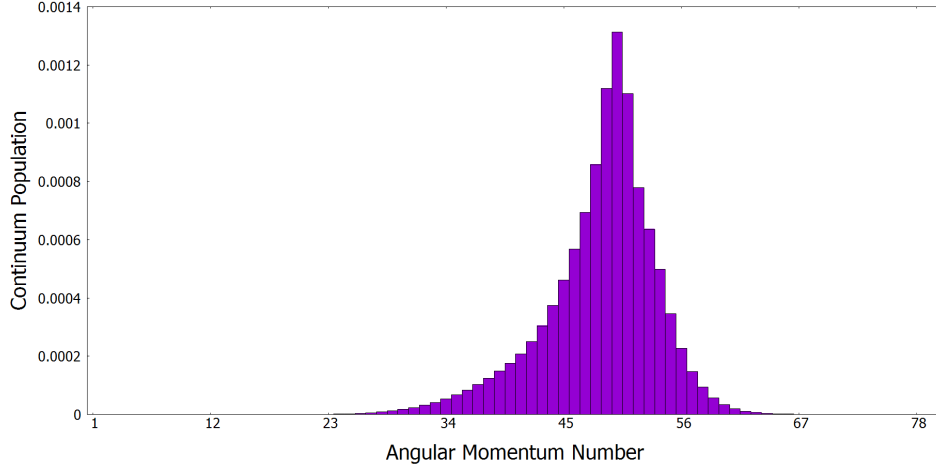
Figure 5.23: The distribution of the angular momentum number population of photoelectrons for $3p$, $m = 0$ argon subject to circularly polarised light.
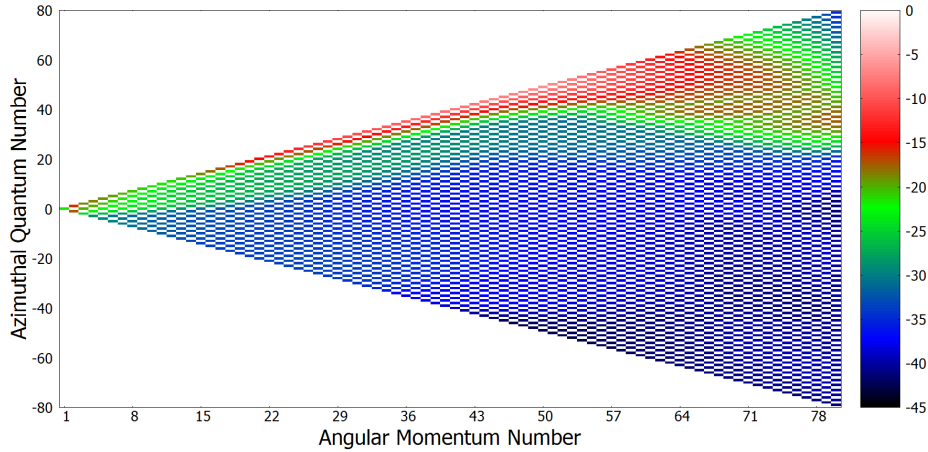
Figure 5.24: The distribution of the (l, m) states of photoelectrons for $3p$, $m = 0$ argon subject to circularly polarised light.

5.6 Conclusion

In the case of linearly polarised light, there was a clear breakdown of the formulae of Delone and Krainov [2] in both hydrogen and argon within the tunnelling regime for system's with even parity initial states which corroborates the findings presented in [72] and [42]. Increasing the ellipticity for even parity initial states, the TEMDs become Gaussian in shape in line with what the SFA without Coulomb correction predicts.

The majority of photoelectrons are to be found in low angular momentum states for systems in the tunnelling regime subject to linearly polarised light and for any ellipticity in the OBI regime. This corroborates with the hypothesis given by Ivanov [42] that when we find a large preponderance of photoelectrons with low angular momenta, the singularity in the Coulomb continuum wave function becomes pronounced in the form of a cusp at the origin of the TEMD. Moving from linear to circular light in the tunnelling regime, we find the distribution of angular momenta shift upward which serves to dull the singularity in the Coulomb continuum wave function and form a Gaussian TEMD.

In all systems that were subject to exactly or nearly linearly polarised light in hydrogen and argon, there was evidence of a change in the slope of the TEMD, highlighting that rescattering occurs independently of whether the initial state has odd or even parity and whether the system lies within the OBI or tunnelling regime.

Ivanov et al [45] presented interesting results in the tunnelling ionisation and OBI regime for metastable neon and argon, respectively. However, they did not separate the initial states by m value. Instead the TEMDs presented by Ivanov *et al* were calculated using a superposition of initial states over the m values for a given l. When analysing the atomic structure in more detail by examining the ionisation from initial states with different magnetic quantum numbers, we found new features for the first time in TEMD calculations. For initial states with odd parity, there was a clear inversion of the cusp-like behaviour and instead we found no zero momentum electrons transverse to the electric field. The transition selection rules for electrons in the cases we considered in this chapter are completely unable to access electronic states that permit zero momenta in the transverse direction, a feature hidden by the

superposition of initial states given in [45]. In order for ionised electrons to access these states from an odd parity initial state, the electric field would require parameters that necessitate non-dipole effects, where different selection rules permit transitions from odd to even parity states.

Chapter 6

Momentum Distributions for Hydrogen Subject to Long Wavelength Intense Fields

6.1 Introduction

Up to now we have focussed on parameter ranges where the dipole approximation is valid. The approximation is sometimes based on the fact that the wavelength of the laser field is very large when compared with the size of the target atom and thus, the vector potential $\mathbf{A}(t)$ is taken to be spatially homogenous. Hence, it is to be expected that this approximation would breakdown as the wavelength of the driving field decreases to the point that it becomes comparable to the size of our atom. However the breakdown of the dipole approximation is also known to occur when the wavelength of a high intensity laser becomes sufficiently long. The parameter range where the dipole approximation is valid is shown in figure 2.1.

Ludwig *et al* [57] have investigated the long wavelength breakdown of the dipole approximation. They state that the limit of the dipole approximation for long wavelength is reached when the magnetic field induced amplitude of a free electron's motion, in the frame where the electron on average is at rest, becomes 1 a.u. or $U_p/2\omega c = 1$. For $1s$ hydrogen subject to an 800 nm pulse,

magnetic field effects would be incurred if the field intensity were to reach $5 \times 10^{15} W/cm^2$. Chelkowski *et al* [19] have performed a grid based TDSE calculation for $1s$ hydrogen to study these non-dipole effects at 800 nm up to $I = 7 \times 10^{14} W/cm^2$, a considerably lower intensity than $5 \times 10^{15} W/cm^2$ given in [57]. The Coulomb potential was replaced by a regularised Coulomb potential and a small shift in momentum along the propagation direction was observed for linearly polarised light [19].

Ludwig *et al* present an experimental study on non-dipole linear polarisation in the mid infra-red range with intensities that breach this limit of $U_p/2\omega c = 1$ a.u. or $I \geq 8\omega^3 c$ alongside simulations performed using classical trajectory Monte Carlo with a semi-classical two step model.
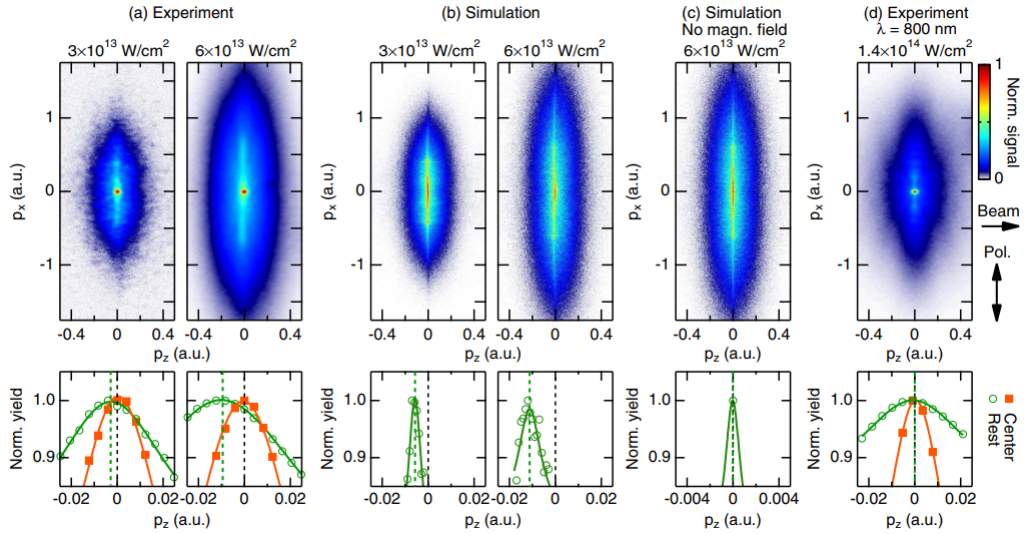
Figure 6.1: The photoelectron momentum distributions measured and calculated by Ludwig *et al* [57] for xenon and helium.

Figure 6.1 shows the breakdown of the dipole approximation in experiment and simulation for laser-atom interactions involving xenon and helium. Panel (a) displays the experimental photoelectron momentum distribution of xenon subject to a $3.4\mu m$ pulse linearly polarised in the x-direction with intensities $3 \times 10^{13} W/cm^2$ and $6 \times 10^{13} W/cm^2$. In the lower panel of (a), the distribution

of momentum along p_z (the propagation direction of the beam and perpendicular to the polarisation plane) is offset. This is also seen to be the case in simulations about $p_z = 0$ in panel (b) and is not manifest when the magnetic component of the field is neglected in panel (c) and when the intensity is too low in panel (d) for helium in an 800 nm laser field.

The offset occurs in the direction opposite to the direction of propagation of the beam. Ludwig *et al* [57] reasoned that this occurs with linear polarisation because the electron is pushed along the propagation direction and is then pulled backwards by the Coulomb potential, towards the parent-ion as it is moved up and down past the ion by the electric field ([53], [22]). The effects of Coulomb focussing are less pronounced for longer wavelength laser fields. Also, in circular polarisation, the effects of the Coulomb field are diminished considerably due to the electron being very unlikely to be involved in recollisions which contributes to the effects of Coulomb focussing in linear polarisation [21]. Experimentally, Smeenk *et al* [80], show that there is a shift in photoelectron momentum along the direction of propagation in circularly polarised light. In a recent paper by Daněk *et al* [26], the dependence between the momentum shift along the propagation direction from positive to negative and the ellipticity of the field is studied experimentally and also theoretically using classical trajectory Monte Carlo simulations.

In this chapter, the TDSE is solved directly for a linearly polarised field including non-dipole terms in the Hamiltonian in order to explore whether these additional dynamics include the effects on the momentum distributions shown in figure 6.1. However, due to the complexity of the resultant TDSE, several approximations are necessary in order to make the calculations possible. Hence the results shown are exploratory in nature.

6.2 Formulation of the Hamiltonian in the Weakly Relativistic Regime

For numerical simulations in which the laser field parameters fall just outside the dipole oasis, specifically near the relativistic break down of the dipole approximation, retardation effects must be considered when formulating the Hamiltonian of the system.

Using a linearly polarised pulse in the x-direction propagating along the z-axis, we define the vector potential of the electromagnetic field as:

$$\mathbf{A}(\mathbf{r}, t) = A(t')\mathbf{e}_x \tag{6.1}$$

where $t' = t - \alpha z$. The Hamiltonian becomes

$$\mathcal{H} = \frac{1}{2}\mathbf{p}^2 + V + A(t')p_x + \frac{1}{2}A^2(t'). \tag{6.2}$$

The TDSE corresponding to this pulse is too expensive computationally, in particular when dealing with the term $A(t')p_x$ and so, Dondera and Bachau introduce the following simple approximation [30] to the potential:

$$A(t - \alpha z) \approx A(t) - \alpha\dot{A}(t)z = A(t) + \alpha F(t)z \tag{6.3}$$

where $F(t) \equiv -\dot{A}(t)$ and $\alpha = 1/c$ is the fine structure constant. Note that this approximation of the potential relies on the parameters of the electromagnetic field and will not produce satisfactory results for frequencies that become to high, specifically for $\alpha\omega > 1$ a.u. or $\omega > 3.73$ keV.

The Hamiltonian in equation (6.2) is now approximated by the following

$$\mathcal{H} \approx \frac{1}{2}\mathbf{p}^2 + V + A(t)p_z + \alpha F(t)zp_x + \alpha A(t)F(t)z, \qquad (6.4)$$

where the term $\frac{1}{2}A^2(t)$ and all terms over and including α^2 have been omitted. We then rewrite equation (6.4) as:

$$\mathcal{H} \approx \mathcal{H}_{at} + \mathcal{H}_{DA} + \mathcal{H}_{RET}^{(1)} + \mathcal{H}_{RET}^{(2)} \equiv \tilde{\mathcal{H}}, \qquad (6.5)$$

where $\mathcal{H}_{at} = \frac{1}{2}\mathbf{p}^2 + V$, $\mathcal{H}_{DA} = A(t)p_x$, $\mathcal{H}_{RET}^{(1)} = \alpha F(t)zp_x$ and $\mathcal{H}_{RET}^{(2)} = \alpha F(t)A(t)z$.

6.2.1 Matrix Elements of the Non-Dipole Part of the Hamiltonian

We represent the wave function in terms of B-spline functions (see equation (3.38)). The Hamiltonian has bandwidth $2k - 1$ where k is the order of the B-spline since for $|i - j| \geq k$ we have

$$\int_0^\infty B_i(r)B_j(r)dr = 0. \qquad (6.6)$$

This is especially desirable for non-dipole calculations because memory is a finite resource and to propagate in the atomic basis, for instance, would significantly reduce the size of the calculation that could be performed as opposed to using the B-spline basis.

$$\left[\mathcal{H}_0\right]_{i,j}^{\substack{l,l\\m,m}} = \frac{-1}{2}\left[\mathcal{B}_{i,j}^{kin}\right] - \frac{l(l+1)}{2}\left[\mathcal{B}_{i,j}^{ang}\right] - \left[\mathcal{B}_{i,j}^{Coul}\right] \qquad (6.7)$$

$$\left[\mathcal{H}_{DA}\right]_{i,j}^{\substack{l-1,l\\m-1,m}} = -iA(t)\sqrt{\frac{(l+m)(l+m-1)}{(2l+1)(2l-1)}}\left[\mathcal{B}_{i,j}^{\partial x}(l)\right], \qquad (6.8)$$

$$\left[\mathcal{H}_{DA}\right]_{i,j}^{\substack{l-1,l\\m+1,m}} = iA(t)\sqrt{\frac{(l-m)(l-m-1)}{(2l+1)(2l-1)}}\left[\mathcal{B}_{i,j}^{\partial x}(l)\right], \qquad (6.9)$$

where

$$\left[\mathcal{B}_{i,j}^{kin}\right] = \left\langle\frac{B_i}{r}\left|\frac{d^2}{dr^2}\right|\frac{B_j}{r}\right\rangle = \int_0^{r_{max}} B_i B_j'' dr, \qquad (6.10)$$

$$\left[\mathcal{B}_{i,j}^{ang}\right] = \left\langle\frac{B_i}{r}\left|\frac{1}{r^2}\right|\frac{B_j}{r}\right\rangle = \int_0^{r_{max}}\frac{B_i B_j}{r^2}dr, \qquad (6.11)$$

$$\left[\mathcal{B}_{i,j}^{Coul}\right] = \left\langle\frac{B_i}{r}\left|\frac{1}{r}\right|\frac{B_j}{r}\right\rangle = \int_0^{r_{max}}\frac{B_i B_j}{r}dr \qquad (6.12)$$

and

$$\left[\mathcal{B}_{i,j}^{\partial x}(k)\right] = \left\langle\frac{B_i}{r}\left|\left|\frac{rB_j' + kB_j}{r^2}\right.\right.\right\rangle = \int_0^{r_{max}} B_i B_j' dr + k\int_0^{r_{max}}\frac{B_i B_j}{r}dr \quad (6.13)$$

which comes from the $\frac{\partial}{\partial x}$ which appears in any part of the Hamiltonian involving $\mathbf{p}$.

$\mathcal{H}_0$ and $\mathcal{H}_{DA}$ are the usual terms for the atomic and interaction parts of the Hamiltonian subject to the dipole approximation. The matrix elements for the extra terms of the Hamiltonian that arise from taking $t' = t - \alpha z$ will be laid out below.

First of all, the matrix elements for the correction $\mathcal{H}_{RET}^{(1)}$ originating from $\mathbf{A}\cdot\mathbf{p}$ in the Hamiltonian are as follows:

$$\left[\mathcal{H}^{(1)}_{RET}\right]^{\substack{l-2,l \\ m-1,m}}_{i,j} = -\frac{i\alpha}{2}F(t)\left[\mathcal{B}^{\partial x,z}_{i,j}(l)\right]$$
$$\times\sqrt{\frac{(l+m)(l+m-1)}{((2l+1)(2l-1)}}\sqrt{\frac{(l+m-2)(l-m)}{(2l-1)(2l-3)}}$$

$$\tag{6.14}$$

$$\left[\mathcal{H}^{(1)}_{RET}\right]^{\substack{l,l \\ m-1,m}}_{i,j} = -\frac{i\alpha}{2}F(t)\left[\mathcal{B}^{\partial x,z}_{i,j}(l)\right]$$
$$\times\sqrt{\frac{(l+m)(l+m-1)}{((2l+1)(2l-1)}}\sqrt{\frac{(l+m-1)(l-m+1)}{(2l+1)(2l-1)}}$$

$$\tag{6.15}$$

$$\left[\mathcal{H}^{(1)}_{RET}\right]^{\substack{l-2,l \\ m+1,m}}_{i,j} = \frac{i\alpha}{2}F(t)\left[\mathcal{B}^{\partial x,z}_{i,j}(l)\right]$$
$$\times\sqrt{\frac{(l-m)(l-m-1)}{(2l+1)(2l-1)}}\sqrt{\frac{(l+m)(l-m-2)}{(2l-1)(2l-3)}}$$

$$\tag{6.16}$$

$$\left[\mathcal{H}^{(1)}_{RET}\right]^{\substack{l,l \\ m+1,m}}_{i,j} = \frac{i\alpha}{2}F(t)\left[\mathcal{B}^{\partial x,z}_{i,j}(l)\right]$$
$$\times\sqrt{\frac{(l-m)(l-m-1)}{((2l+1)(2l-1)}}\sqrt{\frac{(l+m+1)(l-m-1)}{(2l+1)(2l-1)}}$$

$$\tag{6.17}$$

where

$$\left[\mathcal{B}^{\partial x,z}_{i,j}(k)\right] = \left\langle \frac{B_i}{r} \middle| r \middle| \frac{rB'_j + kB_j}{r^2} \right\rangle = \int_0^{r_{max}} B_i B'_j r dr + k\int_0^{r_{max}} B_i B_j dr.$$

$$\tag{6.18}$$

The second non-dipole correction, $\mathcal{H}^{(2)}_{RET}$, due to the $\frac{1}{2}\mathbf{A}^2$ term in the velocity
gauge, is:

$$\left[\mathcal{H}^{(2)}_{RET}\right]^{\substack{l-1,l \\ m,m}}_{i,j} = \alpha F(t)A(t)\left[\mathcal{B}^r_{i,j}\right]\sqrt{\frac{(l+m)(l+m-1)}{(2l+1)(2l-1)}}.$$

$$\tag{6.19}$$

There is one more piece of notation left to clear up:

$$\left[\mathcal{B}_{i,j}^r\right] = \left\langle \frac{B_i}{r} \left| r \right| \frac{B_j}{r} \right\rangle = \int_0^{r_{max}} B_i B_j r dr. \tag{6.20}$$

6.3 Ionisation by Long Wavelength Lasers

The formula that determines when non-dipole effects from the magnetic component $\mathbf{v} \times \mathbf{B}$ arise comes from considering the figure '8' motion of a free charged particle in a plane wave field in figure 6.2. At low intensity, the particle follows a straight line of amplitude α_0 through interaction with a linearly polarised electric field. If the amplitude in the direction of propagation of the plane wave field reaches 1 a.u. then the dipole approximation is no longer valid. This occurs at

$$\beta_0 = \frac{U_p}{2\omega c} = 1 \text{ a.u.} \tag{6.21}$$

which, when rearranged, gives

$$I = 8\omega^3 c. \tag{6.22}$$

Thus, by fixing the intensity and increasing the wavelength of the field sufficiently, non-dipole effects from the magnetic field component along the propagation direction will arise.

6.3.1 Envelope Approximation

We first drop the term pertaining to the second order contribution from $\mathbf{A} \cdot \mathbf{p}$, $\mathcal{H}_{RET}^{(1)}$, since it has been shown to be dominated by $\mathcal{H}_{RET}^{(2)}$ [34].
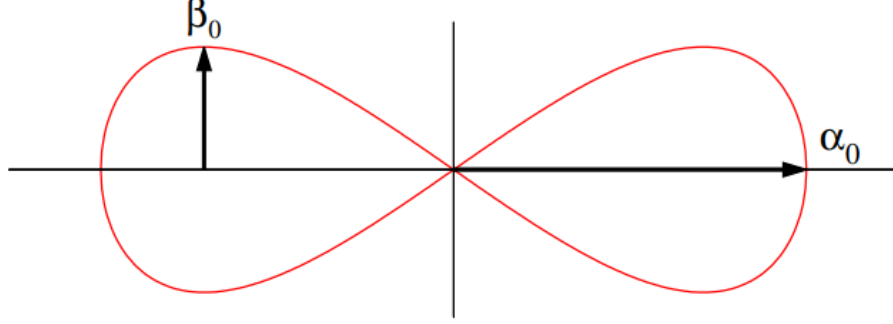
Figure 6.2: A free electron's motion in a plane wave field traces out a figure of 8 in a frame of reference where the electron is at rest on average. The amplitude α_0 is in the direction of the electric, while the amplitude β_0 is the motion in the direction of propagation of the plane wave field [54]. When β_0 reaches 1 a.u. then the long wavelength failure of the dipole approximation may occur (figure taken from [71]).

Special consideration is given in this section of the Hamiltonian to terms relating to two-photon transitions given in equation (6.19) when striking an electron with a laser with a long wavelength and with intensities that would place it within the non-dipole regime. The term involves the product of $F(t)A(t)$, meaning it oscillates at twice the rate of the other terms in the Hamiltonian. It was quickly realised that leaving this term in the form it is given in the equations referenced above, requires extremely small time steps. In order to remedy this problem, it was necessary to employ what it is known as the *envelope approximation* to this term [79].

It is argued in a paper by Simonsen *et al* [79] that one can use a time average of the induced motion along the motion of propagation to approximate the non-dipole contributions to a high degree within the context of high intensity and high frequency lasers. Thus, it is interesting to investigate the effectiveness of this approximation within the context of high intensity, low frequency lasers.

Starting with the reduced Hamiltonian from in equation (6.4)

$$\mathcal{H} = \mathcal{H}_{at} + \mathcal{H}_{DA} - \alpha z A(t) A'(t) \tag{6.23}$$

where $F(t) = -A'(t)$, Simonsen *et al* first convert to what is known as the *propagation gauge* [33] which is achieved by performing a series of unitary gauge transformations of the form

$$\Psi_n = U_n \Psi_{n-1} = e^{i\alpha_n} \Psi_{n-1} \tag{6.24}$$

where

$$\alpha_n(\omega t - \mathbf{k} \cdot \mathbf{r}) = a_n \frac{c^2}{\omega} \int_{-\infty}^{\omega t - \mathbf{k} \cdot \mathbf{r}} \left(\frac{-A(\eta)}{c} \right)^{2n} d\eta \tag{6.25}$$

with the a_n real transformation weights given by

$$a_n = \sum_{i=1}^{n-1} a_i a_{n-i} = \binom{2n}{n} \frac{1}{4^n(2n-1)}. \tag{6.26}$$

Each gauge transformation is then defined recursively as

$$\mathcal{H}_n = U_n \mathcal{H}_{n-1} U_n^\dagger + i \dot{U}_n U_n^\dagger \tag{6.27}$$

however, for the purposes of the approximation defined in [79], it is only necessary to take the first order transformation of the propagation gauge.

With the Hamiltonian defined as it is in equation (6.23), Simonsen *et al* take

$$U = \exp\left(-i\frac{\alpha}{2} z A^2(t) \right) \tag{6.28}$$

resulting in the new Hamiltonian

$$\mathcal{H}_{PG} = U\mathcal{H}U^\dagger + i\dot{U}U^\dagger$$
$$= \mathcal{H}_{at} + A(t)p_x + \frac{\alpha}{2}A^2(t)p_z \tag{6.29}$$

where

$$A(t) = A_0 \sin(\omega t + \phi)f^2(t) \tag{6.30}$$

$$f(t) = \sin^2\left(\frac{\pi t}{\tau}\right) \tag{6.31}$$

for $0 < t < 2N\pi/\omega = \tau$.

The first interaction is simply the dipole interaction term in the velocity gauge, while the other interaction term describes a non-negative force in the direction of propagation which mimics a non-zero displacement pulse [44]. This field in this term, $A^2(t)$ can be rewritten as

$$A^2(t) = \frac{1}{2}A_0^2 f^2(t)(1 - \cos(2(\omega t + \phi)))$$
$$= \frac{1}{2}A_0^2[f^2(t) - f^2(t)\cos(2(\omega t + \phi))] \tag{6.32}$$

so that when this is substituted back into the Hamiltonian given by equation (6.29), it becomes:

$$\mathcal{H}_{PG} = \mathcal{H}_{at} + A(t)p_x$$
$$+ \frac{\alpha}{4}A_0^2 f^2(t)p_z \tag{6.33}$$
$$- \frac{\alpha}{4}A_0^2 f^2(t)\cos(2(\omega t + \phi))p_z.$$

The principle idea behind the envelope approximation is that one can neglect the second non-dipole term in the propagation gauge Hamiltonian. This can be justified because the first term involving just the envelope function $f(t)$ imparts a net momentum transfer to the particle in the direction of propagation, while the other non-dipole term oscillates quickly about this mean net transfer. Since these oscillations are superimposed on a net shift over a comparatively slow time scale, their contribution is expected to vanish. This is true when $f^2(t)$ varies slowly compared to π/ω [79].

When disregarding this term, the envelope approximation in the propagation gauge is

$$\mathcal{H}_{PG}^{env} = \mathcal{H}_{at} + A(t)p_x + \frac{\alpha}{4}A_0^2 f^2(t)p_z. \qquad (6.34)$$

Moving back to the velocity gauge by applying the inverse operation subject to the envelope approximation

$$\Psi = \exp\left(i\frac{\alpha A_0^2}{4}zf^2(t)\right)\Psi_{PG} \qquad (6.35)$$

leaves the envelope approximated velocity gauge Hamiltonian as

$$\mathcal{H}_{env} = \mathcal{H}_{at} + \mathcal{H}_{DA} - \frac{\alpha}{2}A_0^2 zf(t)f'(t). \qquad (6.36)$$

The approximation constitutes a time averaging over the carrier wave in the non-dipole operator [79].

6.4 Non-Dipole Results

In this section, for computational simplicity, the pulse is defined with a cosine squared envelope rather than sine squared

$$A(t) = A_0 \sin(\omega t + \phi) \cos^2\left(\frac{\omega t}{2N}\right) \qquad -\frac{N\pi}{\omega} < t < \frac{N\pi}{\omega} \qquad (6.37)$$

where N is the number of cycles of the pulse. Since the envelope has changed, the time dependent factor in the final summand of equation (6.36) becomes

$$f(t)f'(t) = -\frac{2\pi}{\tau} \cos^3\left(\frac{\pi t}{\tau}\right) \sin\left(\frac{\pi t}{\tau}\right). \qquad (6.38)$$

We begin by calculating the momentum along the propagation direction for the example given in [57], however, we use hydrogen instead of helium (see figure 6.1 panel (d)). We subject ground state hydrogen to an 800 nm, 2 cycle linearly polarised laser with intensity $1.4 \times 10^{14} W/cm^2$ with and without the non-dipole term in equation (6.36). The parameters for this calculation are relatively manageable given the intensity: $l_{max} = 32$, $r_{max} = 350$ a.u., $\delta t = 0.05$ a.u. and 350 B-splines. The parameters were varied to test for convergence. Ostensibly, a calculation involving only 33 total angular momenta is relatively small, however, the inclusion of non-dipole components in the Hamiltonian necessitates all (l, m) pairs to be considered. The total number of (l, m) pairs for this calculation is $33^2 = 1089$.

Figure 6.3 displays the momentum of photoelectrons along the propagation axis (the z-axis). These are calculated as described in subsection 5.3.3 of the previous chapter. We see there is a tiny shift in momentum towards negative z, that is $p_z < 0$, but the peak of the momentum distribution is still found at $p_z = 0$.

We attempted to obtain converged results for intensities that would see a clear indication of non-dipole effects at 800 nm, however, with large intensity comes large photoelectron energies. This means that the number of B-splines
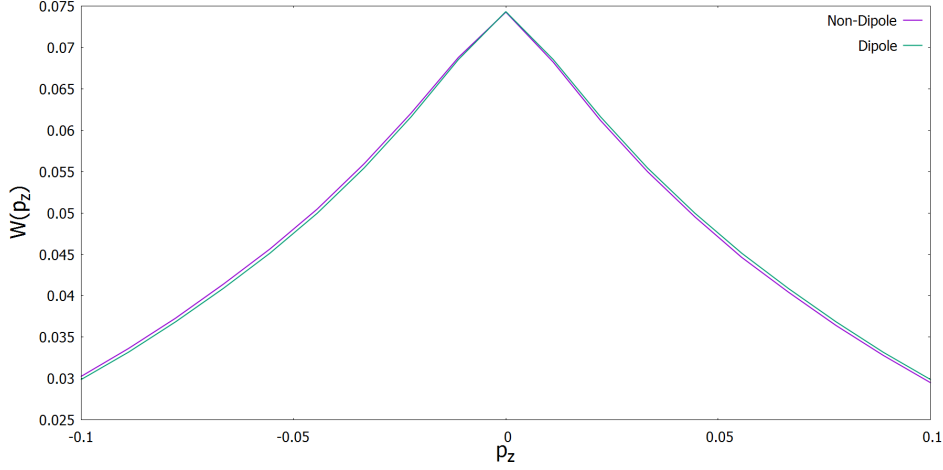
Figure 6.3: A comparison of the momentum distribution along z of $1s$ hydrogen with the dipole approximation in place and with the effect of the addition of non-dipole components. The pulse was linearly polarised with intensity $I = 1.4 \times 10^{14} W/cm^2$ with $\omega = 0.0569$ a.u. and lasted for 2 cycles.

required to represent a calculation at 800 nm becomes unrealistic. To address this issue, we reduce the intensity to $5 \times 10^{13} W/cm^2$ and increase the wavelength of the pulse to 2.5 microns. A reduction in intensity brings with it a reduction in the number of high energy ionisation events. The B-spline basis of size N can faithfully reproduce energies up to [6]

$$E_N = \frac{N^2 \pi^2}{2r_{max}^2}.$$ (6.39)

If we reduce the window of energies we expect photoelectrons to have for a given calculation, we can reduce the number of B-splines dramatically.

With this in mind, the parameters required for convergence for a 2.5 micron laser for 2 cycles with intensity $5 \times 10^{13} W/cm^2$ are $l_{max} = 80$, $\delta t = 0.025$ a.u., $r_{max} = 1000$ a.u. and 1000 B-splines. To emphasise the size of a calculation like this, the total number of (l, m) pairs in this calculation is $81^2 = 6561$. Again, these parameters were tested for convergence.

Figure 6.4 displays a comparison between the TEMD for the dipole ap-
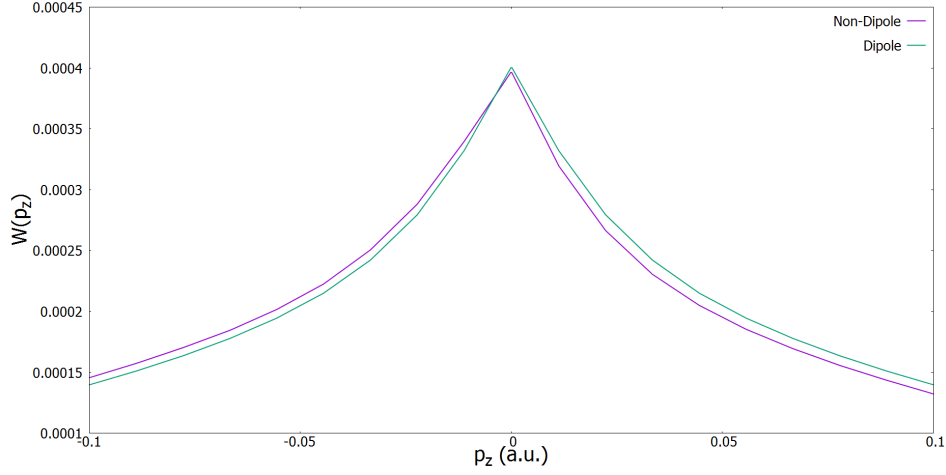
Figure 6.4: A comparison between the TEMD with the dipole approximation in place and the TEMD with the non-dipole envelope approximation. Ground state hydrogen was subject to a linearly polarised 2 cycle pulse of wavelength 2500 nm and intensity $5 \times 10^{13}W/cm^2$.

proximation and the TEMD which pertains to the addition of the non-dipole envelope approximation component to the Hamiltonian. The TEMD for the dipole approximation is symmetric about the origin $p_z = 0$, while the TEMD for the non-dipole calculation is skewed quite clearly towards $p_z < 0$. This corroborates the findings by Ludwig *et al* [57] for xenon at $3 \times 10^{13}W/cm^2$ and $6 \times 10^{13}W/cm^2$ but for 3.4 microns. Interestingly, the experimental results by Ludwig *et al* [57] and the results shown in figure 6.4 exhibit non-dipole effects below the point at which we should expect them to occur according to Reiss [71]. For 3.4 microns, non-dipole effects are predicted to occur at $I = 9 \times 10^{13}W/cm^2$ and for 2.5 microns, non-dipole effects are predicted to occur at $I = 2.3 \times 10^{14}W/cm^2$. In experiment and through the direct solution of the TDSE, non-dipole effects become manifest between at intensities $2 - 3$ times lower than what is predicted.

Panel (a) in figure 6.1 displays the transverse momentum distribution for photoelectrons for the aforementioned laser parameters. There is a small offset, for both intensities considered, towards $p_z < 0$, against the direction of
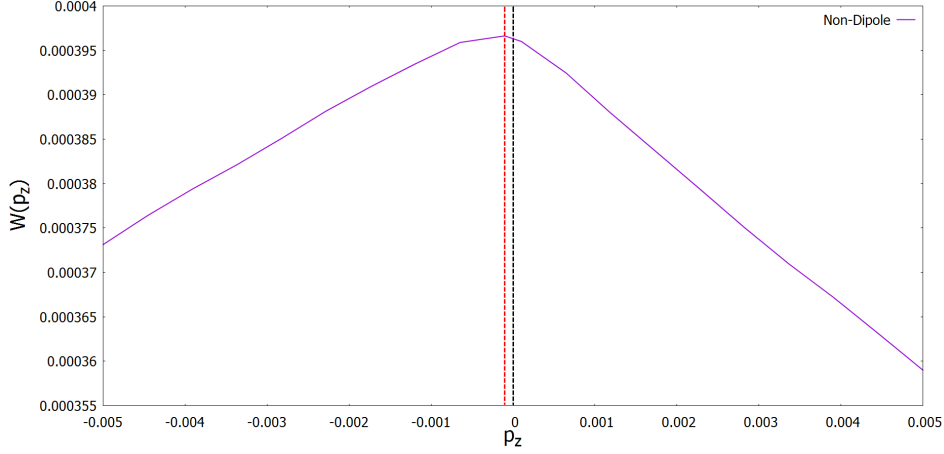
Figure 6.5: A closer look at the TEMD for $1s$ hydrogen subject to a 2 cycle, 2.5 micron linearly polarised pulse with intensity $5 \times 10^{13} W/cm^2$. The black dashed line corresponds to the origin, the red line corresponds to the maximum calculated point of the TEMD.

propagation. Figure 6.5 shows the same small offset against the direction of propagation for the direct solution of the TDSE of ground state hydrogen. The black line corresponds to the origin, the point at which, within the dipole approximation, the TEMD should be symmetric. The red line shows where the TEMD is actually at a maximum according to our calculations - a tiny offset against the direction of propagation, corroborating the results in [57] and accentuating the photoelectron's interaction with the core at the end of the pulse.

We note, that in figure 6.4 the TEMD for the dipole approximation boasts a slightly higher peak. This seems to come from a very minute difference in the cross section at low energy (see figure 6.6). The non-dipole cross section falls slightly under the dipole for low energy, however, beyond this point both cross sections are equal - even in log scale.
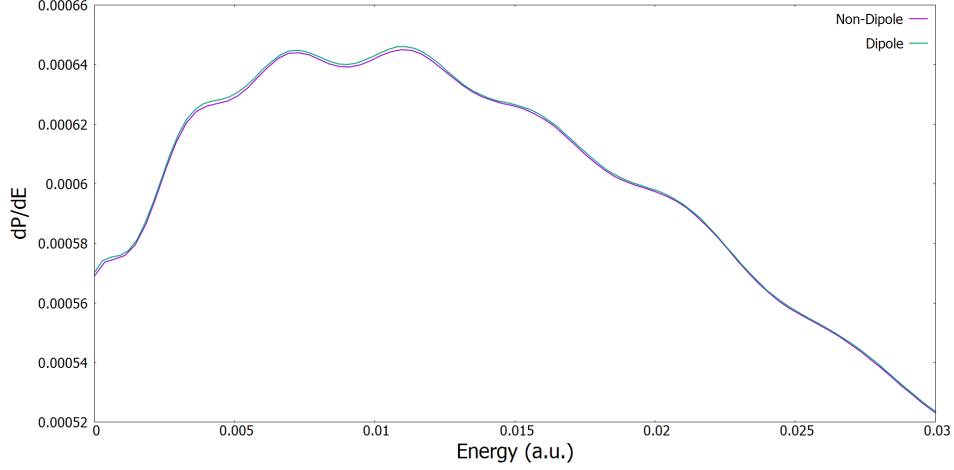
Figure 6.6: The low energy region of the distribution of photoelectron energies for both the dipole and non-dipole calculation in $1s$ hydrogen subject to a 2 cycle 2.5 micron linearly polarised laser with intensity $I = 5 \times 10^{13} W/cm^2$.

6.5 Conclusion

We decided to focus on long wavelength laser-atom interactions in linear polarisation with moderate intensity to compare with the experimental results by Ludwig *et al* [57] which showed that there is a shift in the momentum distribution of photoelectrons against the propagation direction of the laser. With the inclusion of the non-dipole envelope approximation component to the Hamiltonian, we found good agreement with their results. Figure 6.4 shows that for $1s$ hydrogen subject to a 2 cycle, $2.5\mu m$ linearly polarised laser with intensity $5 \times 10^{13} W/cm^2$ that there is a significant tilt in photoelectron momentum against the propagation direction of the laser. A shift in the peak of the momentum distribution along p_z was found in figure 6.5, corroborating the findings of Ludwig *et al* [57] that the Coulomb potential influences the motion of the photoelectron after the pulse.

Figure 6.3 showed a small tilt towards $p_z < 0$ for $1s$ hydrogen subject to a 2 cycle 800 nm linearly polarised pulse with intensity $1.4 \times 10^{14} W/cm^2$. This comes from the fact that the envelope approximation is always non-zero no

matter the parameters of the laser field and will affect the observables at the end of the pulse, even if the effect is very slight. No shift in the peak of the momentum distribution in p_z was observed which is in good agreement with the rightmost panel of figure 6.1.

It is important to note that these results are exploratory and that the envelope approximation permitted these calculations due to the impact it has on the size of the time step we could choose. It would be interesting to use the full non-dipole Hamiltonian in equation (6.2) to investigate the results in this chapter with and without the envelope approximation. Through tests with the full Hamiltonian, we have found the time step required becomes very small since the term $A(t)F(t)$ in equations (6.19) and (6.19) oscillates twice as fast the dipole term and the term $F(t)$ in equations (6.14) to (6.17) oscillates out of phase with the dipole term.

Chapter 7

Conclusion and Outlook

In this thesis we examined a number of effects arising with atoms in intense laser fields. We presented a comparison between the PPT theory of Barth and Smirnova [10], [9] and our direct numerical integration of the TDSE to explore the preferential ionisation of counter-rotating electrons over co-rotating electrons relative to a circularly polarised field, the so-called propensity rule. We found qualitative agreement with the results of Barth and Smirnova for the non-adiabatic tunnelling regime where $E_0 < E_{BSI}$ and $\gamma \approx 1$, [51], in particular when they added long-range Coulomb corrections to their theory [51]. However, outside of this parameter region, we found that their theory did not agree with the TDSE results and that in some cases, the propensity rule broke down. There was a reversal in the propensity rule for certain values of ω and we anticipate that the co-rotating case will continue to be preferentially ionised for $\omega > 0.3$ (the highest value of ω to be used). We also observed a large degree of excitation in the counter-rotating case, accompanied by highly oscillatory behaviour with respect to increasing frequency of the laser field. The co-rotating case only saw significant excitation at the high end of the range of frequencies we considered.

We evaluated the electron momentum distribution for hydrogen and argon for linear and elliptically polarised fields in various parameter regimes. Focussing on the transverse electron momentum distribution (TEMD) in the tunnelling and BSI regimes we found that that the SFA without Coulomb

correction is not sufficient to describe electron dynamics when significant interaction with the ion-core is present during the pulse. For linearly polarised fields within the tunnelling regime a cusp-like shape appears at the origin while the SFA without Coulomb correction predicts a smooth Gaussian TEMD. In addition, a shoulder in the TEMD indicates that rescattering and the Coulomb potential play a crucial role. We find such shoulders in the computed TEMDs for ellipticity up to $\epsilon = 0.25$. The cusp is seen for cases within the tunnelling regime up for $\epsilon = 0.5$ in hydrogen and is observed in ground state argon for linear light. The cusp transforms into a Gaussian as the ellipticity increases towards circular polarisation. For the case of odd parity $l + m$ initial state atoms, we showed that the cusp in the TEMD is inverted. For TEMDs produced from odd parity initial states, this inversion of the cusp at the origin is independent of ionisation regime since it is manifest in $2p$ hydrogen in the BSI regime and is also present in the tunnelling regime for ground state argon. Within the BSI regime for $2p$ hydrogen we see a cusp at the origin for all ellipticities. This means that the SFA without Coulomb correction is not applicable to the transverse momentum dynamics of laser-atom interactions in this regime.

We have performed exploratory calculations in the non-dipole regime for the TEMD for hydrogen. The parameters required for convergence for low frequency, high intensity pulses are very computationally expensive. Ground state hydrogen subject to an 800 nm pulse with intensity above $10^{15} W/cm^2$ requires upwards of 100 angular momenta and very large box sizes. We made some reasonable approximations to the non-dipole terms in the TDSE, including the envelope approximation, and our calculated TEMD shows an asymmetry in the distribution about the origin, agreeing with recent experiments.

We propose some future directions for the work contained in this thesis.

For the propensity rule, it would be interesting to make a direct quantitative comparison with the work of Barth and Smirnova. This would require using longer flat top pulses to calculate the ionisation rate over a cycle. In the non-dipole case, it would be interesting to investigate the accuracy of the envelope approximation and other approximations we used by calculating the TEMD without approximations to the TDSE. This would require significant computational resources but should be feasible. Finally, an interesting question to answer would be how much the inverted cusp in the TEMD is affected when non-dipole components are considered. Non-dipole components would allow odd parity initial states to access even parity states and $p_z = 0$ should, in theory, be possible for electrons subject to such pulses.

Bibliography

[1] P. Agostini et al. "Free-free transitions following six-photon ionization of xenon atoms". *Physical Review Letters* 42, 1127 (1979).

[2] M. V. Ammosov, N. B. Delone, and V. P. Krainov. "Tunnel ionization of complex atoms and atomic ions in a varying electromagnetic-field". *Sov. Phys. JETP* 64, 1191 (1986).

[3] L. Arissian et al. "Direct test of laser tunneling with electron momentum imaging". *Physical Review Letters* 105, 133002 (2010).

[4] S. Augst et al. "Tunneling ionization of noble gases in a high-intensity laser field". *Physical Review Letters* 63, 2212 (1989).

[5] H. Bachau, M. Dondera, and V. Florescu. "Stimulated Compton Scattering in Two-Color Ionization of Hydrogen with keV Electromagnetic Fields". *Physical Review Letters* 112, 073001 (2014).

[6] H. Bachau et al. "Applications of B-splines in atomic and molecular physics". *Reports on Progress in Physics* 64, 1815 (2001).

[7] E. Bank and M. E. H. Ismail. "The attractive Coulomb potential polynomials". *Constructive Approximation* 1, 1 (1985).

[8] I. Barth and M. Lein. "Numerical verification of the theory of nonadiabatic tunnel ionization in strong circularly polarized laser fields". *Journal of Physics B: Atomic, Molecular and Optical Physics* 47, 204016 (2014).

[9] I. Barth and O. Smirnova. "Nonadiabatic tunneling in circularly polarized laser fields. II. Derivation of formulas". *Physical Review A* 87, 013433 (2013).

[10] I. Barth and O. Smirnova. "Nonadiabatic tunneling in circularly polarized laser fields: Physical picture and calculations". *Physical Review A* 84, 063415 (2011).

[11] D. Bauer, D. B. Milošević, and W. Becker. "Strong-field approximation for intense-laser–atom processes: The choice of gauge". *Physical Review A* 72, 023415 (2005).

[12] J. H. Bauer. *Physical Review A* 83, 035402 (2011).

[13] J. H. Bauer et al. "Ionization and excitation of the excited hydrogen atom in strong circularly polarized laser fields". *Physical Review A* 90, 063402 (2014).

[14] H. A. Bethe and E. E. Salpeter. *Quantum mechanics of one-and two-electron atoms*. Springer Science & Business Media, (2012).

[15] C. Z. Bisgaard and L. B. Madsen. "Tunneling ionization of atoms". *American Journal of Physics* 72, 2 (2004).

[16] T. Brabec, M. Y. Ivanov, and P. B. Corkum. "Coulomb focusing in intense field atomic processes". *Physical Review A* 54, R2551 (1996).

[17] J. Burgdörfer. "Inverted cusps in electron spectra near zero velocity in an attractive Coulomb field". *Physical Review Letters* 51, 374 (1983).

[18] J. Burgdörfer et al. "Calculation of electron-loss-to-continuum cusps: An algebraic approach". *Physical Review A* 28, 3277 (1983).

[19]   S. Chelkowski, A. D. Bandrauk, and P. B. Corkum. "Photon-momentum transfer in photoionization: From few photons to many". *Physical Review A* 95, 053402 (2017).

[20]   H. S. Cohl. "On a generalization of the generating function for Gegenbauer polynomials". *Integral Transforms and Special Functions* 24, 10 (2013).

[21]   D. Comtois et al. "Observation of Coulomb focusing in tunnelling ionization of noble gases". *Journal of Physics B: Atomic, Molecular and Optical Physics* 38, 1923 (2005).

[22]   P. B. Corkum. "Plasma perspective on strong field multiphoton ionization". *Physical Review Letters* 71, 1994 (1993).

[23]   E. Cormier and P. Lambropoulos. "Optimal gauge and gauge invariance in non-perturbative time-dependent calculation of above-threshold ionization". *Journal of Physics B: Atomic, Molecular and Optical Physics* 29, 1667 (1996).

[24]   J. Crank and P. Nicolson. "A practical method for numerical evaluation of solutions of partial differential equations of the heat-conduction type". *Mathematical Proceedings of the Cambridge Philosophical Society.* 43, 01. Cambridge Univ Press, (1947).

[25]   E. K. Damon and R. G. Tomlinson. "Observation of ionization of gases by a ruby laser". *Applied Optics* 2, 5 (1963).

[26]   J. Daněk et al. "Interplay between Coulomb-focusing and non-dipole effects in strong-field ionization with elliptical polarization". *Journal of Physics B: Atomic, Molecular and Optical Physics* 51, 114001 (2018).

[27]   C. De Boor. *A practical guide to splines. Number 27 in Applied Mathematical Sciences.* (1978).

[28]   V. L. B. De Jesus et al. "Reaction microscopes applied to study atomic and molecular fragmentation in intense laser fields: non-sequential double ionization of helium". *Journal of electron spectroscopy and related phenomena* 141, 2-3 (2004).

[29]   N. B. Delone and V. P. Krainov. "Energy and angular electron spectra for the tunnel ionization of atoms by strong low-frequency radiation". *JOSA B* 8, 6 (1991).

[30]   M. Dondera and H. Bachau. "Exploring above-threshold ionization of hydrogen in an intense x-ray laser field through nonperturbative calculations". *Physical Review A* 85, 013423 (2012).

[31]   J. H. Eberly, J. Javanainen, and K. Rzazewski. "Above-threshold ionization". *Physics Reports* 204, 5 (1991).

[32]   R. Fletcher. "Conjugate gradient methods for indefinite systems". *Numerical analysis* (1976).

[33]   M. Førre and A. S. Simonsen. "Generalized velocity-gauge form of the light-matter interaction Hamiltonian beyond the dipole approximation". *Physical Review A* 93, 013423 (2016).

[34]   M. Førre and A. S. Simonsen. "Nondipole ionization dynamics in atoms induced by intense xuv laser fields". *Physical Review A* 90, 053411 (2014).

[35]   M. Gajda, B. Piraux, and K. Rzazewski. "Ionization of an excited hydrogen atom by a high-frequency circularly polarized pulsed field". *Physical Review A* 50, 2528 (1994).

[36]   A. Galstyan et al. "Modelling laser-atom interactions in the strong field regime". *The European Physical Journal D* 71, 97 (2017).

[37]   A. Goldberg, H. M. Schey, and J. L. Schwartz. "Computer-generated motion pictures of one-dimensional quantum-mechanical transmission and reflection phenomena". *American Journal of Physics* 35, 3 (1967).

[38]   M. Göppert-Mayer. "Über elementarakte mit zwei quantensprüngen". *Annalen der Physik* 401, 3 (1931).

[39]   I. S. Gradshteyn and I. M. Ryzhik. *Table of integrals, series, and products*. Academic press, (2014).

[40]   T. Herath et al. "Strong-field ionization rate depends on the sign of the magnetic quantum number". *Physical Review Letters* 109, 043004 (2012).

[41]   E. Huens et al. "Numerical studies of the dynamics of multiphoton processes with arbitrary field polarization: Methodological considerations". *Physical Review A* 55, 2132 (1997).

[42]   I. A. Ivanov. "Evolution of the transverse photoelectron-momentum distribution for atomic ionization driven by a laser pulse with varying ellipticity". *Physical Review A* 90, 013418 (2014).

[43]   I. A. Ivanov. "Origin of the cusp in the transverse momentum distribution for the process of strong-field ionization". *Physical Review A* 92, 063417 (2015).

[44]   I. A. Ivanov et al. "Displacement effect in strong-field atomic ionization by an XUV pulse". *Physical Review A* 90, 043401 (2014).

[45]   I. A. Ivanov et al. "Transverse electron momentum distribution in tunneling and over the barrier ionization by laser pulses with varying ellipticity". *Scientific Reports* 6 (2016).

[46]   C. J. Joachain, N. J. Kylstra, and R. M. Potvliege. *Atoms in intense laser fields*. Cambridge University Press, (2012).

[47] W. Kaiser and C. G. B. Garrett. "Two-photon excitation in Ca F 2: Eu 2+". *Physical Review Letters* 7, 229 (1961).

[48] J. Kaushal and O. Smirnova. "Looking inside the tunnelling barrier: I. Strong field ionisation from orbitals with high angular momentum in circularly polarised fields". *Journal of Physics B: Atomic, Molecular and Optical Physics* 51, 174001 (2018).

[49] J. Kaushal and O. Smirnova. "Looking inside the tunnelling barrier: II. Co-and counter-rotating electrons at the tunnelling exit". *Journal of Physics B: Atomic, Molecular and Optical Physics* 51, 174002 (2018).

[50] J. Kaushal and O. Smirnova. "Looking inside the tunnelling barrier III: spin polarisation in strong field ionisation from orbitals with high angular momentum". *Journal of Physics B: Atomic, Molecular and Optical Physics* 51, 174003 (2018).

[51] J. Kaushal and O. Smirnova. "Nonadiabatic Coulomb effects in strong-field ionization in circularly polarized laser fields". *Physical Review A* 88, 013421 (2013).

[52] L. V. Keldysh et al. "Ionization in the field of a strong electromagnetic wave". *Sov. Phys. JETP* 20, 1307 (1965).

[53] K. C. Kulander, K. J. Schafer, and J. L. Krause. *Proceedings of the Workshop on Super Intense Laser Atom Physics (SILAP III)*. 1993.

[54] L. D. Landau and E. M. Lifshitz. *The classical theory of fields*. Pergamon, (1971).

[55] M. Levy. "Wave equations in momentum space". *Proc. R. Soc. Lond. A* 204, 1077 (1950).

[56] K. Liu and I. Barth. "Nonadiabatic tunnel ionization of current-carrying orbitals of prealigned linear molecules in strong circularly polarized laser fields". *Physical Review A* 94, 043402 (2016).

[57] A. Ludwig et al. "Breakdown of the dipole approximation in strong-field ionization". *Physical Review Letters* 113, 243001 (2014).

[58] T. Maiman et al. "Stimulated optical radiation in ruby" (1960).

[59] D. B. Milošević et al. "Above-threshold ionization by few-cycle pulses". *Journal of Physics B: Atomic, Molecular and Optical Physics* 39, R203 (2006).

[60] C. E. Moore. "Atomic Energy Levels, Natl. Bur. Stand. Ref. Data Ser., Natl. Bur. Stand.(US) Circ. No. 35" (1971).

[61] R. Moshammer et al. "Rescattering of Ultralow-Energy Electrons for Single Ionization of Ne in the Tunneling Regime". *Physical Review Letters* 91, 113002 (2003).

[62] H. G. Muller. "Numerical simulation of high-order above-threshold-ionization enhancement in argon". *Physical Review A* 60, 1341 (1999).

[63] A. Ossicini. "Funzione generatrice dei prodotti di due polinomi ultrasferici." *Bollettino dell'Unione Matematica Italiana* 7, 3 (1952).

[64] L. Peng and Q. Gong. "An accurate Fortran code for computing hydrogenic continuum wave functions at a wide range of parameters". *Computer Physics Communications* 181, 12 (2010).

[65] A. M. Perelomov, V. S. Popov, and M. V. Terentev. "Ionization of atoms in an alternating electric field". *Sov. Phys. JETP* 23, 5 (1966).

[66] A. M. Perelomov, V. S. Popov, and M. V. Terentev. "Ionization of atoms in an alternating electric field: II". *Sov. Phys. JETP* 24.1 (1967).

[67]   G. Petite, P. Agostini, and H. G. Muller. "Intensity dependence of non-perturbative above-threshold ionisation spectra: experimental study". *Journal of Physics B: Atomic, Molecular and Optical Physics* 21, 4097 (1988).

[68]   B. Piraux. Private communication: Offered help in the derivation of the coefficients of the continuum Coulomb functions in the Sturmian basis. (2018).

[69]   V. S. Popov. "Tunnel and multiphoton ionization of atoms and ions in a strong laser field (Keldysh theory)". *Physics-Uspekhi* 47, 9 (2004).

[70]   W. Press et al. *Numerical Recipes in Fortran 77: The Art of Scientific Computing.* (1992).

[71]   H. R. Reiss. "The tunnelling model of laser-induced ionization and its failure at low frequencies". *Journal of Physics B: Atomic, Molecular and Optical Physics* 47, 204006 (2014).

[72]   A. Rudenko et al. "Coulomb singularity in the transverse momentum distribution for strong-field single ionization". *Journal of Physics B: Atomic, Molecular and Optical Physics* 38, L191 (2005).

[73]   Y. Saad. *Iterative methods for sparse linear systems.* Siam, (2003).

[74]   J. Sapirstein and W. R. Johnson. "The use of basis splines in theoretical atomic physics". *Journal of Physics B: Atomic, Molecular and Optical Physics* 29, 5213 (1996).

[75]   K. J. Schafer. *Strong field laser physics.* Vol. 134. Springer, (2008).

[76]   K. J. Schafer et al. "Above threshold ionization beyond the high harmonic cutoff". *Physical Review Letters* 70, 1599 (1993).

[77]   A. Scrinzi, M. Geissler, and T. Brabec. "Ionization above the Coulomb barrier". *Physical Review Letters* 83, 706 (1999).

[78]   B. W. Shore. "Use of the Rayleigh-Ritz-Galerkin method with cubic splines for constructing single-particle bound-state radial wavefunctions: The hydrogen atom and its spectrum". *Journal of Physics B: Atomic and Molecular Physics* 6, 1923 (1973).

[79]   A. S. Simonsen et al. "Ionization dynamics beyond the dipole approximation induced by the pulse envelope". *Physical Review A* 93, 053411 (2016).

[80]   C. T. L. Smeenk et al. "Partitioning of the linear photon momentum in multiphoton ionization". *Physical Review Letters* 106, 193002 (2011).

[81]   R. Szmytkowski. "Alternative approach to the solution of the momentum-space Schrödinger equation for bound states of the N-dimensional Coulomb problem". *Annalen der Physik* 524, 6-7 (2012).

[82]   H. A. Van der Vorst. "Bi-CGSTAB: A fast and smoothly converging variant of Bi-CG for the solution of nonsymmetric linear systems". *SIAM Journal on scientific and Statistical Computing* 13, 2 (1992).

[83]   G. S. Voronov and N. B. Delone. "Many photon ionization of the xenon atom by ruby laser radiation". *Sov. Phys. JETP* 23 (1966).

[84]   A Weingartshofer et al. *Physical Review Letters* 39, 269 (1977).

Appendix A: Momentum Space Representation of the Coulomb Potential

Momentum Space Schrödinger Equation

The time independent Schrödinger equation in position space is well known as

$$-\frac{1}{2}\nabla^2\Psi(\mathbf{r}) + V(\mathbf{r})\Psi(\mathbf{r}) = E\Psi(\mathbf{r}) \qquad (A.1)$$

where $V(\mathbf{r})$ is the attractive Coulomb potential. The momentum space representation of equation (A.1) is

$$\left(\frac{p^2}{2} - E\right)\Phi(\mathbf{p}) + \frac{1}{(2\pi)^{\frac{3}{2}}}\int d^3\mathbf{p}' U(\mathbf{p} - \mathbf{p}')\Phi(\mathbf{p}') = 0 \qquad (A.2)$$

where $\Phi(\mathbf{p})$ and $U(\mathbf{p})$ are the Fourier transforms of the position space representations of the wave function and Coulomb potential, respectively. $U(\mathbf{p})$ can be shown to be [55]

$$U(\mathbf{p}) = -\frac{2^{\frac{1}{2}}Z}{\sqrt{\pi}}\frac{1}{p^2}. \qquad (A.3)$$

Substituting equation (A.3) into equation (A.2) produces the following equation for the time independent momentum space Schrödinger equation (TIMSE)

$$\left(\frac{p^2}{2} - E\right)\Phi(\mathbf{p}) = \frac{Z}{(2\pi)^3} \int d^3\mathbf{p}'\Phi(\mathbf{p}')\mathcal{V}(\mathbf{p}' - \mathbf{p}) \qquad (A.4)$$

where

$$\mathcal{V}(\mathbf{p}' - \mathbf{p}) = \frac{4\pi}{|\mathbf{p}' - \mathbf{p}|^2} \qquad (A.5)$$

is the kernel of the Coulomb potential in momentum space. Details of the solution to equation (A.2) are given in [81] and [14].

This is the crux of the problem when solving the TIMSE or the time dependent momentum space Schrödinger equation (TDMSE) and must be approximated. One way to approximate equation (A.5) is to represent it in terms of symmetric separable potentials supporting N bound states of atomic hydrogen

$$\mathcal{V}(\mathbf{p}' - \mathbf{p}) \approx \mathcal{V}(\mathbf{p}', \mathbf{p}) = \sum_{n=1}^{N} v_n^*(\mathbf{p}')v_n(\mathbf{p}). \qquad (A.6)$$

Two methods to generate these separable potentials are presented in [36]. One method is the solution of the system

$$\mathbf{\Phi} + \mathbf{A}\mathbf{V} = 0 \qquad (A.7)$$

for $\mathbf{V}$ which introduces some arbitrariness in the definition of v_n. We devised a second method which sees the kernel represented in terms of Gegenbauer polynomials, the Fourier transforms of Sturmian functions, and spherical harmonics. We shall cover the mathematics behind the second method in this appendix.

We start by writing

$$\frac{1}{|\mathbf{p}' - \mathbf{p}|^2} = \frac{1}{p^2}\frac{1}{1 - 2\rho x + \rho^2} \tag{A.8}$$

where $x = \cos\theta$ (the angle between $\mathbf{p}'$ and $\mathbf{p}$) and $\rho = |\mathbf{p}'/\mathbf{p}|$. From equation 2 in [20] we can rewrite equation (A.8) as

$$\frac{1}{p^2}\frac{1}{1 - 2\rho x + \rho^2} = \frac{\Gamma(\mu)e^{i\pi(\mu - \frac{1}{2})}}{p^2\sqrt{\pi}(1 - \rho^2)^{(\frac{1}{2}-\mu)}} \sum_{l=0}^{\infty}(l+\mu)\mathcal{Q}_{l+\mu-\frac{1}{2}}^{\frac{1}{2}-\mu}\left(\frac{1+\rho^2}{2\rho}\right)C_l^{\mu}(x) \tag{A.9}$$

where $\mathcal{Q}_l^{\mu}$ is a Legendre function of the second kind and C_l^{μ} is a Gegenbauer polynomial. By setting $\mu = 1/2$ and noting $C_l^{\frac{1}{2}}(x) = P_l(x)$, this simplifies to

$$\frac{1}{p^2}\frac{1}{1 - 2\rho x + \rho^2} = \frac{1}{p^2\rho}\sum_{l=0}^{\infty}\mathcal{Q}_l^0\left(\frac{p^2 + p'^2}{2pp'}\right)P_l(\cos\theta). \tag{A.10}$$

Equation 11 in [63] allows us to recast $\mathcal{Q}_l^0$ in terms of Gegenbauer polynomials and along with the fact that

$$P_l(\cos\theta) = \frac{4\pi}{2l+1}\sum_{m=-l}^{l}Y_{l,m}^*(\hat{\mathbf{p}})Y_{l,m}(\hat{\mathbf{p}}') \tag{A.11}$$

then $\mathcal{V}(\mathbf{p}', \mathbf{p})$ becomes

$$\mathcal{V}(\mathbf{p}', \mathbf{p}) = \sum_{l=0}^{\infty}\sum_{n=0}^{\infty}N_{n,l}v_{n,l}^*(p)v_{n,l}(p')\sum_{m=-l}^{l}Y_{l,m}^*(\hat{\mathbf{p}})Y_{l,m}(\hat{\mathbf{p}}') \tag{A.12}$$

to match equation 23 in [36] where

$$v_{n,l}(p) = \frac{1}{p}\left(\frac{2qp}{q^2 + p^2}\right)^{l+1}C_n^{l+1}\left(\frac{q^2 - p^2}{q^2 + p^2}\right) \tag{A.13}$$

and the coefficient $N_{n,l}$ is given by

$$N_{n,l} = \pi[\Gamma(l+1)]^2 \frac{2^{2l+2}(2l+1)}{\Gamma(n+2l+2)}(n!). \tag{A.14}$$

In fact, $v_{n,l}(p)$ is nothing other than the Coulomb Sturmian function in momentum space. By performing a Fourier transform on the function $v_{n,l}(p)$, we obtain the Coulomb Sturmian function in position space up to a normalisation factor. It is clear by this stage, that the free parameter q determines the range of the potential in momentum space.

This decomposition of the Coulomb kernel, equation (A.12), serves as a starting point for solving the TDMSE. Of course in practice, equation (A.12) would be truncated to include as many states that one would desire or that could be handled.

Appendix B: Derivation of the Coefficients of the Continuum Coulomb Functions in the Sturmian Basis

The following was produced in correspondence with Professor Bernard Piraux of Université Catholique de Louvain [68].

The Derivation of the Coefficients of the Continuum Coulomb Functions in the Sturmian Basis

The ingoing Coulomb continuum function is written as

$$\psi_{\mathbf{p}}^{-}(\mathbf{r}) = \sum_{l,m} \frac{4\pi}{2l+1} R_l^{-}(pr) Y_{l,m}(\hat{\mathbf{p}}) Y_{l,m}^{*}(\hat{\mathbf{r}}) \tag{B.1}$$

with

$$R_l^-(pr) = (-1)^l(2\pi)^{\frac{3}{2}}e^{\frac{Z\pi}{2p}}\frac{\Gamma(l+1-iZ/p)}{(2l)!}(2ipr)^le^{ipr}$$
$$\times\,_1F_1(l+1-iZ/p;2l+2;-2ipr)$$

(B.2)

where $_1F_1(a;b;z)$ are the confluent hypergeometric functions of the first kind
and that

$$\int \psi_{\mathbf{p}'}^{-,*}(\mathbf{r})\psi_{\mathbf{p}}^{-}(\mathbf{r})d\mathbf{r} = \delta(\mathbf{p}'-\mathbf{p}).$$

(B.3)

We may write the Sturmian functions in terms of the confluent hypergeo-
metric functions of the first kind (in Chapter 3 we define them in terms of the
associated Laguerre polynomials)

$$S_{n,l}^\kappa(r) = \frac{1}{(2l+1)!}\sqrt{\frac{4\kappa^3}{n}\frac{(n+l)!}{(n-l-1)!}}e^{-\kappa r}(2\kappa)^lr^{l+1}{}_1F_1(l+1-n;2l+2;2\kappa r).$$

(B.4)

We define the coefficients $a_{\nu,l}(p)$ as follows

$$\psi_{\mathbf{p}}^{-,*}(\mathbf{r}) = \sum_{l,m}\sum_{\nu}a_{\nu,l}(p)\frac{S_{\nu,l}^\kappa(r)}{r}Y_{l,m}(\hat{\mathbf{p}})Y_{l,m}^*(\hat{\mathbf{r}}).$$

(B.5)

Using equation (B.1), we can calculate the coefficients $a_{\nu,l}(p)$ by performing

$$
\begin{aligned}
a_{\nu,l}(p) &= \frac{4\pi}{2l+1}\frac{\nu}{\kappa}\int_0^\infty dr S_{\nu,l}^{\kappa}(r)R_l^{-,*}(pr) \\
&= \frac{4\pi}{2l+1}\frac{\nu}{\kappa}\frac{1}{(2l+1)!}\sqrt{\frac{4\kappa^3}{\nu}\frac{(\nu+l)!}{(\nu-l-1)!}}(2\kappa)^l(-2ip)^l(2\pi)^{\frac{-3}{2}}e^{\frac{Z\pi}{2p}}\frac{1}{(2l)!} \\
&\quad \times \Gamma(l+1-iZ/p)\int_0^\infty dr\Big(e^{-(\kappa-ip)r}r^{2l+1}{}_1F_1(l+1-\nu;2l+2;2\kappa r) \\
&\quad \times {}_1F_1(l+1-iZ/p;2l+2;-2ipr)\Big) \\
&= \sqrt{\frac{2\nu\kappa}{\pi}}\frac{2}{[(2l+1)!]^2}\sqrt{\frac{(\nu+1)!}{(\nu-l-1)!}}(-4i\kappa p)^l e^{\frac{Z\pi}{2p}} \\
&\quad \times \Gamma(l+1-iZ/p)\int_0^\infty dr\Big((e^{(\kappa-ip)r}r^{2l+1}{}_1F_1(l+1-\nu;2l+2;2\kappa r) \\
&\quad \times {}_1F_1(l+l-iZ/k;2l+2;-2ipr)\Big).
\end{aligned}
$$

$$(B.6)$$

Letting $x = 2\kappa r$ and using the following identity in [39] (G.R. 7.622.1) we have

$$
\begin{aligned}
I &= \int_0^\infty dr\Big(e^{-(\kappa-ip)r}r^{2l+1}{}_1F_1(l+1-\nu;2l+2;2\kappa r)\Big) \\
&\quad \times {}_1F_1(l+1-iZ/p;2l+2;-2ipr) \\
&= \left(\frac{1}{2\kappa}\right)^{2l+2}\int_0^\infty dx\Big(e^{-\frac{1}{2}(1-ip/\kappa)x}x^{2l+1}{}_1F_1(l+1-\nu;2l+2;x) \\
&\quad \times {}_1F_1(l+1-iZ/p;2l+2;ipx/\kappa)\Big) \\
&= \left(\frac{1}{2\kappa}\right)^{2l+2}(2l+1)!\left[-\left(\frac{1}{2}+\frac{ip}{2\kappa}\right)\right]^{\nu-l-1}\left[\frac{1}{2}+\frac{ip}{2\kappa}\right]^{\frac{iZ}{p}-l-1}\left[\frac{1}{2}-\frac{ip}{2\kappa}\right]^{-\nu-\frac{iZ}{p}} \\
&\quad \times {}_2F_1\left(l+1-\nu,l+1-\frac{iZ}{p};2l+2l;\frac{-ip/\kappa}{(\frac{1}{2}+\frac{ip}{2\kappa})^2}\right).
\end{aligned}
$$

$$(B.7)$$

THE DERIVATION OF THE COEFFICIENTS OF THE CONTINUUM COULOMB FUNCTIONS IN THE STURMIAN BASIS

If we let $\lambda = -ip/\kappa$, then we can recast equation (B.7) as

$$
\begin{aligned}
I &= \left(\frac{1}{2\kappa}\right)^{2l+2} 4^{l+1}(-1)^{\nu-l-1}(1-\lambda)^{-(2l+2)}\left[\frac{1-\lambda}{1+\lambda}\right]^{\nu+\frac{iZ}{p}} \\
&\quad \times (2l+1)!\,_2F_1\left(l+1-\nu, l+1-\frac{iZ}{p}; 2l+2; \frac{-4\lambda}{(1-\lambda)^2}\right).
\end{aligned}
\tag{B.8}
$$

We also have

$$
\begin{aligned}
\left[\frac{1+\lambda}{1-\lambda}\right]^{\frac{iZ}{p}} &= \left[\frac{1+ip/\kappa}{1-ip/\kappa}\right]^{\frac{iZ}{p}} \\
&= \left[\frac{(1+p^2/\kappa^2)e^{i\arctan(p/\kappa)}}{(1+p^2/\kappa^2)e^{-i\arctan(p/\kappa)}}\right]^{\frac{iZ}{p}} \\
&= e^{-\frac{Z}{p}\arctan\left(\frac{p}{\kappa}\right)}.
\end{aligned}
\tag{B.9}
$$

Hence, we finally obtain

$$
\begin{aligned}
a_{\nu,l}(p) &= \left(\frac{2}{\kappa}\right)^{2l+\frac{3}{2}}\sqrt{\frac{\nu}{\pi}}\frac{1}{(2l+1)!}\sqrt{\frac{(\nu+l)!}{(\nu-l-1)!}}(-1)^{\nu-1}(i\kappa p)^l \\
&\quad \times e^{\frac{Z\pi}{2p}}\Gamma(l+1-iZ/p)(1-\lambda)^{-(2l+2)}\left[\frac{1-\lambda}{1+\lambda}\right]^{\nu}e^{\frac{-2Z}{p}\arctan\left(\frac{p}{\kappa}\right)} \\
&\quad \times \,_2F_1\left(l+l-\nu, l+1-\frac{iZ}{p};; 2l+2; \frac{-4\lambda}{(1-\lambda)^2}\right).
\end{aligned}
\tag{B.10}
$$

We now look to expand the radial Coulomb function in terms of Sturmian functions:

$$
R_l^{-,*}(pr) = \sum_{\nu} \tilde{a}_{\nu,l}(p)\frac{S_{\nu,l}^{\kappa}(r)}{r}
\tag{B.11}
$$

where

$$
a_{\nu,l}(p) = \frac{4\pi}{2l+1}\tilde{a}_{\nu,l}(p).
\tag{B.12}
$$

THE DERIVATION OF THE COEFFICIENTS OF THE CONTINUUM COULOMB FUNCTIONS IN THE STURMIAN BASIS

It is useful for computational purposes to express $\tilde{a}_{\nu,l}$ in terms of the Pollaczek polynomials [7]. In expressing these coefficients in terms of Pollaczek polynomials, we are able to use a recurrence relation in the Pollaczek polynomials to recursively calculate successive coefficients in equation (B.11). The definition of the Pollaczek polynomial in terms of $_2F_1$ is as follows:

$$P_n^\lambda(x; a, b) = \frac{1}{n!}(2\lambda)_n e^{in\theta} {}_2F_1(-n, \lambda + it; 2\lambda; 1 - e^{-2i\theta}) \tag{B.13}$$

where $(c)_n$ is the Pochhammer function defined as follows:

$$(c)_n = c(c+1)(c+2)...(c+n-1) = \frac{(c+n-1)!}{(c-1)!}. \tag{B.14}$$

We also define

$$t = (ax + b)(1 - x^2)^{\frac{-1}{2}} \tag{B.15}$$

and

$$x = \cos(\theta). \tag{B.16}$$

Let us write

$$\theta = \arctan\left(\frac{p}{\kappa}\right). \tag{B.17}$$

Therefore, we can write

$$e^{2i\theta} = \frac{(\kappa + ip)^2}{\kappa^2 + p^2} \tag{B.18}$$

and we also have

$$\frac{-4\lambda}{(1-\lambda)^2} = \frac{4ip\kappa}{(\kappa + ip)^2} = \frac{4ip\kappa(\kappa - ip)^2}{(\kappa^2 + p^2)^2}. \tag{B.19}$$

This is useful because from equation (B.18)

$$
\begin{aligned}
(1 - e^{-4i\theta}) &= (1 - e^{-2i\theta})(1 + e^{-2i\theta}) \\
&= [(1 - \cos(2\theta)) + i\sin(2\theta)][(1 + \cos(2\theta)) - i\sin(2\theta)] \\
&= \left[\frac{2p^2}{\kappa^2 + p^2} + \frac{2ip\kappa}{\kappa^2 + p^2}\right]\left[\frac{2\kappa^2}{\kappa^2 + p^2} - \frac{2ip\kappa}{\kappa^2 + p^2}\right] \\
&= \frac{4ip\kappa(\kappa - ip)^2}{(\kappa^2 + p^2)^2}.
\end{aligned}
\tag{B.20}
$$

which is equivalent to equation (B.19).

We can find the value of t by looking at equations (B.10) and (B.13):

$$
\begin{aligned}
t = -\frac{Z}{p} &= \frac{a + \cos(2\theta) + b}{\sqrt{1 - \cos^2(2\theta)}} \\
&= \frac{a\cos(2\theta) + b}{\sin(2\theta)} \\
&= \frac{a(\kappa^2 - p^2) + b(\kappa^2 + p^2)}{2\kappa p} \\
&= \frac{\kappa^2(a + b) + p^2(a - b)}{2\kappa p}.
\end{aligned}
\tag{B.21}
$$

Comparing coefficients in κ and p, we can deduce that

$$
a - b = 0
\tag{B.22}
$$

and

$$
a = b = \frac{-Z}{p}.
\tag{B.23}
$$

In addition, we recast n in terms of ν

$$
n = \nu - (l + 1)
\tag{B.24}
$$

$$
(2\lambda)_n = \frac{(l + \nu)!}{(2l + 1)!}
\tag{B.25}
$$

and

$$e^{2in\theta} = e^{2i(\nu-l-1)\theta}. \tag{B.26}$$

From these manipulations, we are able to represent $_2F_1$ with in terms of Pollaczek polynomials:

$$
\begin{aligned}
_2F_1&(l+1-\nu, l+1-iZ/p; 2l+2; 1-e^{-4i\theta}) \\
&= \frac{(2l+1)!(\nu-l-1)!}{(l+\nu)!} e^{-2i(\nu-l-1)\theta} P_{\nu-l-1}^{l+1}\left(\cos(2\theta); \frac{-Z}{p}, \frac{-Z}{p}\right).
\end{aligned}
\tag{B.27}
$$

Finally, using

$$(1-\lambda)^{-(2l+2)}\left(\frac{1-\lambda}{1+\lambda}\right)^{\nu+\frac{iZ}{p}} = \frac{e^{-i\theta(2l+2)}}{(\kappa^2+p^2)^{l+1}} e^{2i\nu\theta} e^{-2\frac{Z}{p}\theta} \kappa^{2l+2} \tag{B.28}$$

with equation (B.12), we finally obtain

$$
\begin{aligned}
a_{\nu,l}(p) = {}& \frac{(-1)^{\nu-1}}{2l+1}\sqrt{\frac{2\nu\kappa}{\pi}}(4l\kappa)(4i\kappa p)^l \sqrt{\frac{(\nu-l-1)!}{(\nu+l)!}} \\
& \times \frac{\Gamma(l+1-iZ/p)}{(\kappa^2+p^2)^{l+1}} e^{\frac{Z}{p}\left(\frac{\pi}{2}-2\theta\right)} P_{\nu-l-1}^{l+1}\left(\cos(2\theta); \frac{-Z}{\kappa}; \frac{-Z}{\kappa}\right).
\end{aligned}
\tag{B.29}
$$